A Thesis Submitted for the Degree of PhD at the University of Warwick

Permanent WRAP URL:

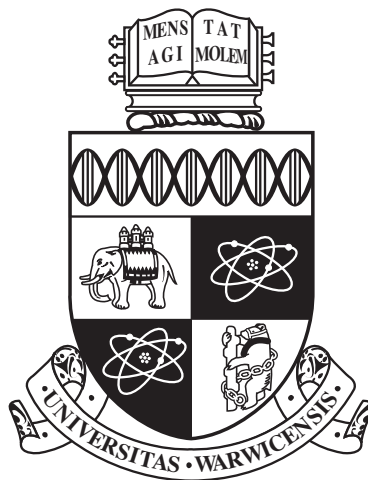http://wrap.warwick.ac.uk/180349

warwick.ac.uk/lib-publications

Spectroscopy of Single-walled Carbon Nanotubes with Atomic Nanowire Filling

by

Ziyi Hu

Thesis

Submitted to the University of Warwick

for the degree of

Doctor of Philosophy in Physics

Department of Physics

December 2022

THE UNIVERSITY OF

WARWICK

Contents

List of Tables

Acknowledgments

I first want to thank my two PhD supervisors, Dr. James Lloyd-Hughes and Dr. Jeremy Sloan. It was a great pleasure to work with them in the last four years or so. I also want to thank the colleagues from my research group and friends, Edward, Maurizio, Kiran, Maria, Daniel, Connor, Jake, Sophie, Junn, Justas, Helen, Huiliang, Amelia,... Because of them, I discovered far more interesting and exciting things beyond just research. I would like to give a big thank to my parents and my family. It was them who encouraged me when I struggled with my research.

Besides, I would also like to thank Kadie, Fu and Liwei for being good colleagues and advisors.

I appreciate the sponsorship of China Scholarship Council that supports my PhD study. Also, I would like to thank the following Research Technology Platforms (RTPs) at University of Warwick that provide opportunities of material characterizations and analyses: Warwick Centre for Ultrafast Spectroscopy (WCUS), Electron Microscopy RTP, Spectroscopy RTP and X-ray Photoelectron Spectroscopy (XPS) RTP. I especially want to thank Dr. Michael Staniforth, Dr. Ben Breeze, Dr. Jack Woolley, Dr. Steve York, Dr. Yisong Han, Dr. Steve Hindmarsh and Dr. Reza Kashtiban for offering training on the facilities. Additionally, I thank Dr. Eric Faulques for helping with the Raman characterizations.

Declarations

I declare this thesis is about my own work except where indicated. It has not been submitted for a degree at another university. Results of theoretical calculations on the nanostructure formation energies shown in **Appendix B** were conducted by A. Vasylenko and his colleagues.

The results presented in this thesis are taken from or adapted from the following articles:

1. Ziyi Hu*, Ben Breeze, Reza J. Kashtiban, Jeremy Sloan*, and James Lloyd-Hughes* Zigzag HgTe Nanowires Modify the Electron–Phonon Interaction in Chirality-Refined Single-Walled Carbon Nanotubes. *ACS Nano*, 2022, 16, 4, 6789-6800

2. Ziyi Hu*, Ben Breeze, Marc Walker, Eric Faulques, Jeremy Sloan*, James Lloyd-Hughes* Spectroscopic Insights into the Influence of Filling Carbon Nanotubes with Atomic Nanowires for Photophysical and Photochemical Applications. *ACS Applied Nano Materials* 2023, 6, 4, 2883–2893.

3. *Abstract* Ziyi Hu, Jeremy Sloan, and James Lloyd-Hughes Modifying electron-phonon interaction in chirality-refined single-walled carbon nanotubes by zigzag HgTe nanowire filling. *ACS Fall Meeting* 2022

Other featured articles published during my PhD which are not present here:

1. Ziyi Hu, Ryan O'Neill, Rostyslav Lesyuk, Christian Klinke* Colloidal Two-dimensional Metal Chalcogenides: Realization and Application of the Structural Anisotropy. *Accounts of Chemical Research*, 2021, 54, 20, 3792–3803

The results presented in this thesis have been partly reported at the following scientific conferences and workshops:

2. Modifying electron-phonon interaction in chirality-refined single-walled carbon nanotubes by zig-zag HgTe nanowire filling, ACS Fall Meeting 2022, Chicago (Virtual), USA, 2022, Oral presentation.

3. Synthesis and Spectroscopy of Chirality-Refined HgTe-Filled Single Walled Carbon Nanotubes, 7th Nano Today Conference, Guangzhou (Virtual), China, 2021, Poster presentation.

Abbreviations

AC aberration-corrected

ADF annular dark field

AFM atomic force microscopy

ATP aqueous two-phase

BF bright field

BWF Breit-Wigner-Fano

BZ Brillouin zone

CB conduction band

CD circular dichroism

CVD chemical vapor deposition

CCVD catalytic chemical vapor deposition

CL condenser lens

CLA condenser lens aperture

DI deionized

DX dextran

DFT density functional theory

DOC sodium deoxycholate

DOS density of states

DGU density gradient ultracentrifugation

DR double resonance

ED electron diffraction

EDX energy dispersive X-ray analysis

EET exciton energy transfer

FIR far-infrared

FTIR Fourier Transform infrared

F8BT poly(9,9-dioctylfluorene-*alt*-benzothiadiazole

HgTe mercury telluride

HRTEM high-resolution transmission electron microscopy

IR infrared

JDOS joint density of states

LA longitudinal acoustic

LCVD laser-assisted chemical vapor deposition

LO longitudinal optic

MIR mid-infrared

MWCNTs multi-walled carbon nanotubes

NEXAS near-edge X-ray absorption spectroscopy

NIR near-infrared

NW nanowire

OL objective lens

OPTP optical pump-terahertz probe

PA photo-absorption

PB photo-bleaching

PFD poly(9,9-di-n-dodecylfluorene)

PFO poly(9,9-dioctylfluorene

PID propotional integral-differential

PL photoluminescence

PLE photoluminescence-excitation

PLQY photoluminescence quantum yield

PMT photomultiplier

PEG polyethylene-glycol

QNM quantum nanomechanical

QY quantum yield

RBM radial breathing mode

RRS resonant Raman scattering

SA selected area aperture

SC sodium cholate

SDS sodium dodecyl sulfate

SDBS sodium dodecyl benzene sulfonate

SEM scanning electron microscopy

SR single resonance

STEM scanning transmission electron microscope

SWCNTs single-walled carbon nanotubes

TA transient absorption

TCSPC time-correlated single-photon counting

THz-TDS time-domain terahertz

TO transverse optic

TOPAS optical parametric amplifiers

UV ultraviolet

VB valence band

vis visible

XPS X-ray photoelectron spectroscopy

1D one-dimensional

2D two-dimensional

List of Symbols

d_t nanotube diameter

$\mathbf{C}$ chiral vector

(n, m) chiral indices

θ chiral angle

N number of hexagons of the graphite honeycomb lattice in the nanotube unit cell

d_R great common divisor of $(2n + m)$ and $(2m + n)$

$\mathbf{k}$ wave-vector

$V_{pp\pi}$ nearest neighbour transfer integral

$(\hat{\mathbf{k}}_x, \hat{\mathbf{k}}_y)$ coordinate basis in reciprocal space

E_{cmini} conduction minimum for the given band

$\parallel T \parallel$ amplitude of translational vector

γ_0 nearest-neighbour hopping parameter

ν_{11} 1st-order transition energy in units of cm^{-1}

ν_{22} 2nd-order transition energy in units of cm^{-1}

S_{ii} transition energy of semiconducting nanotubes in units of eV

M_{ii} transition energy of metallic nanotubes in units of eV

sp^2 hybridization of one s orbital and two p orbitals

sp^3 hybridization of one s orbital and three p orbitals

λ wavelength of light

μ refractive index of medium

β collection semi-angle

δ Rayleigh criterion

τ time constant of a lifetime component

ω frequency

q term describing the coupling strength between phonon and electronic continuum

Γ linewidth of Raman mode

E_b exciton binding energy

E_g band gap energy

A Auger constant

γ Auger rate coefficient

k rate coefficient of an exponential term

$A_{1g}(A_1), E_{1g}(E_1), E_{2g}(E_2)$ Raman modes with different symmetry

ν_q plasmon mode velocity

I_{int} intensity of inter-band emission

I_{ph} intensity of phonon scattering

$\sigma(\omega)$ frequency-domain conductivity

ϵ_0 dielectric permitivity of free space

c light speed in vacuum

$\tilde{n}_S$ complex frequency-dependent refractive index

$T(\omega)$ frequency-domain transmission

Z_0 impedance of free space

m^* effective mass of carriers

γ_D, γ_p momentum scattering rates of the Drude and surface plasmon model

ω_p plasmon resonant frequency

Abstract

The tight nanopore of single-walled carbon nanotube (SWCNT) offer atomically smooth templates for the growth of ultrathin one-dimensional (1D) nanocrystals. Although filling of various types of compounds or molecules inside carbon nanotubes has been reported over the last 20 years or so, a comprehensive understand on the physics behind such a coupling between the 1D nanomaterials is far from satisfactory.

In this thesis, the optical properties of chirality-refined SWCNTs filled by ultrathin nanowire-shaped crystals were studied by means of steady-state and time-resolved spectroscopy. By encapsulating mercury telluride (HgTe), a narrow band gap semiconductor in the bulk form, the excitonic properties, phonon features and transient dynamics of nanotubes were found to be noticeably changed. Additionally, it was revealed that the performance of carbon nanotubes was determined by both the geometry of nanowire and SWCNT parameters such as chirality or tube diameter.

Later in this thesis, the influence of environment on the optical properties of SWCNTs was investigated. By means of photoluminescence characterization, it was demonstrated that a change of the suspending medium from water to gelatin matrix can lead to a modified many-body interactions in nanotubes. Based on the subsequent temperature-dependent photoluminescence and Raman measurements, it was found that the encapsulated nanowires can alter both the intratube stiffness and the intertube interactions of carbon nanotubes.

Chapter 1

Introduction and Structure of Thesis

Carbon nanotubes are one-dimensional nanomaterials with high aspect ratios and rigid chiral structures. They have tremendous and fascinating optical properties, such as large exciton binding energies [1] and significant optical anisotropy [2; 3]. Due to these benefits, carbon nanotubes have shown potential in various fields such as light harvesting, catalytic reactions and biomedical labelling.

The optical properties of carbon nanotubes can be actively controlled by its structure parameters such as diameter and chirality. Carbon nanotube suppliers such as CoMoCAT® and NanoIntegris® are now capable to produce high-quality single-walled carbon nanotubes in a sufficiently wide diameter range (0.7-2 nm), whose optical response lies in a spectral window spanning from ultraviolet to infrared [4; 5; 6]. In recent decades, the development of liquid phase-based sorting protocols realized the refinement of nanotubes with particular chiralities and diameters. The successful separation of different nanotube species allows the origins of various optical phenomena to be clarified, such as inter-nanotube exciton energy transfer [7] or chirality-dependent shift of Raman modes [8].

Templating or encapsulating materials inside carbon nanotubes has been discovered as far back as 1997, when Smith et al. proved that C_{60} can exist inside the nanotubes [9]. In following years, the encapsulation of other molecules and nanowires was demonstrated by several research groups [10; 11; 12; 13]. It was revealed by optical spectroscopic measurements that such guest materials can alter the excitonic transition performance and charge carrier transport ability of carbon nanotubes [13; 14; 15]. Although the promise of filled carbon nanotubes had been demonstrated, further studies on these materials are hindered by a lack of knowledge

on the actual nanotube composition and parameters, which is required for understanding the mechanism of one-dimensional material filling affecting the properties of individual nanotube species.

The main focus of this thesis is to explore the properties of atomic nanowire-filled carbon nanotubes and the impact of infiltration. The structure of thesis is started with an introduction of the carbon nanotube properties and previous research on nanotube filling or functionalization, followed by the chapters presenting results of structure and spectroscopic characterizations on the materials.

Chapter 2 is an introduction of the electronic properties of carbon nanotubes, which include chiralities, electronic band structures and the optical transition performance. The progress in chemically separating and purifying carbon nanotubes, synthesis of filled nanotubes and control of electronic properties via doping are then discussed.

Chapter 3 introduces the characterizing techniques applied in this thesis. Material structure analysis is conducted by means of electron microscopic imaging. The physical and optical properties of nanotube samples are studies based on various types of spectroscopic characterizations.

Chapter 4 provides details about the protocols of material fabrication and separation. The structures and steady-state optical properties of nanowire-filled SWCNTs are analyzed.

Chapter 5 and **6** investigate the effect of nanowire infiltration on the optical performance of carbon nanotubes via broadband absorption spectroscopy, photoluminescence, Raman scattering and time-resolved spectroscopy.

Chapter 7 studies the environment effect on carbon nanotubes. Temperature-dependent $in-situ$ measurements are conducted to further investigate the interaction between nanotubes and encapsulated nanowires.

Chapter 8 provides a summary of the discoveries based on the experimental characterizations and analyses above. The outcomes and implications of the studies in this thesis is also discussed.

Chapter 2

Fundamentals of Carbon Nanotubes and Nanotube-based Materials

In this chapter we focus on the fundamentals of SWCNTs such as the assignment of chiral structures, estimations of excitonic transition energies based on theories, and chemical interactions with other materials. This is important for understanding the optical and physiochemical properties of SWCNTs as we will discuss in following chapters.

2.1   Structure of SWCNTs

The structure of SWCNTs can be physically regarded as rolling a two-dimensional (2D) graphene sheet into a cylinder. The rolling direction is defined by the chiral vector $\mathbf{C} = n\mathbf{a}_1 + m\mathbf{a}_2$, where $\mathbf{a}_1$ and $\mathbf{a}_2$ are the basis vectors of graphene. A schematic to describe the formation of a SWCNT is shown in **Figure 2.1**. In this way, the structure of a SWCNT can be represented by this pair of indices (n, m), with its diameter d_t and chiral angle θ expressed as:

$$d_t = \frac{|a_1|}{\pi}\sqrt{n^2 + nm + m^2} = 0.783\sqrt{n^2 + m^2 + nm} \tag{2.1}$$

$$\theta = \cos^{-1}\left(\frac{2n + m}{2\sqrt{n^2 + m^2 + nm}}\right) \tag{2.2}$$
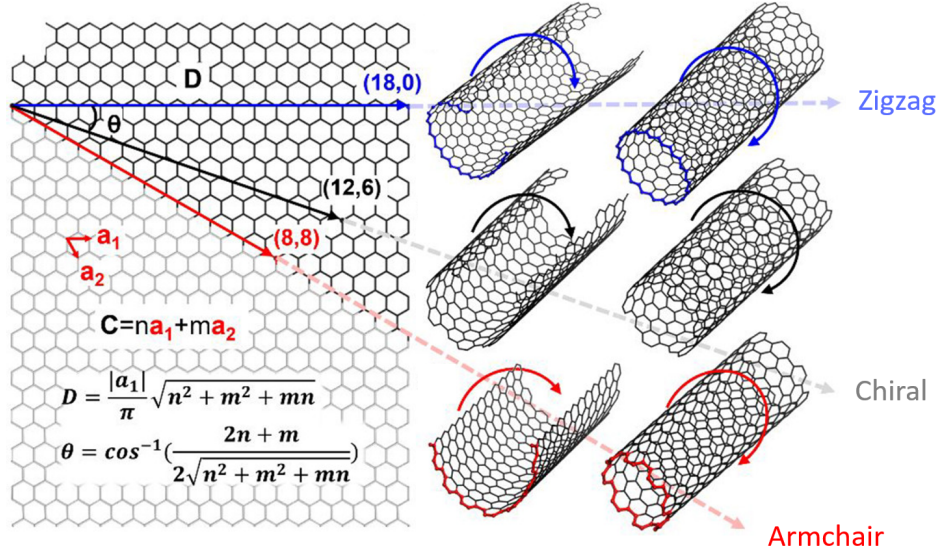
Figure 2.1: Schematic to show the formation of SWCNTs.

Consequently, the SWCNTs can be divided into zigzag ($\theta=0°$), armchair ($\theta=30°$) and chiral ($0°<\theta<30°$) nanotubes. Further to this, by taking the $mod(2n+m,3)$ value (remainder of $2n+m$ divided by 3) of a SWCNT one can get 0, 1 and 2, which correspond to a metallic, a type-1 semiconducting and a type-2 semiconducting nanotube, respectively. It is normally considered that only armchair SWCNTs ($n=m$) are strict metallic nanotubes, whilst other types of metallic nanotubes (especially near-zigzag SWCNTs with a θ of $\sim0°$) have split electronic states at the K-point due to the trigonal warping effect [16].

Over the years, several methods has been developed for the industry-scale preparation of high-quality carbon nanotubes [17]. They can generally be classified into the arc-discharge [18], laser vaporization (ablation) [19] and chemical vapor deposition (CVD) methods. As the most important commercial method, CVD technique is now widely used to grow SWCNTs with a wide range of diameters (from <1 to up to 5 nm). Examples of such methods include the CoMoCAT process, high-pressure carbon monoxide (HiPco) process, catalytic chemical vapor deposition (CCVD) [20], laser-assisted chemical vapor deposition (LCVD) [21]. The as-received carbon nanotube product from these methods are usually end-capped. Catalytic metal particles can also coexist with these SWCNTs.

While large-diameter SWCNTs and multi-walled carbon nanotubes (MWCNTs) are sometimes more suitable for electron microscopic imaging or X-ray diffraction analysis due to the effect of their sizes, their electronic and optical properties

can significantly differ from those of small-diameter ones, especially SWCNTs have a width of <1 nm, such as (6,5) and (7,5). A comprehensive understanding of carbon nanotubes' properties would benefit from having both large- and small-diameter SWCNTs or even giving priority to narrow SWCNTs, as their optical and excitonic features lie in the detection range of most commonly used spectrometers.

2.2 Electronic structure of SWCNTs and their optical properties

2.2.1 Energy dispersion in 1D nanotube system

If ignoring the curvature effect, the electronic band structure of SWCNTs can be explained by using a graphene sheet [16; 22]. Therefore, the SWCNT can be regarded as a rectangular lattice with a $2N$-point basis, where N is the number of hexagons of the graphite honeycomb lattice that lie within the nanotube unit cell:

$$N = \frac{2\sqrt{n^2 + m^2 + nm}}{d_R} \qquad (2.3)$$

with d_R the greatest common divisor of $(2n+m)$ and $(2m+n)$ for a (n, m) nanotube.

2D graphene has a hexagonal first Brillouin zone (BZ) in the reciprocal space which contains the high symmetry points G, K and M [16]. The energy dispersion of graphene as a function of wavevector k is expressed as:

$$E_{2D}(\mathbf{k}) = \pm V_{pp\pi}[3 + 2\cos(\mathbf{k} \cdot \mathbf{a}_1) + 2\cos(\mathbf{k} \cdot \mathbf{a}_2) + 2\cos(\mathbf{k} \cdot \mathbf{a}_1 - \mathbf{k} \cdot \mathbf{a}_2)]^{1/2} \quad (2.4)$$

where $V_{pp\pi}$ is the nearest neighbour transfer integral, $\mathbf{a}_1$ and $\mathbf{a}_2$ are the basis vectors of graphene defined in **Section 2.1**.

The one-dimensional (1D) energy band of SWCNTs can be worked out from **eq 2.4**:

$$E_{1D}(\hat{k}) = \pm V_{pp\pi}[1 + 4\cos(\frac{\sqrt{3}\hat{k}_x}{2}a_0)\cos\frac{\hat{k}_y}{2}a_0 + 4\cos^2(\frac{\hat{k}_y}{2}a_0)]^{1/2} \qquad (2.5)$$

where $a_0 = \sqrt{3}a_{C-C} = 0.246$ nm.

The periodic boundary condition applies in the circumferential direction of nanotubes, which is, $\mathbf{C} \cdot \mathbf{k} = 2\pi q$, with $\mathbf{C}$ the chiral vector, $\mathbf{k}$ the vector along
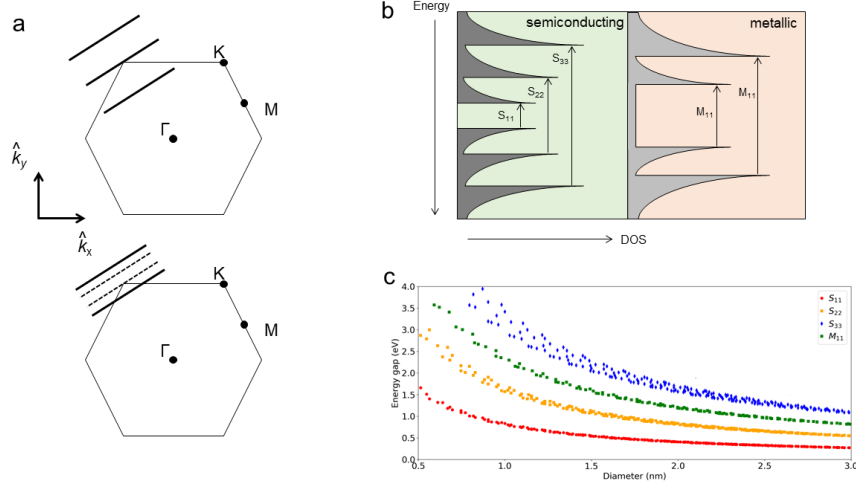
Figure 2.2: (a) The wave vector for metallic (top) and semiconducting (bottom) carbon nanotubes blueshown be the board cutting lines in the two-dimensional Brillouin zone of graphite. (b) DOS of SWCNTs including Van Hove singularities. The DOS were calculated by the approximation in **eq. 2.8**. (c) Optical transition energies of SWCNTs as a function of nanotube diameter, calculated based on the Kataura plot.

the circumferential direction and an integer [16; 23; 24]. This means there will be only a few selection of the N possible vectors in the circumferential direction of a nanotube. By substituting the allowed **k** into **eq 2.5**, the energy dispersion relation for a particular (n, m) SWCNT can be obtained. For metallic nanotubes, k vectors meet the boundary condition (shown as the bold solid lines in **Figure 2.2a**) intersect the K point in the BZ, for semiconducting nanotubes, K point present one-third of the distance between two bold lines (shown as the dashed lines in **Figure 2.2a**).

2.2.2 Density of states for carbon nanotubes

The density of states (DOS) per unit energy for a 1D system can be given as [25]:

$$D(E)dE = \frac{2 \parallel T \parallel}{\pi} \left(\frac{dE}{dk} \right)^{-1} dE \tag{2.6}$$

where $\parallel T \parallel$ is the amplitude of translational vector. Each peak, or energy band, of DOS is called a van Hove singularity (vHs).

Based on **eq 2.5** and **eq 2.6**, the simplified expression of DOS for SWCNTs is:

$$D(E)dE = \sum_{i}^{allbands} \frac{4}{\pi V_{pp\pi}\sqrt{3}} \frac{E}{\sqrt{E^2 - E_{cmini}^2}} dE \qquad (2.7)$$

where E_{cmini} is the conduction minimum for the given band. For metallic SWCNTs, according to the aforementioned boundary condition, bands will cross the Fermi level and as a result gives rise to a continuous DOS between the lowest conduction band (CB) and highest valence band (VB). The schematic of DOS for semiconducting and metallic SWCNTs is shown in **Figure 2.2b**.

2.2.3 Optical transition energy models

Optical transitions between different CBs and VBs are known as E_{ii}, with $i = 1, 2, 3, ...$ indicating the order of transition. If the electronic state of SWCNTs is specified, the terms M_{ii} and S_{ii} are used for the case of metallic and semiconducting nanotubes, respectively. The optical transition energies of SWCNTs are traditionally calculated in a single-electron approach by applying the tight-binding schemes [26]. However, such an approach doesn't take into account the curvature effect, which is crucial for the electronic structure of metallic SWCNTs. Due to a shift in momentum of the cutting line that would normally pass through the K point, non-armchair SWCNTs show the opening of a small band gap on the order of around 20 meV [27]. Additionally, tight-binding theory doesn't account for the C-C bond length variation and many-body corrections. It thus underscores the impact of the strong Coulomb interactions within SWCNTs on the optical transition energies. The transition energies (band gaps) of different (n, m) nanotubes calculated based on the tight-binding model are shown in a Kataura plot [24] (**Figure 2.2c**), for which a simple analytic expression can be given as:

$$E_{ii} = \frac{2i\gamma_0 a_{C-C}}{d_t} \qquad (2.8)$$

where $\gamma_0 = 2.7 - 3.0$ eV is the nearest-neighbour hopping energy.

In recent years, an empirical transition energy model was introduced [28], which shows a closer match with the experimentally determined energy values of SDS-dispersed SWCNTs:

$$\nu_{11(mod=1)} = \frac{10^7}{157.5 + 1066.9d_t} - 771\frac{\cos^{1.374}(3\theta)}{d_t^{2.272}} \tag{2.9}$$

$$\nu_{11(mod=2)} = \frac{10^7}{157.5 + 1066.9d_t} + 347\frac{\cos^{0.886}(3\theta)}{d_t^{2.129}} \tag{2.10}$$

$$\nu_{22(mod=1)} = \frac{10^7}{145.6 + 575.7d_t} + 1326\frac{\cos^{0.828}(3\theta)}{d_t^{1.809}} \tag{2.11}$$

$$\nu_{22(mod=2)} = \frac{10^7}{145.6 + 575.7d_t} + 1421\frac{\cos^{1.11}(3\theta)}{d_t^{2.497}} \tag{2.12}$$

2.2.4 Excitons in carbon nanotubes

In tightly confined 1D systems, the strong Coulomb force, inefficient screening and many-body interactions can effectively confine carriers and lead to the generation of excitons with large electron-hole binding energies for the excited electronic states [29; 30]. As single nanotubes can be isolated to avoid the effect of disorder and screening by the nearby substrate or gate, the field lines of Coulomb interaction lie unscreened in the vacuum, resulting in long-range interactions. In contrast, single-particle energy calculation based on the tight binding theory [26] does not take into account the effect of Coulomb interaction, it describes that the energies of single particles are not affected by dielectric screening. Such an electron-hole interaction results in a difference between the actual optical transition energies and those obtained based on one-particle interband theories.

Such a strong excitonic effect can dominate all optical processes in SWCNTs, including optical absorption, photoluminescence, Raman and Rayleigh scattering. For SWCNTs with diameters up to 2.1 nm, the size of exciton had been theoretically predicted to be on the order of 1-10 nm [31; 32]. Using results and insights from *ab initio* calculations, a symmetry-based variational method within the effective-mass and envelope-function approximations using tight-binding wave functions predicted the size of bright lowest-energy excitons to be: $\sigma = d_t(A + B\xi + C\xi^2)$, where d_t is the SWCNT diameter and $\xi = (-1)^v \cos 3\theta/d_t$ captures the chirality dependence (v is the $mod(2n + m, 3)$ value for a given (n, m) nanotube) [32]. A best fit to

modelled exciton size for SWCNTs with diameters between 0.5 and 1.3 nm is given by A=1.769, B=0.249 nm, and C=0.0913 nm^2. For (6,5) nanotubes with a d_t of 0.74 nm, the exciton size is estimated to be 1.35 nm, which is far less than the tube length (normally tens to hundreds of nm). Based on results from ultrafast pump-probe spectroscopy, the diffusion length of excitons (L_d) in SWCNTs was found to be about 100 nm in bundles and 1μm in monodispersed nanotubes, which has a dependence on the diffusion coefficient D and recombination lifetime τ based on $L_d = \sqrt{D\tau}$ [33; 34]. At high pump fluences, where an exciton-exciton annihilation process dominates, the typical exciton diffusion coefficient is on the order of 0.1 cm^2 s^{-1} [34; 35].

Compared to semiconducting SWCNTs, where the screening is weak, metallic SWCNTs contain a higher concentration of free charges and can weaken the electron-hole interaction by enhanced screening, leading to a lower exciton binding energy. According to both theoretical calculations and experimental optical characterizations, the exciton binding energies are from hundreds of meV to up to 1 eV in semiconducting nanotubes [29; 36; 37] and less than 100 meV in metallic nanotubes [36; 38; 39].

Two types of excitons can exist in SWCNTs: (1) bound excitons that lie within the optical gap (excitons associated with first-order transitions, *i.e.* E_{11}) and (2) resonant excitons that are embedded in the continuum of the lower energy bands (excitons associated with higher-order transitions, *i.e.* E_{22}, E_{33}, etc.). Bound excitons are produced by below-bandgap excitation and are stabilized without dissociation [40]. Resonant excitons are formed at higher excitation energies such as those of the electronic continuum and they resonantly couple to the continuum states, rapidly dissociate into free carriers and then re-associate into the lowest energy excitonic state by a step of fast inter-subband relaxation [41].

2.3 Chemical purification of SWCNTs

The as-synthesized SWCNTs usually simultaneously condense into thick bundles due to the van der Waals attraction force [42; 43], which increases the inhomogeneity in property and limits the commercial applications of SWCNT product.

Variations in the electronic structure and metallicity of (n, m) can lead to varied chemistries and reactivities. This enables the chemistry selectivity, or, in another word, makes the strength of interaction between different types of SWCNTs and molecules different. SWCNT chirality refinement can thus be achieved by isolating SWCNTs with surfactant micelle or conjungated copolymers under an intense
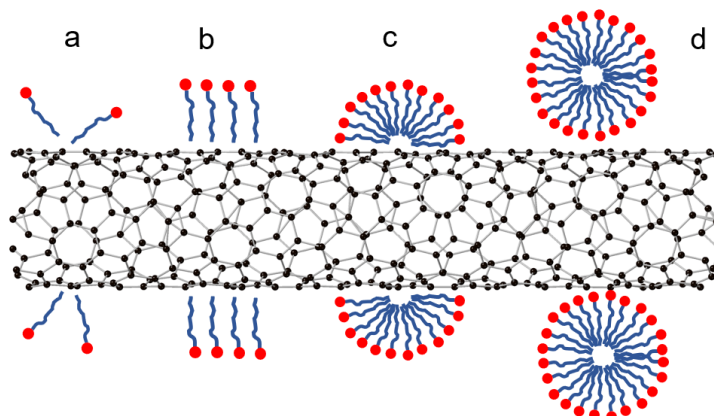
Figure 2.3: Schematic to representatively show the interaction of surfactant molecules with SWCNTs: (a) Random adsorption of surfactant molecules, (b) encapsulation in a cylindrical surfactant micelle, (c) hemimicellar adsorption and (d) Adsorption of micelles when approaching critical micelle concentration.

external energy input (*e.g.* ultrasound) in the liquid phase followed by a process of separation based on the difference in their chemical potential or physical properties. A most commonly applied type of surfactant used for isolating carbon nanotubes is sodium dodecyl sulfate (SDS), which provides a hydrophobic alkyl group and a hydrophilic -SO_4^- functional group while dissolved in water. Both experimental study [44] and theory based on molecular dynamic simulations [45; 46; 47] have demonstrated that the SDS molecules adsorbed around the carbon nanotubes can display different conformations depending on their concentration in the solution. Some basic structures these molecules form into include: (a) randomly adsorbed molecules; (b) cylindrical micelles; (c) hemimicellar adsorption and (d) adsorbed micelles, which are schematically shown in **Figure 2.3**. In addition to SDS, other types of ionic surfactant such as sodium dodecyl benzene sulfonate (SDBS), sodium cholate (SC) and sodium deoxycholate (DOC) have also been shown to effectively isolate carbon nanotubes [48; 49; 50; 51]. After the isolation of SWCNTs, a stabilized surfactant micelle coating with it hydrophilic group pointing outward will grow around them.

The nature of such a micelle coating could have a huge dependence on the electronic band structure of SWCNT. With this difference, enrichment of SWCNTs based on their chiralities can be achieved by several developed liquid-based separation techniques, such as density gradient ultracentrifugation (DGU) [52; 53; 54; 55; 56], aqueous two-phase (ATP) extraction [57; 58; 59; 60] and gel column chromatography [61; 62; 63].

Being a method widely used in biology for separating subcellular compo-
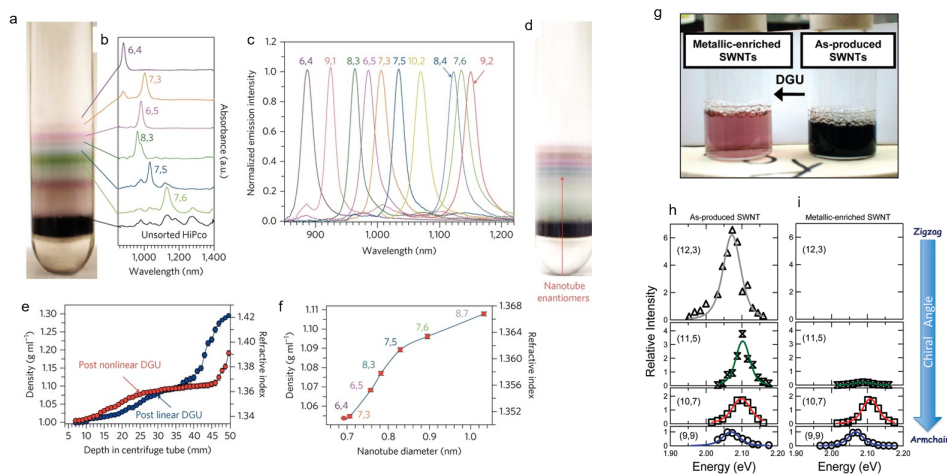
Figure 2.4: (a-f) Sorting HiPco SWCNTs based on the density-gradient ultracentrifugation (DGU) method. Reproduced with permission from ref [53] (ref. no.: 5378310669526). Copyright 2010 Springer Nature. (g-i) Refining metallic nanotubes from HiPco SWCNTs based on the DGU method. Reproduced with permission from ref [54]. Copyright 2010 American Chemical Society. Panel (g) and (i) are the resonant Raman excitation profiles (intensities of Raman scattering measured at varied excitation energies) of metallic nanotubes belonging to a $(2n + m) = 27$ family in the as-produced and metallic SWCNT-enriched samples, respectively. These plots indicate the population of each (n, m) nanotube species in the sample.

Figure 2.5: (a-c) Sorting small-diameter nanotubes from CoMoCAT SWCNTs based on the aqueous two-phase (ATP) extraction method. Reproduced with permission from ref [60]. Copyright 2019 American Chemical Soc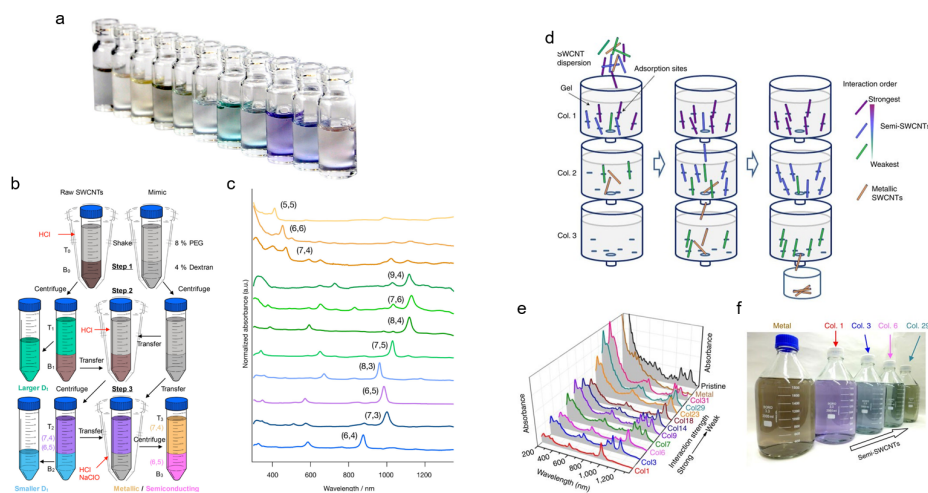iety. (d-f) Purifying HiPco SWCNTs based on the gel column chromatography method. Reproduced with permission from ref [61]. Copyright 2010 Springer Nature.

11

nents with differing buoyant densities, density-gradient ultracentrifugation (DGU) has now been applied to sort SWCNTs with different chiralities and bundle scales. Weisman's group adopted a nonlinear DGU method to successfully separate various (n,m) SWCNTs that have different handedness [53] (**Figure 2.4 a-f**). Kono's group achieved a high selectivity of armchair and near-armchair metallic SWCNTs by a DGU method applying sodium dodecyl sulfate (SDS) and sodium cholate (SC) as the surfactant [54] (**Figure 2.4 g-h**). Aqueous two-phase extraction (ATP) and gel column chromatography protocols had been reported by other research groups and the separation efficiency can now be improved to that of DGU method. SWCNT purification based on these sorting protocols can be exemplified by Flavel's [60] (**Figure 2.5 a-c**) and Kataura's [61] (**Figure 2.5 d-f**) work.

Apart from isolating SWCNTs with ionic surfactant molecules, polymer wrapping is also a widely used method to obtain nanotubes isolated to an individual state. Previous experiments had demonstrated that long-chain molecules such as poly(9,9-dioctylfluorene) (PFO)-based conjugated polymers [64; 65] (**Figure 2.6 a-c**), Pluronic and Tetronic block copolymers [66] and DNA [67; 68; 69] can effectively interact with SWCNT of a particular chirality or even resolve left- and right-handed nanotubes [67] (**Figure 2.6 d-g**).

2.4 Filling SWCNTs by the guest materials

Filling the central pore of a SWCNT with a guest material offers the additional benefit of creating an unconventional 1D nanostructure that cannot be directly synthesized in free space. Previous experimental works have shown that various kinds of materials, including pure metals[13; 70], metal chalcogenides [12; 71; 72; 73; 74; 75] (**Figure 2.7a**), metal halides [14; 76; 77], graphene nanoribbons[78] (**Figure 2.7b**), C_{60} [79], water molecules [80; 81], white phosphorus [11], iodine [82], dye molecules[10; 83] (**Figure 2.7c** and **d**) and alkane molecules [15] (**Figure 2.7e** and **f**), can be successfully encapsulated inside SWCNT nanotubes. When binary compounds crystallise inside narrow SWCNTs, the restricted volume leads to atomically-thin nanowires (NWs) that adopt different structures – such as linear chains,[74; 77] zig-zag chains [74] and helical chains [77] – depending on the SWCNT diameter.

It thus leads to an interesting question of how 1D NW/molecular chain filling can change the physical or chemical features (*e.g.* optical transitions, charge carrier generation) of the host nanotube and whether there is a possibility to investigate the properties of the filling materials themselves. A normal change that filling
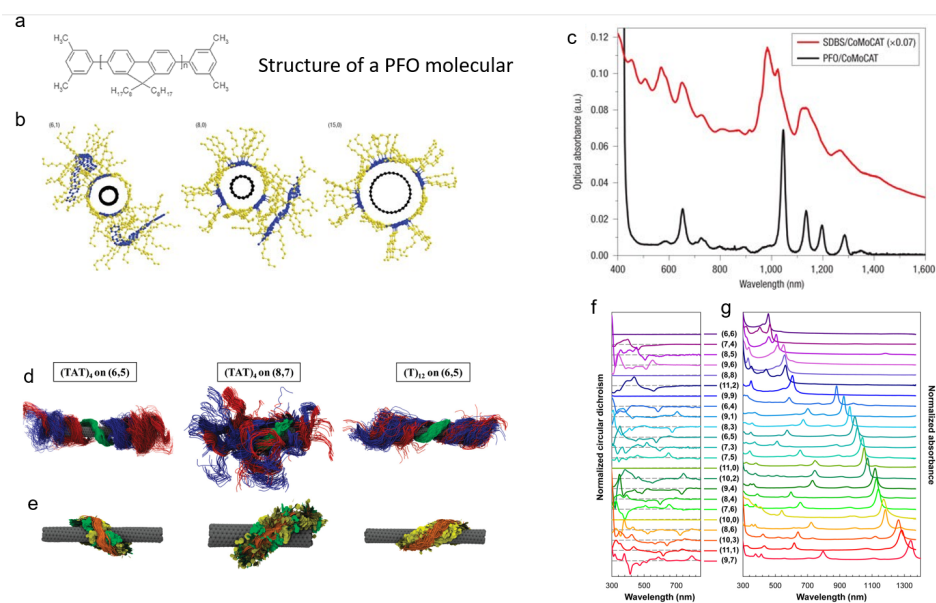
Figure 2.6: (a) Chemical structure of Poly[9,9-dioctylfluorenyl-2,7-diyl] end capped with Dimethylphenyl. (b) Model structures of three SWCNTs encased with PFO chains. (c) Typical steady-state absorption spectrum of CoMoCAT SWC-NTs wrapped by PFO compared to those isolated by Sodium Dodecyl Benzene Sulphonate (SDBS). Reproduced with permission from ref [64] (ref. no.: 5378311261717). Copyright 2007 Springer Nature. (d) Simulated structures of DNA multistrand hybrids over SWCNT surfaces. (e) Nucleic acid representations for their respective hybrid clusters. Reproduced with permission from ref [69]. Copyright 2012 American Chemical Society. (f,g) circular dichroism (CD) and steady-state absorption spectra of CoMoCAT SWCNTs sorted based on a DNA-assisted ATP method. Reproduced with permission from ref [67]. Copyright 2016 American Chemical Society.
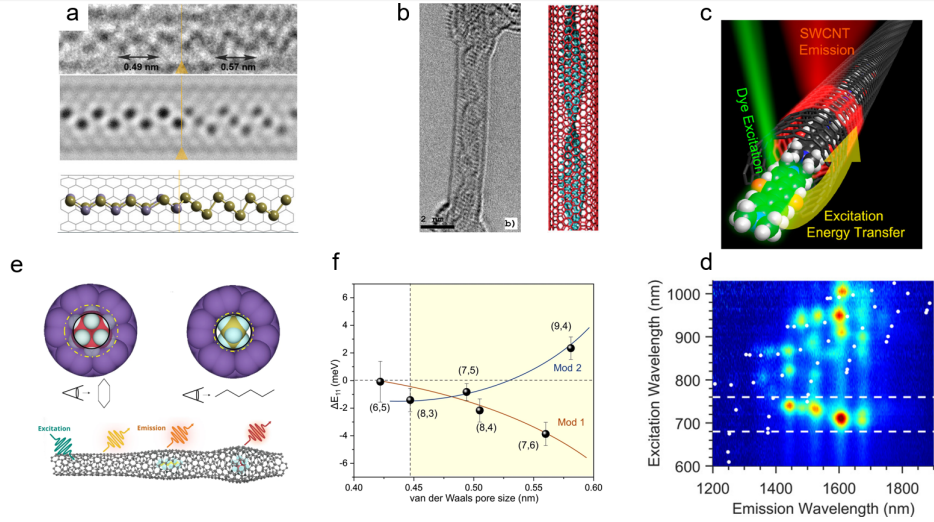
Figure 2.7: (a) Experimental image, simulated image and structure model of a SWCNT filled by the zig-zag SnTe chain (on left-hand side) and the coil-like Te chain (on right-hand side). Reproduced with permission from ref [74]. Copyright 2018 American Chemical Society. (b) Experimental image and structure model of a twisted coronenen-based Graphene Nanoribbons (GNRs) inside a nanotube. Reproduced with permission from ref [78]. Copyright 2011 American Chemical Society. (c,d) Structure and photoluminescence-excitation (PLE) features of SWC-NTs filled by 1,3-bis[4-(dimethylamino)phenyl]-squaraine (SQ) dye molecules. Emission features within the area highlighted by dashed lines in (d) originate from the exciton energy transfer (EET) from encapsulated dye molecules to surrounding SWCNTs. Reproduced with permission from ref [83]. Copyright 2018 American Chemical Society. (e) Structures of a (6,5) SWCNT filled by cyclohexane and b n-hexane. The filling of SWCNT by oversized molecules changes its structure and leads to red-shifted photoluminescence. (f) Differences in photoluminescence energies between cyclohexane (99.9%)- and n-hexane-incubated end-opened SWCNTs ($\Delta E_{11} = E_{11,cyclohexane} - E_{11,n-hexane}$) plotted as a function of the van der Waals pore size of the nanotubes. Both n-hexane and cyclohexane can fit in those nanotube pores in the yellow colored area, while only n-hexane can enter the (6,5)-SWCNT pore. Solid curves show the trend of variation for $mod = 1$ and $mod = 2$ (n, m). Reproduced with permission from ref [84]. Copyright 2021 Springer Nature.

14

can bring to the SWCNT is the spectral shift of its excitonic features and Raman modes. Filling SWCNTs by water molecules had been shown to lead to a slight red-shifting and broadening of the S_{11} emission peak [85]. Accordingly, the time-resolved photoluminescence decay of the materials revealed that the short-living component had a shortened radiative lifetime after filling. The effect of water filling was then attributed to a change of the internal dielectric environment of SWCNT [85]. A study based on density functional theory (DFT) found that water filling can lead to a voltage generation between the tube ends due to the interactions between the water dipole chains and charge carriers from the SWCNTs [86].

A quantitative analysis of the effect of materials filling on the electronic structure of SWCNTs can be exemplified by the study conducted by Qu et al [84]. By comparing the fluorescence of various (n, m) nanotube species (e.g., (6,5), (7,5), (7,6)) which were unfilled (end-capped) and filled by alkane molecules (cyclohexane and n-hexane), they demonstrated a dependence of PL position shift on the radial strain on SWCNTs induced by nanotube filling (**Figure 2.7f**). Such a strain effect can be expressed as:

$$\Delta E_{ii} = (-1)^{i+1}(-1)^{k+1}3t_0\sigma\sin 3\theta \qquad (2.13)$$

where ΔE_{ii} is the shift in the excitonic transition energy, i is the transition order ($i = 1, 2, 3, ...$ for the E_{11}, E_{22}, E_{33},... transitions), k is the mod index which equals $mod(n - m, 3)$, θ is the chiral angle and t_0 is estimated to be 3 eV. σ is the radial strain due to nanotube filling. Significantly, this model suggests that type-I ($mod = 1$) and type-II ($mod = 2$) SWCNTs will show an excitonic energy shift in the opposite direction.

Compared to water molecules, filling SWCNTs by metal halide chains had been shown to result in a more significant change in their spectra. Eliseev et al. had found that filling the medium-sized SWCNTs ($\sim$1.2-1.7 nm) with CuX and AgX (X = Cl, Br and I) NWs can lead to a relatively more significant change in their Raman modes, with a blue-shift of RBM and tangential (G) modes by up to 8 and 23 cm^{-1} being discovered. With analyses based on XPS, near-edge X-ray absorption spectroscopy (NEXAS) and valence band spectra, they revealed an acceptor behavior of these halogenide NWs and a charge transfer from the SWCNT to them [76; 14].

Studying the energy flows between the filling materials and the host carbon nanotubes can be useful for the design of future light-harvesting materials. A

common way of such energy convergence within the low-dimensional nanomaterials is exciton energy transfer (EET) [87; 88; 89; 90], which has been broadly seen in the carbon nanotube bundles [87; 88]. In a system where EET occurs, a pair of molecules act as the energy donor and acceptor. The rate of EET can be found from a change in the quantum yield (QY) of donor molecules, of which the relation can be given as:

$$n = \frac{Q_{PL}}{Q_{PL,0}} = \frac{k_r + k_{nr}}{k_r + k_{nr} + k_{ET}} \tag{2.14}$$

where Q_{PL} and $Q_{PL,0}$ are the photoluminescence quantum yield (PLQY) of donor molecular with and without the presence of acceptor molecular, n is the ratio between the two QY values, k_r, k_{nr} and k_{ET} are the rates of radiative recombination, non-radiative recombination and EET.

In recent years, exciton energy transfer (EET) in filled SWCNT systems has been studied. Based on evidence found by the photoluminescence characterization, an energy transfer from the encapsulated dye molecules to the outside SWCNTs has been demonstrated [10; 83] (**Figure 2.7d**). These discoveries demonstrated the promise of filled SWCNTs as a light harvester with an active wavelength range from the UV to up to the mid-infrared.

2.5   Functionalization of the SWCNTs

SWCNTs can interact with polymers or dye molecules through a noncovalent and a covalent manner. The noncovalent nanotube-polymer interaction, known to be achieved through $\pi - \pi$ attraction [91], is exemplified by exfoliating the nanotubes with small molecules such as SDS or wrapping the nanotubes surface by conjugated copolymers that have a significantly larger molecular weight. Due to the covalent bond-free nature of such a strategy, the effect of defect generation on carbon nanotubes that hinders determination of their intrinsic features can be minimised. In recent years, efficient individualization of nanotubes and chirality selection have been achieved based on various types of copolymers, such as poly(9,9-dioctylfluorene) (PFO) [64; 65], poly(9,9-di-n-dodecylfluorene) (PFD) [92] and poly(9,9-dioctylfluorene-alt-benzothiadiazole) (F8BT) [93]. The breakthroughs in elucidating the relation between polymer structure and nanotube selectivity can provide the opportunity for a large-scale production of valuable SWCNT-based materials, which paves the way for developing advanced electronic nanodevices

[94; 95; 96; 97].

sp^3-functionalization of SWCNTs is a method to introduce covalently bound species onto the nanotube side walls and result in the creation of sp^3 defects. The chemicals applied so far to achieve the functionalization include oxygen [53], diazonium salts [98], molecules with alkyl groups [99] and aromatic compounds [100]. Due to the introduction of fluorescent defects, an outcome of such functionalization is the creation of an exciton trap state on the lower-energy side of the E_{11} excitonic state, which gives rise to an additional fluorescence features known as E_{11}^- and E_{11}^-*. The quantitative change in the SWCNT band structure due to these photo-active defects can lead to promising features such as exciton localization and upconversion [101]. It was also discovered that the configuration of functional groups can be modified based on a change of solvent type during the defect formation, enabling a wider spectral window of the materials towards telecom wavelengths [102].

2.6   Doping the carbon nanotubes

Post-chemical processing and surface functionalization can usually lead to a p- (nanotubes receive holes) or n-type (receive electrons) doping of carbon nanotubes, which is desirable for semiconductor devices. While p-type doping is normal to carbon nanotubes as they can readily accept holes from naturally absorbed oxygen [103], n-type doping is relatively non-trivial and can't last for long in air. Previously discovered methods to turn carbon nanotubes into a n-type are mostly based on introducing n-type dopant such as alkali metal [104], nitrogen-containing molecules [105; 106] or supramolecular salts [107] outside of them. A precise control of the electrical conductivity and thermoelectric charge carrier property achieved by such a doping strategy can offer a potential avenue for producing high-performance carbon nanotube-based electronics [104; 105; 106; 107; 108].

2.7   Summary

Single-walled carbon nanotubes (SWCNTs) are regarded as rolled-up 2D graphene, whose electronic properties can be changed sensitively by structure modifications (*e.g.* diameter, chiral angle). Due to the polydispersive nature and a lack of uniformity of the as-synthesized SWCNTs, commercial applications of them are limited. Rapid development of the techniques to isolate and separate nanotubes has enabled discrimination of carbon nanotubes by their chiralities and sizes, which enable bulk materials of monodispersed SWCNTs to be produced.

Functionalization of carbon nanotubes offers additional degrees of freedom to tune their physiochemical and optical properties. Such a strategy can be achieved either through non-covalent interaction with surfactant molecules or conjugated copolymers, or by introducing covalently bound species on the SWCNT side wall. Besides nanotube functionalization, filling SWCNTs by the guest material has also been achieved in recent decades, which raised concerns of investigating the potential interaction between the encapsulated 1D structure and the host nanotube.

With a high tunability of the optical and electronic properties due to physical variations provided by the structure diversity and the feasibility of functionalization or filling, SWCNTs and SWCNT-containing materials have a vast range of proposed applications including transistors, logic gates, photonics and electronics. It is foreseen that the large-scale production of SWCNTs with high values, *i.e.* having a substantially large degree of structure and dispersivity control, can be a focus of future works in the field.

Chapter 3

Characterization Techniques and Equipment

In this chapter we introduce the characterizing techniques used in this study. The properties of materials were investigated by both electron microscopy and optical spectroscopy.

3.1   A list of equipment and operation parameters

Various types of characterization methods were carried out in this study to investigate the structure and optical properties of materials. For investigations on the atomic structure of NW-filled SWCNTs, high-resolution transmission electron microscopy (HRTEM) and annular dark-field scanning transmission electron microscope (ADF-STEM) based on a doubly aberration-corrected (AC) instrument were applied. An electron acceleration voltage of 200 kV was used throughout nearly all of the experiments. Although such a relatively high voltage means a large electron dose (number of electrons per area and time) and can potentially induce the knock-on damage (an elastic scattering process occurred when the incident electron beam interact with the sample material and knock the nuclei out from it to create defects) on the sample [91], we observed that the atomic NWs and carbon nanotubes can retain a stabilized conformation over the duration of multiple scans (staying in the same sample region for up to 5 min).

The morphology and topography of materials (e.g., thin films produced by vacuum filtration) were studied by scanning electron microscopy (SEM) and atomic force microscopy (AFM). Examination of the chemical composition of materials was conducted based on the energy dispersive X-ray analysis (EDX) operated during

SEM or STEM measurement. The effects of NW filling on the chemical and optical properties of SWCNTs were studied by steady-state, time-resolved and X-ray spectroscopy. A list of the equipment applied for this study and their explanations is shown as follows:

Table 3.1: Characterization instruments and operation parameters

Name	Brand	Use	Parameters
HRTEM	JEOL ARM 200F & JEOL JEM-2100	analysing the nanostructure of material	Electron voltage: 200 kV
ADF-STEM	JEOL ARM 200F	Analyze the atom conformation of material.	Electron voltage: 200 kV, collection semi-angle: 35-180 mrad
SAED	JEOL ARM 200F	Study the crystal structure and phase.	
SEM	Zeiss Gemini	Analyze the morphology of film-state materials.	Electron voltage: 0.3-10 kV
EDX	Zeiss Gemini	Chemical composition investigation.	Signal collection depends on the working distance in SEM and tilt angle of sample specimen in TEM.
XPS		Study the chemical composition and elemental valence.	
UV-Vis-NIR absorption	PerkinElmer LAMBDA1050	Analyze sample optical absorption features.	Scattered signals are analyzed by the integrating sphere.

PL	HORIBA Fluorolog-3	Analyze the fluorescence of sample.	Excitation ranges and gratings: 330-800 nm (1200 grooves/mm), 800-1000 nm (600 grooves/mm)
Raman spectroscopy	Renishaw In-Via Reflex & HORIBA LabRam HR Evolution	Investigate the Raman scattering features of samples. & output power 2.5 mW. Use a focal lens with a numerical aperture (N.A.) of 0.9 for nearly all excitation wavelengths except 325 nm (using a UV-enhanced lens with an N.A. of 0.4)	
FTIR	Bruker Vertex 70V	Analyze the far-infrared absorption of samples.	Detect both MIR (6000-400 cm^{-1}) and FIR (400-130 cm^{-1} ranges.
THz-TDS	-	Analyze the far-infrared absorption of samples down to <1 THz.	THz beam are generated by the photoconductive emitter and detected by the ZnTe crystal.
Transient absorption	-	Analyze the exciton and charge carrier decay dynamics on a time scale of down to <20 fs.	white light supercontinuum is generated by a CaF_2 (330-720 nm) or a sapphire (720-1100 nm) crystal.
OPTP	-	Analyze the charge carrier decay dynamics.	

Temperature controller for Raman	Linkim TSHM600	Control temperature for Raman measurements.	Temperature range: 20-400 °C, ramp rate: 40 °C per minute
Temperature controller for PL	Oxford Optistat	Control temperature for the PL measurements.	Measurement temperature: $\sim$80 K
Plasma cleaner	diener	Clean the sample surface by plasma treatment.	-

3.2   Abberation-corrected TEM and STEM

A transmission electron microscope (TEM) employs a high voltage to generate the electron beam and contains several components such as electromagnetic lenses, deflectors and aperture to manipulate it. As the electron beam passes the sample specimen, part of it transmits through to form an image of the sample whilst the rest part diffracts and is focused into a set of spots on the back focal plane of the lens behind the sample specimen, known as the diffraction pattern. A scanning transmission electron microscope (STEM) is a conventional TEM equipped with additional components such as scan coils and detectors to capture the bright-field (BF), annular dark-field (ADF) and high-angle annular dark-field (HAADF) images. It employs an aperture behind the lens before sample specimen to focus the electron beam to a tiny spot and records an image as the focused electron beam (called the probe beam) is rastering across the sample region. For the Jeol ARM 200F TEM, the aberration is corrected in both of the probe-forming (in STEM mode) and image-forming (in conventional TEM mode) optics, allowing characterization with an atomic resolution in both of the STEM and conventional TEM mode. A schematic to describe the principle of TEM, selected area electron diffraction (SAED) and STEM is shown in **Figure 3.1**.

The detection limit (smallest probed distance) of a TEM is defined by the Rayleigh criterion:

$$\delta = \frac{0.61\lambda}{\mu \sin \beta} \tag{3.1}$$

where λ is the wavelength of electron beam, μ the refractive index of view medium and β the collection semi-angle. Due to the fact that electrons in TEM are accelerated by the electrostatic potential drop, the higher the potential (acceleration voltage) means the shorter the wavelength λ. This will provide a smaller detection limit. Also, the above theories and principles make it clear that imaging at the focus (corresponding to the largest collection semi-angle) will provide the smallest detection limit but the lowest contrast, whilst imaging at an over- or under-focused condition (corresponding to a relatively smaller collection semi-angle) will improve the contrast but at the cost of resolution. Additionally, other issues such as abberation, sample inhomogeneity (thickness variation, specimen tilting) and electron dose variation can also lower the quality of images. Since the materials studied here are treated by the liquid-phase processing, there are further problems of sample contamination due to the surfactant molecules. We found that the existence of these organic compounds can cause hydrocarbon contamination build up and seriously reduce the image resolution. To avoid such issues, the TEM samples were baked in an vacuum oven at 100-150 °C for 12 h prior to characterization and beam showering was conducted before image acquisition.

For the general TEM or ADF-STEM imaging carried out in this study, the pixel dwell time was chosen to be 5, 10 and 20 μs for the search, preview and capture modes. ADF-STEM measurement was conducted by inserting a 30 μm condenser lens in the electron beam path, which reduced the current density to about 0.2 pA·cm^{-2} on the fluorescence screen.

3.3 AFM Morphology and Mechanical Property Measurements

In AFM a sharp probe (cantilever) is brought into close proximity to a sample with aims to acquire the interaction force between the cantilever tip and the material surface. Such a kind of force can result in the displacement of the tip, which can be monitored by detecting the position change of a laser beam reflected off the back of a cantilever, known as a beam-bounce scheme. The displacement change while the tip interacts with the sample surface can be given once a setpoint value (or imaging force) is defined. In AFM a propotional-integral-differential (PID) feedback
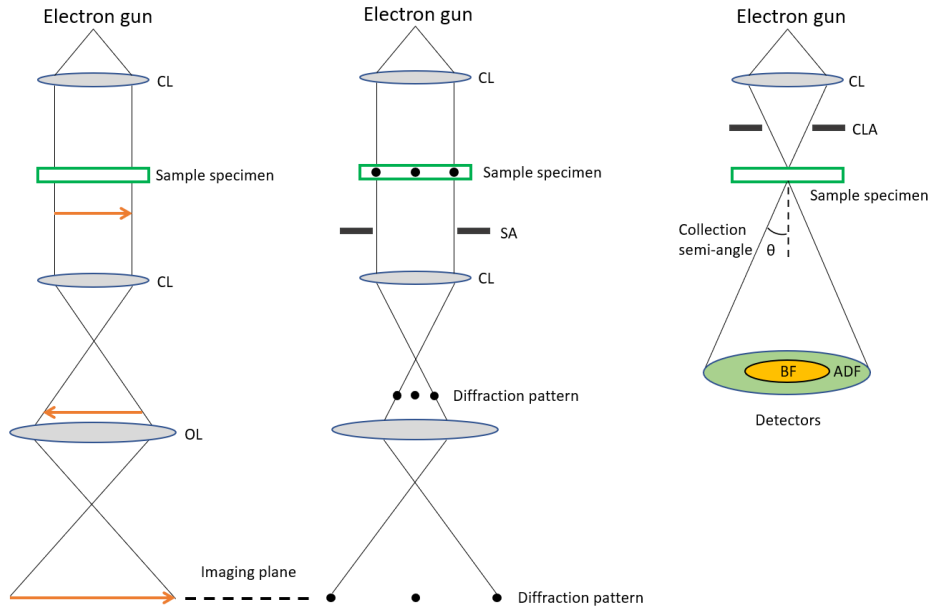
Figure 3.1: Schematic of TEM operated in different modes: conventional bright-field imaging, electron diffraction and scanning mode. Aberrations in the figure: CL-condenser lens, CLA-condenser lens aperture, OL-objective lens, SA-selected area aperture, BF-bright field, ADF-annular dark field.

controller can drive the z-piezo to optimize the setpoint value to better match with the real-time signals. The processes can be illustratively shown in **Figure 3.2a**.

The most common scan mode for an AFM is the tapping mode, which requires the cantilever to oscillate at its resonant frequency (normally up to hundreds of kHz). The disadvantage of such a scan mode is the frequent change of the setpoint value while scanning over an homogeneous surface (*e.g.* a sample with both hard and soft regimes), which then causes a dramatic change of the cantilever dynamics and introduce noise to the scan.

The AFM system applied in this study adopts a non-resonant scan mode known as peak-force tapping, which allows the cantilever to oscillate at a frequency of 1-8 kHz. The benefits of such a method are the application of a relatively low setpoint force value (down to <1 nN) and the ability to detect the deflection (or the force) during the tip engagement and withdrawal (**Figure 3.2b**) on each pixel of the scan. Additionally, the peak-force tapping method enables the quantum nanomechanical (QNM) properties of materials, including Young's modulus, adhesion, dissipation and deformation to be directly measured.

For the AFM experiments conducted here, the peak-force tapping mode was adopted and the nanomechanical properties of materials were analyzed. With the
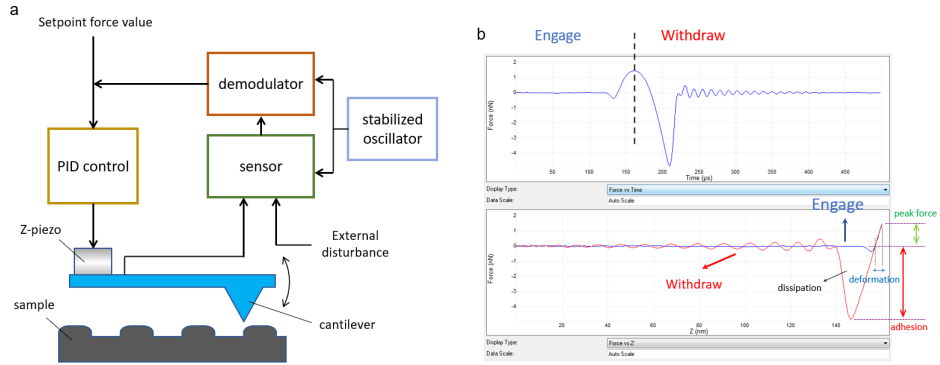
Figure 3.2: (a) Principle of AFM. (b) Force on the cantilever tip as a function of time and height. During tapping, the tip experiences an engaging and a withdrawing period, where different types of signals can be extracted.

help of these characterizations, the homogeneity of SWCNTs after the filling and chemical treatments which can be affected by the coexistence of surfactant aggregates or inorganic particles was investigated.

Knowing the actual dimension of individual SWCNTs is important to the accurate estimation of their excitonic and optical properties (*e.g.* plasmon resonance frequency is related to both of the nanotube diameter and length [109; 110]). To allow the actual morphology of individualized nanotubes to be characterized, the AFM samples are prepared by drop-casting or spin-coating the solution-state nanotubes on the quartz substrate followed by removal of the excess surfactant molecules based on a washing protocol. In prior to the sample washing, a plasma clean treatment was applied. The plasma-cleaned sample was then washed three times by isoproponal and once by DI water. The resolution of AFM is limited by the radius of the cantilever tip (2-12 nm for the Scanasyst-Air SiN cantilever used here throughout the study). Only the height signals were used for the determination of diameters of isolated nanotubes (~ 1 nm).

3.3.1 SEM and EDX analysis

The chemical compositions of the SWCNT samples were studied by X-ray energy dispersive spectroscopic (EDX) characterization based on a Zeiss Gemini scanning electron microscope (SEM) equipped with a silicon drift detector. The principle of EDX characterization is described here. Upon irradiation by the electron beam, an electron on the inner shell of an atom can be excited and ejected from it, with another electron on the outer and higher-energy shell filling the hole left on this

inner shell. The difference in energy between the higher-energy shell and the lower energy shell is then released in the form of an X-ray and its energies which indicate the atomic structure of an element are then detected by EDX, yielding the chemical and elemental information of the sample.

For conventional morphology measurement, a low electron acceleration voltage of less than 1 kV was used and images were capsuled by an 'InLens' detector. For chemical analysis by EDX, a high acceleration voltage of 20 kV and a sufficiently long working distance of 8.5 cm were applied in order to collect enough X-ray signal.

3.4 Steady-state spectroscopic measurements

3.4.1 UV-vis-NIR absorption

The absorption features associated with excitonic transitions of SWCNTs (E_{11}, E_{22}, E_{33}, etc.) which present in the UV-Vis-NIR wavelength regime were measured by a PerkinElmer LAMBDA1050 spectrometer. The instrument was equipped with a deuterium and a tunsten halogen lamp as the light source, and a photomultiplier (PMT), a peltier-controlled InGaAs and a PbS detector to characterize the signals from 175 nm to 1500 nm. Different types of materials were tested for this study, including solution-state, gelatin-embedded and filtrated thin film samples. For solution-state SWCNTs and filtrated thin films, pure SDS aqueous medium of the same concentration and quartz substrate of the same thickness were applied as the references for background subtraction. For gelatin-embedded samples, only the substrate was used as the reference due to the difficulty of accurately controlling the thickness of gelatin film. A spectrum of the substrate with the pure gelatin film was then taken and rescaled with respect to the spectrum of SWCNT-containing film sample for the estimation of the background level.

3.4.2 Photoluminescence excitation (PLE)

Photoluminescence of carbon nanotubes is generated by interband recombination of the electron-hole pairs [111]. Because of the very fast inter-subband relaxation (*e.g.* from E_{22} to E_{11} or E_{33} to E_{22}), which had been determined to be on a timescale of ~ 40 fs [40], photoluminescence on the E_{11} excitonic state will dominate in SWCNTs. Due to the presence of an exceptionally high density of states at van Hove Singularities (vHSs), prominent fluorescence would be induced following light absorption at photon energies E_{ii}, as shown in **Figure 3.3a**. Apart from the resonant excitation at E_{ii}, other origins of photoluminescence in SWCNTs include
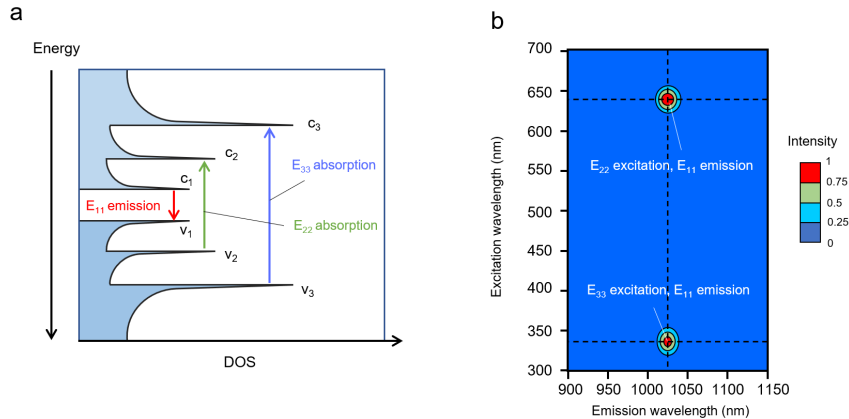
Figure 3.3: (a) Schematic diagram of the density of states and van Hove singularities of a semiconducting SWCNT. Vertical upward green and blue arrows depict the optical excitations with energies E_{22} and E_{33}. Red downward arrow denotes photoluminescence generation due to E_{11} emission transition. (b) Typical photoluminescence excitation (PLE) map of a SWCNT sample containing only (7,5) nanotubes. The two signal maxima are attributed to the photoluminescence following E_{22} and E_{33} resonant excitation.

the existence of exciton-phonon bound states [112], exciton energy transfer [87] and non-resonance absorption [113].

In the study here, we characterized the photoluminescence of SWCNTs following excitation in a wide range of wavelengths. In this way, a photoluminescence-excitation (PLE) 2D contour map showing the variation of fluorescence intensity against both the excitation and emission wavelengths can be generated. Because of the fast internal relaxation to the available states below the first excitonic state, photoluminescence of the metallic SWCNTs cannot be detected. The PLE map thus only provides the information of semiconducting SWCNTs. After obtaining the experimental E_{ii} wavelengths for a SWCNT species of interest from PLE contour map and converting them to energies, the chirality of a nanotube can be determined by matching these energies to the theoretical energies of a certain (n, m) nanotube calculated based on the empirical transition energy model introduced in **Section 2.2** [28]. The PLE map of a SWCNT sample containing only semiconducting (7,5) nanotubes is illustratively shown by **Figure 3.3b**. The photoluminescence is seen at an emission wavelength of ~ 1024 nm, which corresponds to the wavelength of E_{11} excitonic state of (7,5) SWCNTs. The fluorescence maximum encountered at the excitation wavelengths of ~ 645 nm and ~ 340 nm are induced by the E_{22} and E_{33} resonant excitation, respectively.

A HORIBA Fluorolog-3 spectrometer equipped with a Xenon lamp that gen-

27

erated a broadband excitation beam was employed for the PLE measurements. A single-grating monochromator was applied to select the excitation wavelength. A single photon-counting PMT detector was used to detect fluorescence signals in the near-infrared (850-1350 nm) wavelengths. The spectrometer corrected for variations in the lamp output (by counting excitation signals from a silicon photodiode detector) and the detector monochromator's sensitivity. The solution-state SWCNT sample was loaded into a cuvette with 1 cm path length for the measurement. The fluorescence of solutions and thin films were collected in a right-angle and a front-face geometry, respectively. A band-pass filter with nearly 100 % transmittance between 332-807 nm was placed after the excitation grating slit. A NIR long-pass glass filter was placed before the emission grating slit to block Rayleigh scattering signals. To characterize the phonon sidebands of the SWCNTs, measurements were carried out at excitation wavelengths between 850 nm and 1000 nm, which required changing the excitation grating from 1200 grooves/mm to 600 grooves/mm. According to the relation between nanotube diameter and the wavelength of their optical transitions [28], the wavelengths of E_{11} for semiconducting SWCNTs smaller than 1 nm are less than 1300 nm. The spectrometer is capable of detecting the photoluminescence from these narrow SWCNTs.

Low-temperature photoluminescence of the gelatin-embedded SWCNT films was characterized based on a cryostat (Oxford Optistat) which allowed the temperature to be maintained at 80 K.

3.4.3 Fourier transform infrared spectroscopy (FTIR)

The MIR and FIR absorbance of the SWCNT thin film was examined by a Bruker Vertex 70V Fourier-transform infrared spectrometer (130-2500 cm^{-1} or 0.016-0.31 eV). The measurements were taken in a transmission geometry with a DLaTGS detector being used to collect the signals. The FIR (130-400 cm^{-1}) and MIR (400-6000 cm^{-1}) excitation beams were selected by a silicon and a KBr splitter, respectively. An aperture size of 3 mm was used throughout the experiments.

3.4.4 Time-domain terahertz spectroscopy (THz-TDS)

Terahertz (THz) radiation incident onto a finite-length metallic or doped semiconducting SWCNT launches collective charge oscillations along the nanotube axis, driving electrons and holes along opposite directions of a tube, which are known as plasmons [110; 114; 115]. The created electric dipole generate an electric field opposing the incident electromagnetic field, which is known as the depolarization

field. The charge carriers on SWCNTs are forced to undergo harmonic oscillation as a result of not only the applied electromagnetic field but also the electrostatic restoring force arising from the depolarization field. This makes the conductivity of SWCNTs in the far-infrared and THz regimes to be modelled by plasmon resonance [115]. It can be described by a Lorentzian model, for which the frequency-dependent conductivity of carbon nanotubes is given as:

$$\sigma(\omega) = \frac{Ne}{m^*} \frac{i\gamma_p}{\omega^2 - \omega_0^2 + i\omega\gamma_p} \tag{3.2}$$

where N is the density of charge carriers, $e = 1.602 \times 10^{19}$ C is electron charge, m^* is the effective mass of charge carriers, ω_0 is the plasmon resonance frequency and γ_p is the phenomenological scattering rate for the plasmon response.

The plasmon resonance frequency ω_0 is related to the geometry, dielectric constants and charge carrier density N:

$$\omega_0 = \sqrt{g\frac{Ne^2}{\epsilon_0 m^*}} \tag{3.3}$$

with g representing a factor related to the geometry and the dielectric constants of SWCNTs and surrounding medium. $\epsilon_0 = 8.854 \times 10^{-12}$ Fm^{-1} is the dielectric permittivity of free space.

To characterize the free carrier properties and conductivity of SWCNTs, a THz-TDS setup measuring absorbance within frequencies of 0.2-3 THz was applied. The THz-TDS setup and characterizing method here are similar to those applied in the research work previously conducted by our group [116; 117; 118]. In specific, the femtosecond (fs) laser beam generated by a MaiTai laser was split into a pump and a probe beam. The pump beam was focused on a THz emitter, which was a photoconductive antenna (PCA) consisting of a substrate of gallium arsenide (GaAs) and two parallel gold electrodes deposited on it, to generate THz pulses. The THz radiation was focused onto the test sample and then onto the detector by off-axis parabolic (OAP) mirrors. The detection of THz beam was based on electro-optic sampling. The probe beam gates the detector, which responses to the amplitude and sign of the electric field of the THz pulse. The detection system consists of an electro-optic crystal (zinc telluride (ZnTe) for the experiments here), a quarter wave ($\lambda/4$ plate, the Wollaston prism and balanced photodiode. The principle of THz radiation detection is as follows: when THz pulse arrives in the electro-optic crystal,

its birefringence is changed, resulting in the modulation of the phase of the probe beam. The $\lambda/4$ plate turns the probe beam from linearly polarized to circularly polarized (elliptically polarized if there is a phase shift caused by the THz pulse). Afterwards, the probe beam is split into two orthogonal components by a Wollaston prism, which are sent into the balanced photodiodes and are converted into the current signals. A lock-in amplifier characterizes the difference in the intensities of these two components measured by the photodiodes. This difference is proportional to the field strength of THz pulse arriving into the electro-optic crystal. By changing the time delay of the pump beam relative to that of the probe beam based on a mechanical delay stage, a time profile of the THz field strength (time-domain waveform) can be obtained. By fast Fourier transform (FFT), complex transmission coefficient as a function of frequency corresponding to the ratio of electric fields for tests on the sample and reference materials, $T(\omega) = E_{sample}/E_{ref}$, can be obtained.

3.5 Time-resolved spectroscopic measurements

3.5.1 Transient absorption spectroscopy

The transient dynamics of excitons in the SWCNT samples were examined by transient absorption (TA) spectroscopy. After the SWCNTs are excited by the pump beam, it shows a reduced ground-state absorbance as the ground state is partially depopulated (**Figure 3.4**). Therefore, the occurrence of reduced absorbance of the probe pulse is called ground-state bleach (GSB) or photo-bleaching (PB), which leads to negative differential absorbance ($\Delta A < 0$) at the spectral positions of the steady-state absorption bands (**Figure 3.5a**). When the interaction with the probe pulse further promotes an already excited SWCNT to a higher-lying excited state, the decrease in the probe's intensity due to the excited state absorption (ESA) leads to positive differential absorbance ($\Delta A > 0$) at probe energies corresponding to the energy difference between the higher-lying excited state and the lower-lying excited state (**Figure 3.4** and **Figure 3.5b**). Alternatively, a shift in the transient frequency can also lead to positive and negative differential absorbance (**Figure 3.5c**).

For the measurement, a pump beam and a probe beam were derived from the optical parametric amplifiers (TOPAS) which were seeded with 1 kHz, 40 fs, 800 nm pulses generated by doubly amplified Ti:Sapphire laser (Newport Spectra Physics Spitfire Ace PA). The pump beam was mechanically chopped at 500 Hz. Different white light probe continuua (330-720 nm and 700-1100 nm) were produced from a CaF_2 crystal pumped at 800 nm, and a sapphire crystal pumped at 1300 nm,
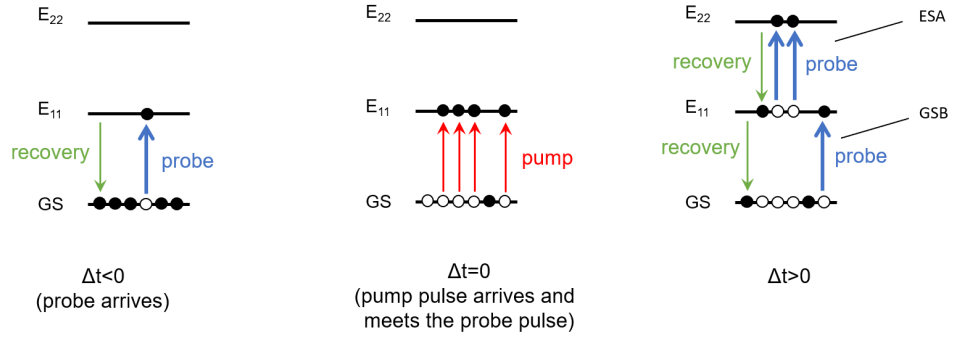
Figure 3.4: Schematic diagrams describing the different types of signal responses in TA. Red and blue upward arrows denote the pump and probe, respectively. Green downward arrow denotes the recovery of the population.
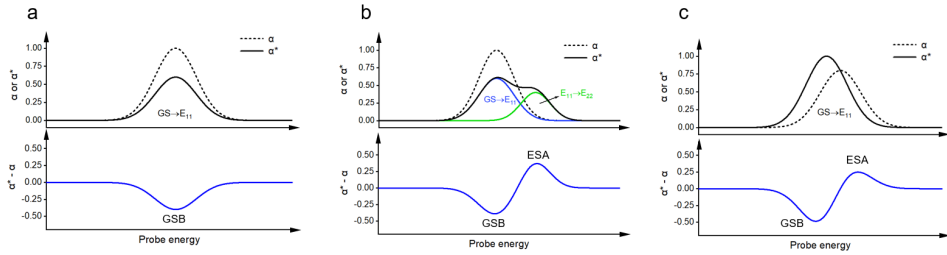
Figure 3.5: Schematic diagrams showing the generation of negative and positive TA signal responses. α and α^* stand for the absorption coefficients of SWCNT at the equilibrium and the photoexcited state, respectively. (a) Depopulation of the ground state leads to decreased absorbance of the probe beam and causes ground-state bleach (GSB). (b) Excitation of a nanotube from the lower-lying excited state (E_{11}) to the higher-lying excited state (E_{22}) leads to increased absorbance of the probe beam and results in excited state absorption (ESA). (c) A shift of the temporal frequency can also give rise to negative and positive differential absorbance.
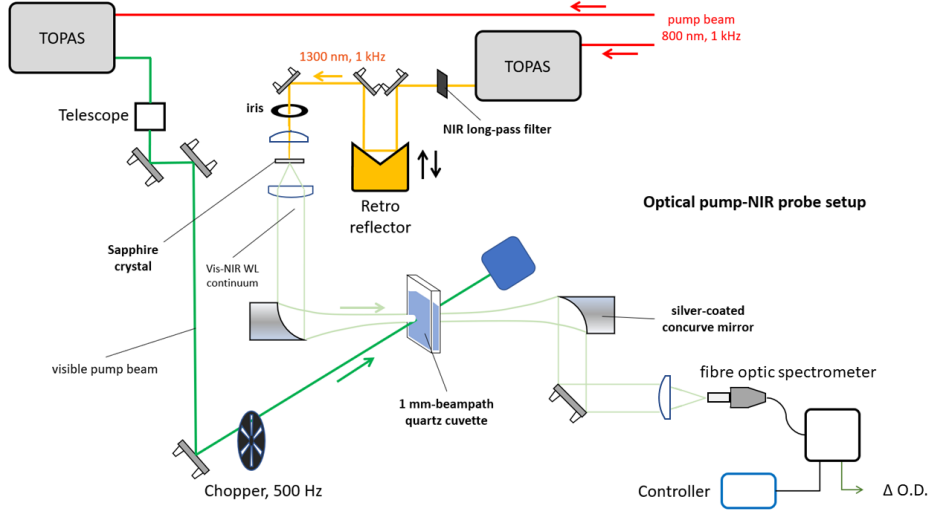
Figure 3.6: Schematic of the ultrafast pump-probe spectroscopy setup.

respectively. A set of neutral-density filters and narrow band-pass filters were placed in the beam path to avoid saturation of the detector (taking a maximum of 16,000 counts per scan) while affording a broadband white light supercontinuum. The obtained transient signals are averaged differential absorbance over multiple spectral scans:

$$\Delta OD(t) = OD_{on}(t) - OD_{off}(t) = \log_{10}\left(\frac{I_{on}}{I_{off}}\right) \tag{3.4}$$

where I_{on} and I_{off} are the intensities of transmitted white light beam under and without photoexcitation. To compare the dynamics of various transient features more straightforwardly, the transient absorption signals are normalized to the highest signal strength measured right after photoexcitation (ΔOD_0), obtaining:

$$\Delta OD_{norm}(t) = OD(t)/\Delta OD_0 \tag{3.5}$$

A schematic of the pump-probe setup used to probe the signals in the NIR region (720-1100 nm) is shown in **Figure 3.6**.

The IR pulse width was 40 fs, which defined the resolution of the experiment. The solution-state SWCNTs were transferred into a 1 mm beam path quartz cuvette for the measurement, which induced a power loss of ∼5 %. To carry out measurements under both resonant and non-resonant conditions, pump wavelengths

32

of 350 nm, 500 nm, 590 nm and 625 nm were chosen for the semiconducting SWCNT samples. The pump fluences were set to a wide range (0.1-20 mJ cm^{-2} per pulse) in order for a deep understanding of the optical pathways in SWCNTs at both the linear and non-linear conditions. The acquired TA signals were chirp-corrected and those detected at negative time delays were subtracted to remove the effect of pump scattering.

Experimental TA dynamics can be modelled based on the exciton decay rate equation and a excitation profile. The rate equation applied here is in a bi-exciton Auger recombination type in order to describe the large non-linear property of SWCNTs. Details of rate equation are given in the following chapters.

The profile of excitation beam can be considered as a Gaussian function with a duration on the scale of the pump pulse ($\sim$40-100 fs), which can be expressed as:

$$f(t) = 2\frac{\sqrt{\log 2}}{\sqrt{\pi}w} \cdot \exp(-4\log 2(\frac{t}{w})^2) \tag{3.6}$$

with w the duration of the profile.

3.5.2 Optical-pump/terahertz-probe (OPTP) spectroscopy

The dynamics of photoexcited charge carriers can be examined based on a relative change in the THz electric field after photoexcitation. In practice, this type of transient features can be characterized by OPTP spectroscopy [116; 117]. The experimental setup and characterizing methods are detailed in the following. The 1 kHz, 800 nm fs laser output from the same Ti:sapphire laser used for TA measurements was split into a pump and a probe beam. The pump beam was incident on a spintronic emitter to generate THz radiation [119]. The probe beam was used to gate the detector. The THz radiation was detected via electro-optic sampling in a ZnTe crystal. Compared to the THz-TDS system, OPTP employs an additional optical pump beam derived from an optical parametric amplifier (TOPAS) to photoexcite the sample. An extra mechanical delay stage was applied to change the time delay of this optical pump relative to that of the THz pulse. A high-precision, high-resolution oscilloscope (Pico Technology PicoScope 4262) was applied to record the balanced photodiode outputs for gate pulses (the 800 nm probe pulses mentioned above). To allow the electric field strength of the THz beam transmitted through the tested sample under the photoexcited condition (E_{on}) and the one without optical pump irradiation (E_{off}) to be measured, the beam used to pump the THz emitter and the optical pump beam were mechanically chopped at 500 and 250 Hz,

respectively. This scheme results in four types of signals, which are signal A (optical pump pulse on, THz pulse on), signal B (optical pump pulse on, THz pulse off), signal C (optical pump pulse off, THz pulse on) and signal D (optical pump pulse off, THz pulse off), and we can then have $E_{on} \propto (A - B)$ and $E_{off} \propto (C - D)$. A change in the THz transmission, $\Delta T/T_{off}$, at the sample due to photoexcitation is thus given as:

$$\Delta T/T_{off} = \Delta E/E_{off} = (E_{on} - E_{off})/E_{off} = \frac{(A - B) - (C - D)}{C - D} \qquad (3.7)$$

Negative transient signals ($\Delta E/E < 0$) are induced by the increased absorbance of THz beam due to the generation of photo-excited charge carriers, while positive transient signals ($\Delta E/E > 0$ are induced by the decreased absorption of THz beam due to following reasons: (i) the photo-excited excitons can form trions by taking the electrons or holes from doping. Trions have a higher mass and a lower conductivity, leading to decreased THz absorbance [116]; (ii) enhanced intertube interaction due to the existence of both metallic and semiconducting carbon nanotubes within a bundle.

The tested samples for OPTP characterizations in this thesis are SWCNT thin films lying on the quartz substrate which have a typical thickness of $\sim 100 nm$. With thin film approximation, the complex conductivity $\Delta\sigma(\omega) = \frac{\delta \Delta T}{T_{off}} \frac{n_i + n_k}{Z_0}$, where δ is the film thickness, $Z_0 = 377 \ \Omega$ is impedance of free space, n_i and n_k are, respectively, refractive indices of the medium before and after the sample.

3.6   Raman spectroscopy

Raman scattering is an inelastic light scattering event, during which both the direction and frequency of the photon will change [120]. It consists of following steps: (i) an electron is excited from the valence energy band to the conduction energy band after absorbing light; (ii) the electron scatters by emitting (or absorbing) a phonon and (iii) the electron relaxes back onto the valence energy band and emits a photon. Raman spectroscopy measures the intensity of emitted light as a function of frequency shift of the scattered photons, enabling the phonon frequencies and phonon dispersion relations of the material to be accurately determined. Depending on whether emitting or absorbing a phonon, Raman scattering can be classified as a Stokes process or an anti-Stokes process, respectively.

The number of emitted phonons before the relaxation of the lattice can be

one, two, and so on. We call them one-phonon, two-phonon and multi-phonon Raman processes, respectively. The order of a scattering event is defined as its number in the sequence of the total scattering events, including elastic scattering by an imperfection (*e.g.* a defect or edge) of the crystal. In order for an electron to recombine with a hole, the scattered $\mathbf{k} + \mathbf{q}$ states ($\mathbf{k}$ and $\mathbf{q}$ are the electron and phonon vectors, respectively) should not differ from $\mathbf{k}$ by more than two times the photon wave vector. This momentum conservation requirement and the small wave vector of the photon is the reason why we usually observe zone-center $\mathbf{q} = \mathbf{0}$ or Γ point phonon modes in a solid. For SWCNTs, the low-frequency radial breathing mode (RBM) and high-frequency G mode are two typical first-order Raman modes. RBMs are a unique phonon mode that are prominent in SWCNTs. It is a bond-stretching out-of-plane mode for which all carbon atoms move coherently along the radial direction. Since the mass of all carbon atoms along the circumferential direction is proportional to the SWCNT diameter, the frequency of RBM depends inversely on the nanotube diameter [120]. The intensity of first-order Raman scattering process can be expressed as [120]:

$$
I(\omega, E_L) = C(\frac{E_a}{E_j})[n(q,\mu) + 1] \sum_j |\sum_a \frac{M^d(\mathbf{k} - \mathbf{q}, jb)M^{ep}(\mathbf{q}, ba)M^d(\mathbf{k}, aj)}{\Delta E_{aj}(\Delta E_{aj} - \hbar\omega)}|^2 \quad (3.8)
$$

where ω is frequency, E_L is the energy of incident laser, C is a constant independent of nanotube chirality, $n(q,\mu)$ stands for the number of phonons, $M^d(k, aj)$ is a matrix element associated with the electric dipole interaction with the incident photon to make a transition from state a to state j, and $M^e p(q, ba)$ is a matrix element linked to the electron-phonon interaction, $M^d(k, aj)$ is a matrix element linked to the electric dipole interaction that gives emission of a photon with the transition from state j to state b. ΔE_{aj} is the energy difference between the starting state a and the final state j. $\hbar\omega$ is the phonon energy.

When the optical absorption (or emission) is to (or from) a real electronic state, the energy denominators in the oscillator strength becomes singular. There are thus two resonance conditions for optical transitions: (1) resonance with the incident laser photon, $E_L = \Delta E$ and (2) resonance with the scattered photon, $E_L = \Delta E + \hbar\omega$, with ΔE the energy difference between two electronic states. As well as to the resonant enhancement, a singularity in the joint density of states (JDOS) contributes to the Raman intensity. If energy of either the incident or the emitted photon matches that of the van Hove Singularities, strong Raman scattering can be detected. The polarization geometry can also affect the Raman intensity [121].

Such a change has a dependence on the symmetry of the phonon mode of interest.

In this study, Raman measurements were carried out on various instruments, including Renishaw InVia Reflex, Horiba T64000 triple stage and Horiba LabRam HR Evolution. The LabRam spectrometer was equipped with a laser excitation of 600 nm or 488 nm, with both lasers providing maximum optical power of 50 mW at the sample, and a 600 l/mm grating. The inVia systems were equipped with 325 nm (0.5 mW), 442 nm (25 mW), 514.5 nm (38 mW), 532 nm (20 mW), 633 nm (10 mW) and 785 nm (30 mW) with maximum powers at the sample as indicated. All data on the Invia system were collected by a 1800 l/mm grating except for the 325 nm and 442 nm excitation, which used a 2400 l/mm grating and 785 nm using a 1200 l/mm. The HORIBA T64000 instrument applied a triple-grating system to generate a 562 nm excitation beam.

To get the desired S/N ratio while avoiding heating or damaging the sample, the laser power was generally reduced to 1 to 5% of its maximum. The laser beams in visible wavelengths (>442 nm) were brought to a micron-scale spot focus (<5 microns) onto the sample by a ×50 objective lens, with N.A. 0.9, while the 325 nm beam was focused by a ×40 UV-enhanced objective lens. Spectra were collected in the back-scattering configuration. Temperature-dependent Raman measurements were conducted on the Linkam stage (THMS600) with a ramping rate of 40°C. The excitation beam power for these temperature-dependent measurements was increased by few times to compensate for the power loss at the quartz window on the stage. A spectrum was acquired 2 min after the temperature reached the set value. The issue of sample moving and defocusing during heating can be neglected as the Raman spectra were normalized to their background signal intensities afterward.

3.7 X-ray photoelectron spectroscopy (XPS)

XPS is a technique applied to analyze the composition of elements and chemical bonds. It detects kinetic energies of photoelectrons generated by the incident X-ray and obtains a plot of the number of electrons varying against binding energies, which are calculated by:

$$E_{binding} = E_{photon} - E_{kinetic} - \phi \tag{3.9}$$

where $E_{binding}$, E_{photon} and $E_{kinetic}$ are electron binding energy, X-ray photon energy and kinetic energy of emitted electrons, respectively. The work function ϕ is a

correction factor for the instrument and correlates to the minimum energy required to eject an electron from an atom.

Each element in the material will produce a number of peaks that present at binding energies corresponding to the energy levels of atoms (*e.g.*, $1s, 2s, 2p, 3s$). The peak intensity, or electron counts, would thus indicate the amount of an element within the XPS sampling volumn. Since XPS only detects the fraction of electrons which escape from the sample, it is a type of surface-sensitive characterizing technique.

To carry out XPS measurements on the vacuum-filtered SWCNT thin films, they were attached to electrically-conductive carbon tape and mounted on to a sample bar, before being loaded into a Kratos Axis Ultra DLD spectrometer. The load lock was pumped to below 1×10^{-6} mbar before sample transfer to the analysis chamber. After sample transfer, the analysis chamber had a base pressure below 1×10^{-10} mbar. XPS was performed with the sample illuminated using a monochromated Al $K\alpha$ x-ray source ($h\nu = 1486.7$ eV).

XPS measurements were performed in the main analysis chamber, with the sample being illuminated using a monochromated Al Kα x-ray source ($\hbar\nu = 1486.7$ eV). The measurements were conducted at room temperature and at a take-off angle of 90° with respect to the surface parallel. The core level spectra were recorded using a pass energy of 20 eV (with a resolution of approximately 0.4 eV), from an analysis area of 300 mm × 700 mm . The work function and binding energy scale of the spectrometer were calibrated using the Fermi edge and 3d5/2 peak recorded from a polycrystalline Ag sample prior to the commencement of the experiments. The data were analysed in the CasaXPS package using Shirley backgrounds and mixed Gaussian-Lorentzian (Voigt) lineshapes, with asymmetry parameters where appropriate. Due to surface charging during the experiment, the samples had to be flooded with a beam of low energy electrons in order to prevent the surface becoming positively charged. This necessitated subsequent referencing of the binding energy scale to the C-C/C-H adventitious carbon component at 284.6 eV. For compositional analysis, the analyser transmission function was determined using clean metallic foils to determine the detection efficiency across the full binding energy range.

3.8   Summary

Knowing the atomic structures and dimensionalities of nanowire-filled SWCNT is essential to the subsequent optical and spectroscopic research. Based on various kinds of transmission electron microscopic techniques (conventional TEM, ADF-

STEM, electron diffraction, etc.), the atomic structures of filled nanotubes as well as their degrees of bundling can be revealed. Additional structure parameters such as the nanotube bundle size are going to be characterized by AFM and SEM. These measurements will pave the way for an in-depth understanding on the distinct effects of nanowire-nanotube, intra-nanotube and inter-nanotube interactions on the electronic properties of SWCNTs.

Various steady-state and time-resolved spectroscopic characterizations will be conducted to study the optical features of SWCNT materials, especially their excitonic properties. In essence, the experiments carried out in this work aim to disclose the relation between atomic structures of filled SWCNTs and their physio-chemical properties. The following chapters will provide details about the spectroscopic studies on various types of SWCNTs whose diameters are refined based on the chemical methods.

Chapter 4

Materials Synthesis and Purification

In this chapter we provided details of methods for nanotube filling and refinement. Determination of the material structures and nanotube chiralities were carried out based on TEM, AFM and steady-state absorption measurement.

4.1   Materials

SWCNTs used in this study include products from CoMoCAT (ref no. 775533, Co-MoCAT76, $\bar{d}_t$ 0.84 nm; ref no. 773735, SG65i, $\bar{d}_t$ 0.78 nm; ref no. 724777, CHASM, d_t 0.8-1.4 nm), HiPco (d_t 0.8-1.2 nm) and TUBALL ($\bar{d}_t$ 1.6 nm). Sodium dodecyl sulfate (SDS, ACS reagent, $\geq 99.0\%$, Sigma-Aldrich) was used as surfactant to isolate the carbon nanotubes. Mercury telluride (HgTe, 99%, Alfa Aesar) was used as the filling material. Hydrogels made from a cross-linked copolymer of allyldextran and N,N'-methylene bisacrylamide (Sephacryl S-200, GE Healthcare) were applied for the gel column chromotography experiment. Polyethylene-glycol (PEG, Sigma-Aldrich, MW 8,000), dextran (DX, Sigma-Aldrich, MW $\sim 70,000$), sodium deoxy-cholate (DOC, Sigma-Aldrich, $\geq 98.0\%$) and sodium cholate (SC, Sigma-Aldrich, $\geq 99\%$) were used in the ATP extraction experiment. Gelatin (Sigma-Aldrich) was applied as the polymer matrix for preparing gelatin-embedded SWCNT films. The cellulose filter membrane used for preparation of filtrated SWCNT thin films were from Merck (0.05 µm).
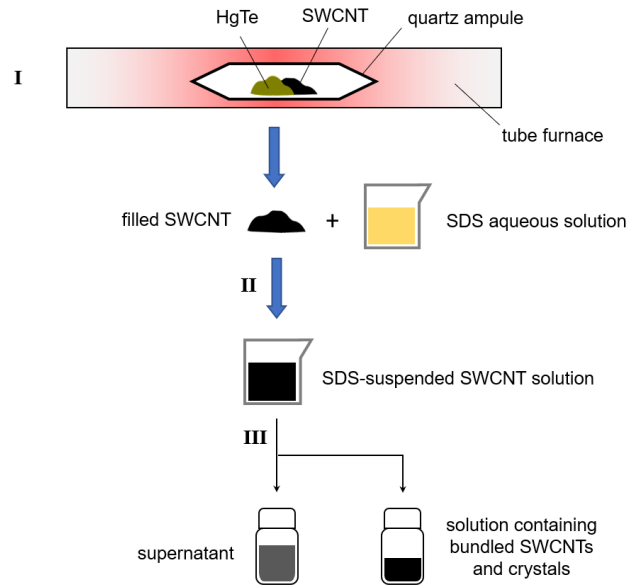
Figure 4.1: Schematic diagram describing steps of melt filling and SWCNT dispersing. Step I: conduct melt filling based on the mixture of SWCNT and HgTe powders at a temperature above the melting point of HgTe in a tube furnace. Step II: disperse the powder-like filled SWCNTs in SDS aqueous solution by tip-sonication. Step III: remove bundled SWCNTs and catalysis nanoparticles by centrifugation.

4.2 Filling nanotubes via melt filtration and sublimation

Melt filling synthesis was conducted at a temperature slightly above the melting point of the filling material to let them spontaneously infiltrate into the carbon nanotubes. Such a method had been previously demonstrated to result a high ratio of filling inside medium-size SWCNTs (1.35-1.5 nm in width) [73]. During the filling experiment, a mixture of raw SWCNT powders and filling material was put in a quartz ampule which was sealed under a high vacuum ($<1 \times 10^{-3}$ mbar). The ampule containing materials were then transferred into a tube furnace and heated to a temperature above the melting point. For filling with HgTe, the raw powder of SWCNTs was mixed with the ground HgTe powder to achieve a 1:1 mass ratio. The mixture was transferred in the ampule and heated to 770°C for 12 h followed by 670°C for 3 h. The synthesis experiment is descriptively shown by Step I in **Figure 4.1**. The resulting filled product contained impurities such as crystals grown outside of the SWCNTs (**Figure 4.2**).

Filling result of the experiments was examined by HRTEM and ADF-STEM imaging. It was particularly found that CoMoCAT76 (**Figure 4.3a**), CHASM
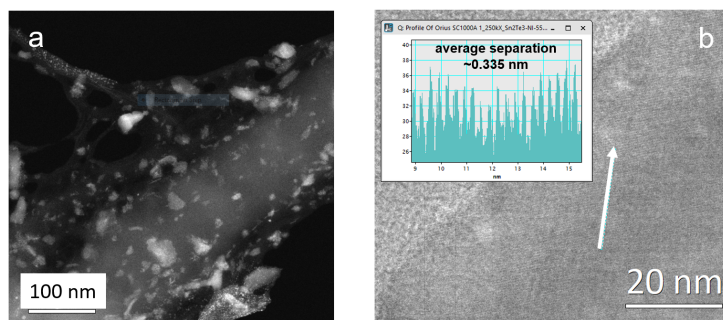
40

Figure 4.2: (a) ADF-STEM and (b) BF-TEM images showing crystals grown outside of the SWCNTs after the melt filling experiment. Inset in (b) is the intensity profile along the direction indicated by the red arrow. The averaged separation between two peaks matches up with the d-spacing of (111) plane for the HgTe crystal
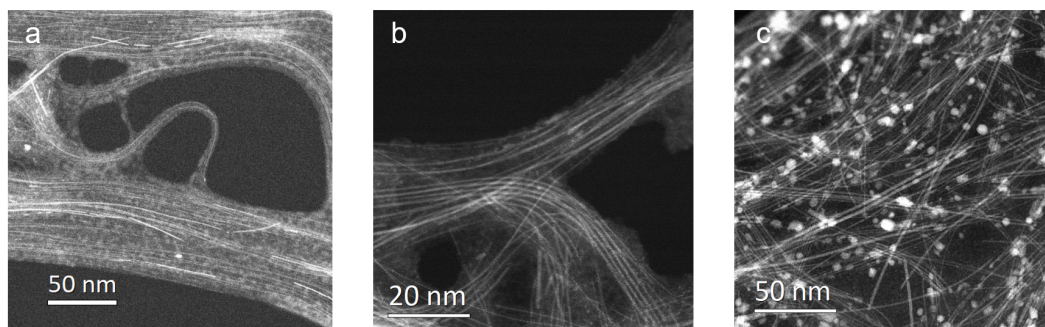
.

Figure 4.3: ADF-STEM images of the as-fabricated HgTe NW-filled
(a) CoMoCAT76, (b) CHASM and (c) TUBALL SWCNTs.

(**Figure 4.3b**) and TUBALL (**Figure 4.3c**) SWCNTs can afford a relatively high filling ratio, while SWCNTs from SG65i (**Figure 4.4a**) and HiPco (**Figure 4.4b**) were only partially filled.

4.3 Chirality refinement based on gel column chromatography

The unfilled and HgTe-filled powder-like SWCNTs were added to an aqueous SDS medium (2 wt. %) and then dispersed by a tip sonicator (150 W, 20 % power output) operated under a pulsed mode (2s power on and 2s power off) for at least 15 h (described by Step II in **Figure 4.1**). The obtained SWCNT dispersion was then pre-purified by an ultracentrifuge (Thermo Scientific Sorvall WX+), described by Step III in **Figure 4.1**. It was revealed that an acceleration of 197,000$\times g$ was
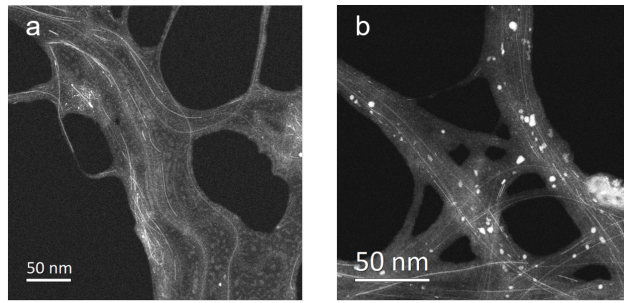
Figure 4.4: ADF-STEM images of the as-fabricated HgTe NW-filled (a) SG65i and (b) HiPco SWCNTs.
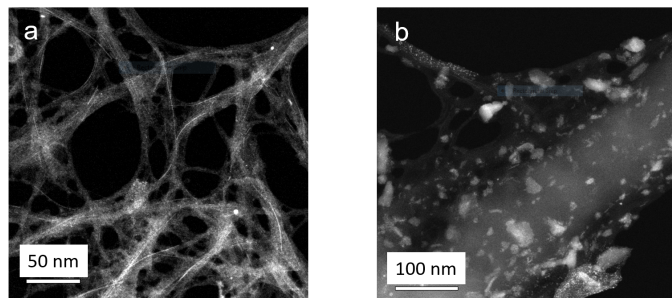

Figure 4.5: ADF-STEM images of HgTe NW-filled CoMoCAT76 SWCNTs treated by centrifugation under centripetal accelerations of (a) 197,000×g and (b) 5,000×g. (b) is same as Figure 4.2a

sufficient to remove most impurities such as overgrown crystals (**Figure 4.5**).

The as-centrifuged SWCNT solutions were sorted based on a gel column chromotography approach similar to the one reported by a previous work [61]. In brief, alkyl dextran-based gels were loaded into a glass column and equilibrated by a 2 wt. % SDS solution. SWCNT solution of about twice the volume of the gel bed was then applied to the column. After the SWCNT solution passed through the gel bed and a fraction of nanotubes were trapped, aqueous solutions containing increasing amounts of SDS (*e.g.*, 0.3 wt.%, 0.5 wt.%, 1.0 wt.%, 1.5 wt.%, 2.0 wt.%, 5.0 wt.%) were used to elute the nanotubes. It has been found that the fraction of semiconducting nanotubes that have the smallest diameters (*e.g.*, (6,4) and (6,5)) can be collected first. To sort nanotubes with greater diameters, pure DI water was added to the solution of SWCNTs that were not bound to the gels (to decrease the surfactant concentration to a certain value, such as 1.6 wt. % or 1.2 wt. %) and another round of gel chromatography experiment was then conducted. To extract metallic nanotubes from the CoMoCAT76 SWCNTs, the as-centrifuged SWCNT
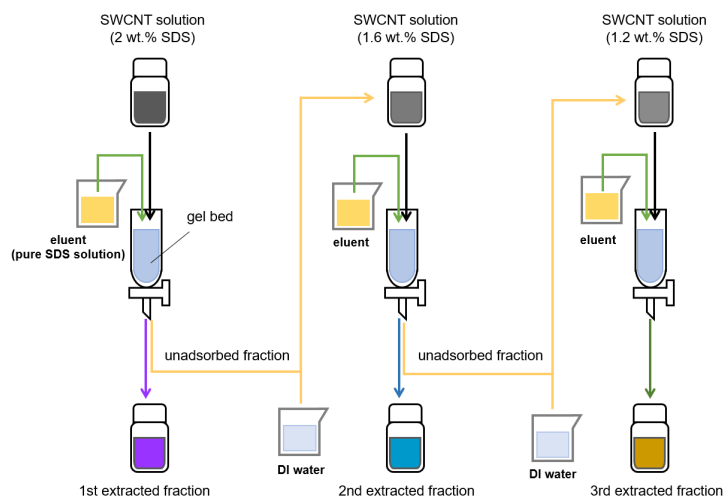
Figure 4.6: Schematic diagram describing the steps of SWCNT chirality refinement by three rounds of gel column chromatography experiment, which enable nanotubes with increased diameters to be extracted.

solution was applied to the gel column and the first solution portion coming out from it (showing a light brown color) was collected, which had an enrichment of metallic SWCNTs. The multi-step gel column chromatography experiment applied to extract SWCNTs with increased diameters is descriptively shown in **Figure 4.6**.

During the sorting experiment, it was discovered that eluent with a minimum SDS concentration of 5 wt. % was required to achieve the enrichment of nearly isolated semiconducting SWCNTs (no significant red-shifting of the excitonic absorption peak caused by bundling, as is shown in **Figure 4.7**). We particularly found that such a separation protocol can realize an efficient diameter refinement for the HiPco SWCNTs, with discrete excitonic peaks clearly been observed from the absorption and PL spectra after the sorting (**Figure 4.8** and **Figure 4.9**).

The structures and dimensionalities of sorted SWCNTs were studied by AFM imaging. The actual diameter of the SWCNT (or SWCNT bundle) was judged based on the averaged height at 5 different sites along the tube axis direction. It was revealed that the CoMoCAT76 and HiPco SWCNTs can be effectively isolated down to an individual state (**Figure 4.10**), while the SG65i and CHASM SWCNTs existed in a bundled state with a width of tens of nm (**Figure 4.11**). The exceptionally low yield of isolated nanotubes from the SG65i and CHASM SWCNT products is in contrast with the experimental results reported in previous studies [122; 57]. Possible interpretation of the difficulty to debundle these two types of SWCNTs is an inefficient non-covalent interaction between the surfactant molecules and nanotubes
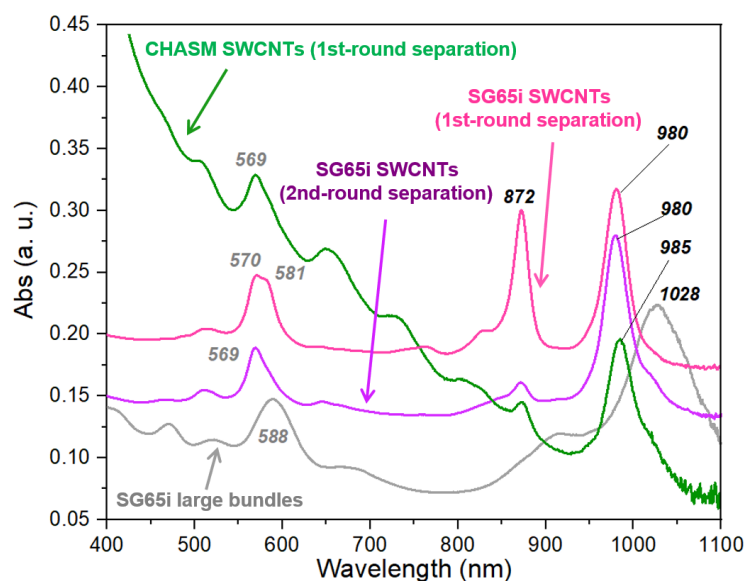
Figure 4.7: UV-vis-NIR absorption spectra of the SG65i and CHASM SWCNTs extracted from the raw product by gel column chromatography under different experimental conditions. Wavelengths of the absorption peaks associated with S_{11} and S_{22} excitonic transitions of SWCNTs are annotated. Pink and purple curves stand for the spectra of SG65i SWCNTs extracted by the 5 wt. % SDS eluent during the 1st and 2nd round of gel column chromatography experiment, respectively. Grey curve stands for the spectrum of heavily bundled SG65i SWCNTs extracted by the 2 wt. % SDS eluent during the 1st-round of gel column chromatography experiment. Green curve stands for the spectrum of CHASM SWCNTs extracted by the 5 wt. % SDS eluent during the 1st-round of gel column chromatography experiment.

Figure 4.8: Photoluminescence-excitation (PLE) maps of (a) (6,5)-, (b) (7,5)- and (c) (7,6)-enriched SWCNTs extracted from HiPco product.
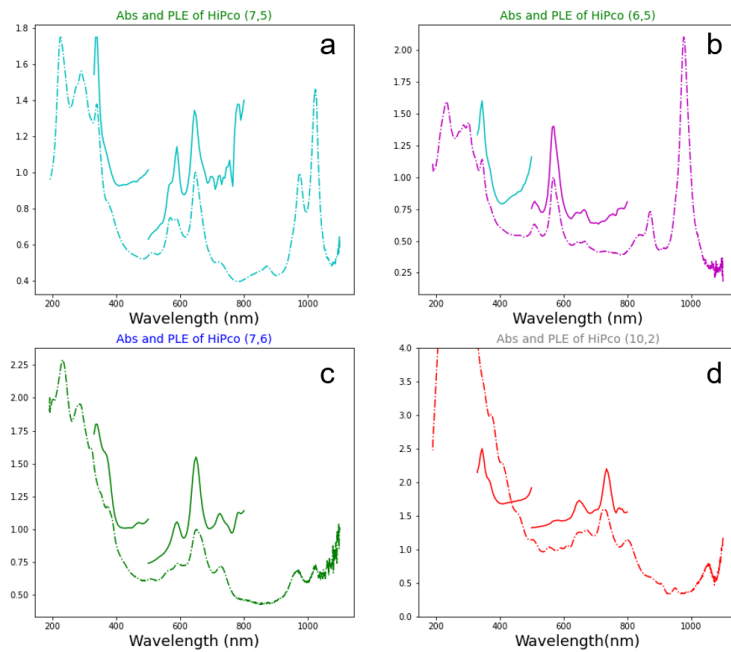
Figure 4.9: Comparison between the absorption spectra (dashed dot curves) and PLE profile (solid curves) of different HiPco SWCNT fractions.

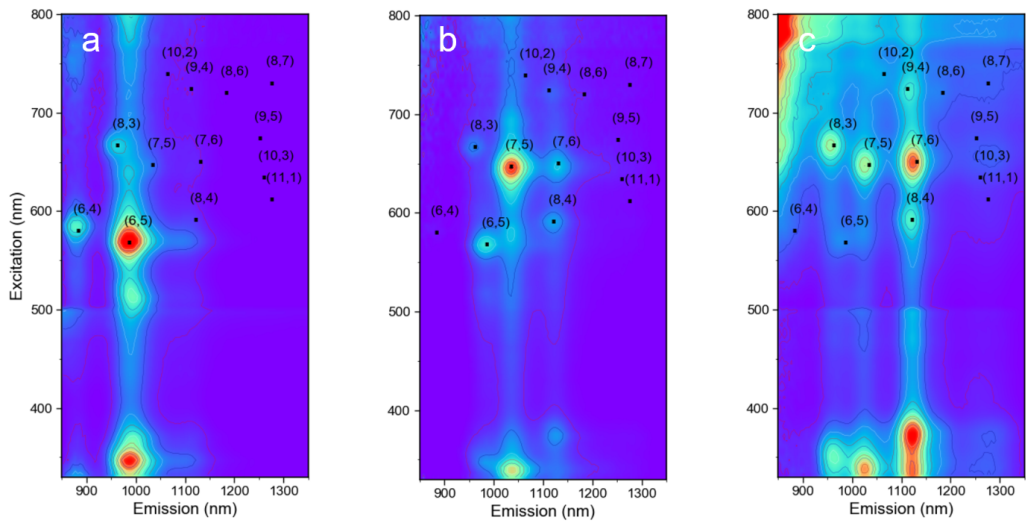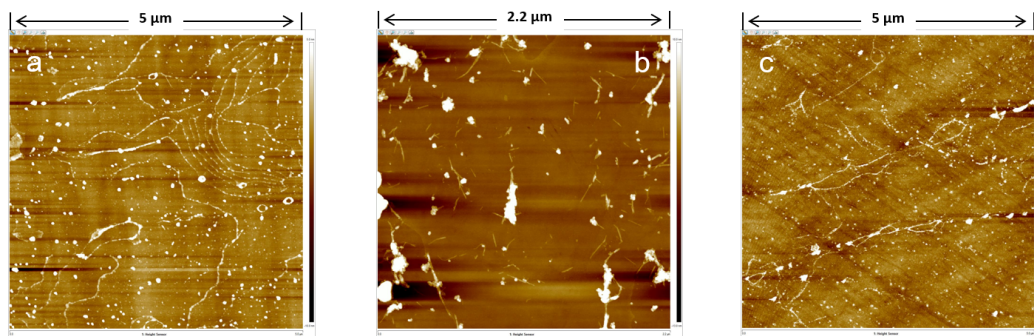Figure 4.10: AFM height images of sorted (a) semiconducting CoMoCAT76 SWC-NTs, (b) metallic CoMoCAT76 SWCNTs and (c) (7,5)-enriched HiPco SWCNTs.
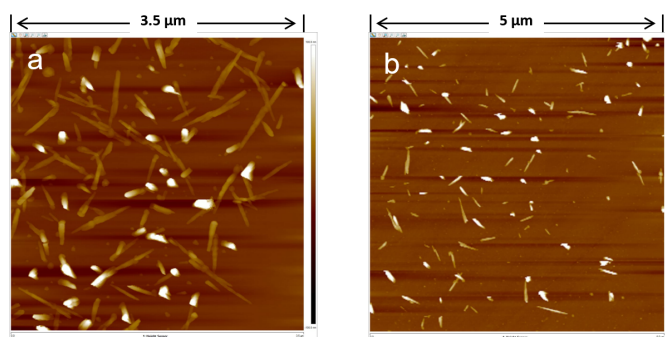
Figure 4.11: AFM height images of sorted (a) (6,4) and (6,5)-enriched SG65i SWC-NTs and (b) (7,5)-enriched CHASM SWCNTs.

[123].

4.4 SWCNT sorting based on aqueous two-phase extraction

The large-diameter TUBALL SWCNTs were sorted based on an aqueous two-phase extraction (ATP) method [58]. In brief, 50 wt. % PEG and 20 wt. % Dxtran aqueous solutions were mechanically mixed together by a Vortex mixer (VWR) to prepare a two-phase medium. A clear phase separation can be observed over time. SWCNT stock solution (as-centrifuged SWCNTs dispersed in the SDS medium), 5 wt. % SDS, 5 wt. % SC, 5 wt. % DOC aqueous solutions and pure DI water were then added into the two-phase medium, with their volumes being adjusted to achieve a constant final sum value. The mixed solution was agitated again by the Vortex mixer and centrifuged to allow the redistribution of SWCNTs in the two phases.
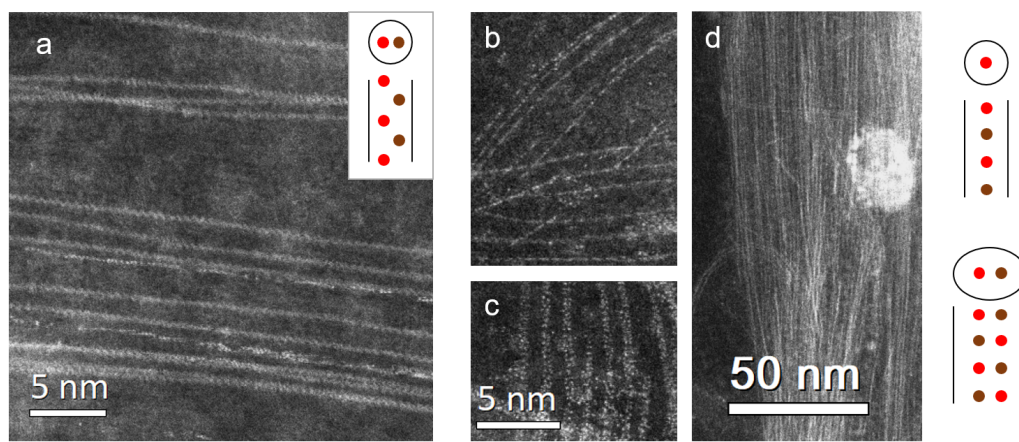
Figure 4.12: ADF-STEM images of filled SWCNTs with different NW structures: (a) Semiconducting CoMoCAT76 SWCNTs extracted from the as-centrifuged SWCNTs after five rounds of gel column chromatography experiment displaying a dominant NW structure of zig-zag chain, (b,c) As-centrifuged CHASM SWCNTs which display two main types of NW structures: linear chain and 2 atom-by-1 atom-thick chain, (d) CHASM SWCNTs extracted from the as-centrifuged SWCNTs after the first round of gel column chromatography experiment showing a dominance of linear chain structure. The atomic structures of zig-zag, linear and two atom-by-one atom-thick (2×1) chains are schematically shown by the inset of panel (a) and two diagrams on the right, respectively.

4.5 Structure and chemical composition of nanowires in chirality-refined SWCNTs

The nanostructure of enriched SWCNTs was examined by HRTEM and ADF-STEM. It was discovered that the separation of SWCNTs by diameters after the gel column chromatography or ATP experiment can also lead to the refinement of nanowire structure.

By extracting small-diameter filled nanotubes ($d_t < 1$ nm, chiralities of these CoMoCAT76 SWCNTs were determined based on optical absorption and photoluminescence characterizations, details of which are provided in **Section 5.2**) from the raw (as-centrifuged) CoMoCAT76 SWCNTs, a dominant NW structure of zig-zag chains can be observed (**Figure 4.12a**).

Linear and 2 atom-by-1 atom-thick chains were found to be the two main NW structure in the CHASM SWCNT sample (**Figure 4.12b**, **c**). After a subsequent diameter enrichment by gel column chromatography, small-diameter SWCNTs with NWs dominated by a linear chain structure can be extracted (**Figure 4.12d**, chiralities of these CHASM SWCNTs were determined based on optical absorption and photoluminescence characterizations, details of which are provided in **Section 6.2**).

As revealed by the theoretical study conducted by Vasylenko and colleagues [74], the formation energies of nanowires having different structures vary with the encapsulating nanotube diameter, resulting in a favorable nanowire structure for a particular SWCNT diameter range. Details of the calculation method and the obtained formation energies for nanowires with different atomic structures are provided in **Appendix B**. As per calculation results, it was suspected that the linear chains and zig-zag chains exist inside the small-diameter (n, m) species, such as (6,5) and (7,5), while the 2 atom-by-1 atom-thick chains presented inside (n, m) species with a diameters of generally greater than 0.9 nm.

For TUBALL SWCNTs, it was demonstrated that the ATP sorting can lead to an effective separation of filled nanotubes into the top liquid phase and unfilled SWCNTs or extraneous materials (crystals grown outside of SWCNTs) into the bottom liquid phase (**Figure 4.13**).

EDX analyses were performed to examine the chemical composition of materials. It was demonstrated that both the zig-zag chains grown inside CoMoCAT SWCNTs and wider chains grown inside TUBALL SWCNTs had the stoichiometry HgTe (**Figure 4.14** and **4.15**). For the filled CHASM SWCNTs, a variation in the chemical composition of nanowires with the state of purification was found (**Figure 4.16**). Compared to as-centrifuged samples, the SWCNTs further purified based
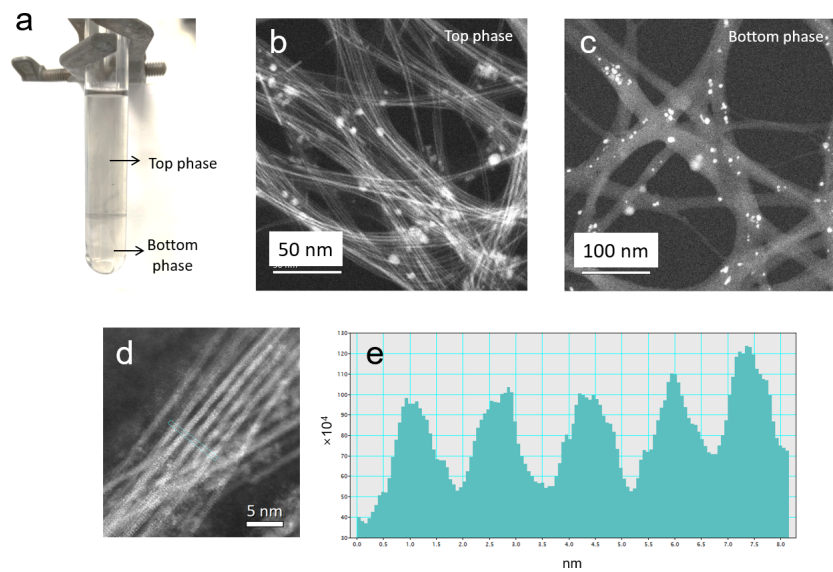
Figure 4.13: (a) Real photograph showing the re-distribution of TUBALL SWCNTs in two phases after the ATP extraction experiment. (b,c) ADF-STEM images of extracted filled TUBALL SWCNTs from the top and bottom liquid phases. (d) A higher-resolution image of filled TUBALL SWCNTs from the top phase and (e) corresponding intensity profile. NWs in TUBALL SWCNTs were found to be comparatively wider.
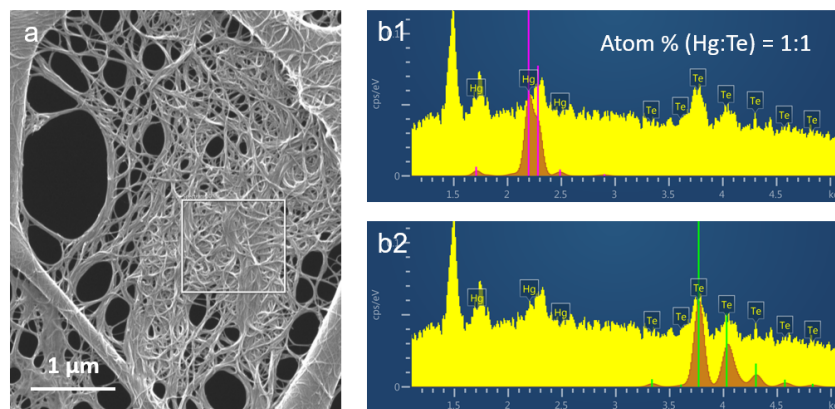
Figure 4.14: EDX analysis on the HgTe-filled semiconducting CoMoCAT SWCNT sample. (a) The morphology of SWCNT film in the scanned region. The white rectangle highlights the area selected for EDX detection. (b) The experimental (yellow spectral region) and simulated (red spectral regions) EDX signal peaks.

on gel column chromatography had a higher Te abundance (atom ratio of Te:Hg is $\sim 70\% : 30\%$). This probably indicates that the linear nanowires contain crystal regions of pure tellurium depleted in mercury.

4.6 Preparation of densely-packed SWCNT thin films

To examine the optical properties of material by FTIR and terahertz spectroscopy, thin films of densely packed SWCNTs were prepared based on the vacuum filtration method. A schematic diagram depicting the filtration setup and the preparation steps of SWCNT thin films is shown in **Figure 4.17**.

The topography of the SWCNT thin films were studied by AFM (**Figure 4.18**). It can be found that the nanotubes in these films presented a higher degree of bundling compared to those in the solution state (see AFM images in **Figure 4.10** and **Figure 4.11**). The homogeneity of the films were investigated by the quantum nanomechanical (QNM) tool of AFM. It allows additional signals reflecting the mechanical properties of materials to be recorded and analyzed during the AFM measurement, including modulus, adhesion, dissipation, and deformation. For filled SWCNTs, nanoparticles that were grown outside of SWCNTs (extraneous materials) were occasionally encountered over the film surface, which typically displayed a lower adhesion force than nanotubes, as can be seen from the adhesion force maps (**Figure 4.19c,d**). As determined by previous studies, the emergence of overgrown crystals can significantly alter the optical properties of SWCNTs [117]. While these
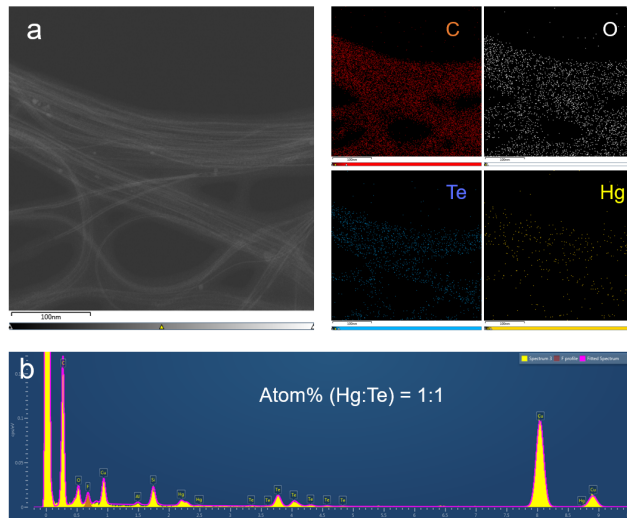
Figure 4.15: EDX analysis on the HgTe-filled TUBALL SWCNT sample. (a) ADF-STEM image showing the characterized region, with the EDX maps for C Kα1, Oα1, Te Lα1 and Hg Lα1 peak signals shown on the right. (b) EDX spectrum obtained from the same region.
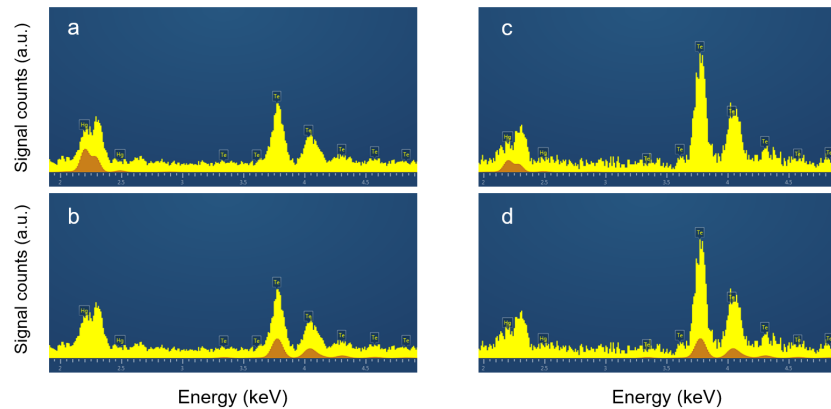
Figure 4.16: EDX analysis on the HgTe-filled CHASM SWCNT samples. (a,b) are as-centrifuged SWCNTs showing a dominant NW structure of both linear chain and 2 atom-by-1 atom-thick chain. (c,d) are SWCNTs obtained after the first round of gel column chromatography experiment, which show a dominant NW structure of linear chain.
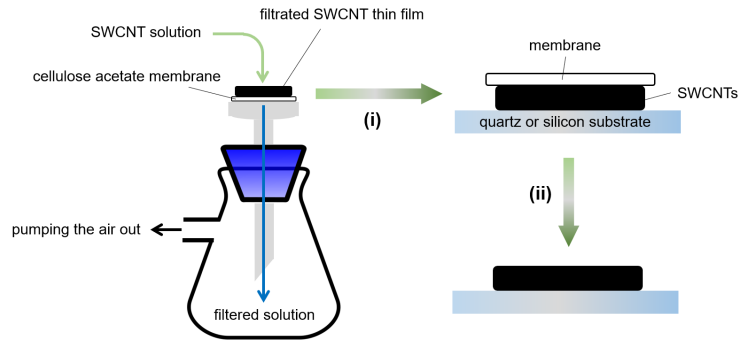
Figure 4.17: The vacuum filtration setup and the steps to prepare SWCNT thin films. The as-filtrated thin film is attached onto the quartz or silicon substrate (Step (i)). The cellulose acetate membrane is then removed by the vapor of acetone (Step (ii)).

extraneous materials can be eliminated by a post-annealing treatment under vacuum [124], it may also remove the free carriers in SWCNTs and hence change their optical property in the far-infrared region [115]. Therefore, no post treatment was conducted on the SWCNT films prior to optical characterizations.

4.7 Summaries

In this chapter, the results of nanowire filling inside various types of SWCNT products are shown. It is demonstrated that a higher yield of encapsulated nanowires can be achieved in CoMoCAT76, CHASM and TUBALL SWCNTs than in SG65i and HiPco SWCNTs. Based on gel column chromatography, diameter refinement was achieved on CoMoCAT76, CHASM and HiPco SWCNTs. Such a nanotube diameter selection further resulted in an enrichment of nanowires with a dominant structure type. Optical characterizations and investigations of the electronic properties on these diameter- and chirality-separated SWCNTs will be carried out in **Chapter 5, 6** and **7**.
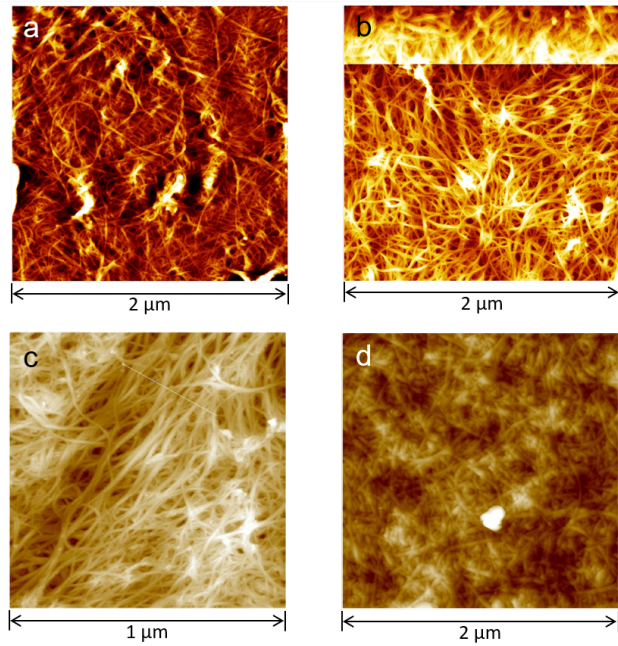
Figure 4.18: AFM height images of (a) (6,4), (6,5)-enriched SG65i, (b) (7,5)-enriched CHASM, (c) semiconducting CoMoCAT76 and (d) metallic CoMoCAT76 SWCNT films.
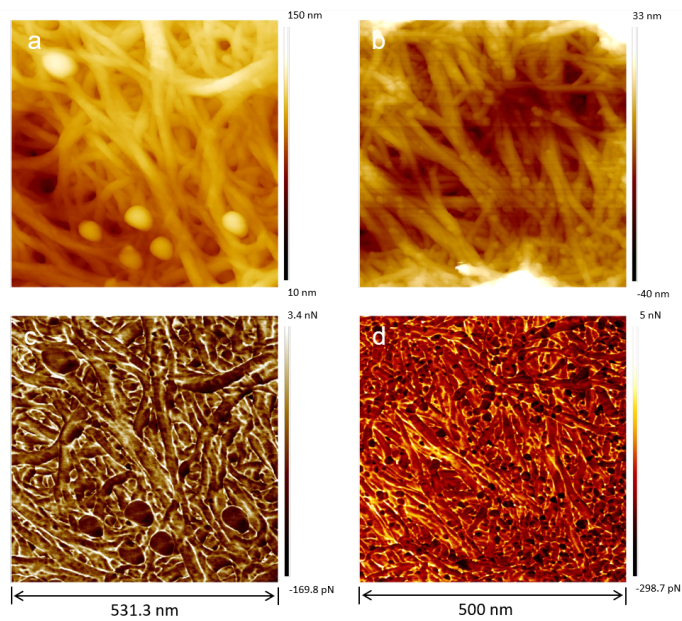
Figure 4.19: AFM height images (a,b) and adhesion force maps acquired during the QNM measurments (c,d) of (a,c) HgTe-filled SG65i and (b,d) HiPco SWCNT films.

Chapter 5

Optical Properties of Zig-zag HgTe Nanowire-filled SWCNTs

In this chapter we studied the optical properties of chirality-refined SWCNTs filled by zig-zag atomic NWs. **Section 5.2-5.5** appear in the following publication: Ziyi Hu, Ben Breeze, Reza J. Kashtiban, Jeremy Sloan, and James Lloyd-Hughes Zigzag HgTe Nanowires Modify the Electron–Phonon Interaction in Chirality-Refined Single-Walled Carbon Nanotubes, *ACS Nano*, 2022, 16, 4, 6789-6800.

5.1 Background

5.1.1 Raman modes of SWCNTs

Based on the nature of Raman modes of SWCNTs, they can be divided into different categories, which include: i) phonon wave vector (q) of the phonon eigenfunctions which defines the symmetry of a Raman mode as A (totally symmetric) or E_μ (μ is the number of nodes and equals to 1, 2, 3,...). ii) Resonance type: one-phonon single resonance, two-phonon single resonance and two-phonon double resonance. iii) Intravalley or intervalley scattering: In a double resonance case, this depends on whether the scattering event takes an electron from K to K' point, or vice versa. iv) Stokes or anti-stokes Raman scattering: Whether the scattering of an electron is by a phonon consists of the emission of a phonon (Stokes shift) or the absorption of a phonon (anti-Stokes shift). According to the above categories, the properties of various Raman modes in SWCNTs can be learned, such as radial breathing mode (RBM), disorder mode (D) and tangential mode (G). The common Raman modes of SWCNTs and their features are shown in the table below:

Table 5.1: Typical Raman modes of SWCNTs and their discription

Name	Estimated frequency (cm^{-1})	Resonance type	Notes
RBM	237/d$_t$	SR	Vibration of radius
immediate-frequency mode (IFM$^-$)	750-850	DR2	Combination mode oTO–LA
immediate-frequency mode (IFM$^+$)	950-1050	DR2	Combination mode oTO-LA
D	1300-1400	DR1	LO or iTO mode, inter-valley scattering
G$^-$	1540-1580	SR	Split from the G mode of graphite due to the curvature effect of nanotube, not observable in armchair SWCNTs
G$^+$	1590-1600	SR	split from the G mode of graphite due to the curvature effect of nanotube
Breit–Wigner–Fano lineshape (BWF)	1550	SR	Only observed in non-armchair metallic SWCNTs
M$^-$	1732	DR2	overtone of oTO mode
M$^+$	1750	DR2	overtone of oTO mode
iTOLA	1950	DR2	combination mode of iTO and LA
G'	2700	DR2	overtone of D mode
2LO	2900	DR2	overtone of LO mode
2G	3180	DR2	overtone of G mode

SR–single resonance, DR1–first-order ($q \sim 0$) double resonance, DR2–second-order double resonance, oTO–out-of-plane transverse optic, iTO–in-plane transverse optic, LO–longitudinal optic, LA–longitudinal acoustic.

The Raman-active G band of SWCNTs contains multiple peaks as a result

of the curvature of the SWCNT, which yields different C-C vibrational frequencies for the axial and circumferential directions [125; 120]. The G mode of SWCNTs is commonly found to split into a G^- and G^+ component presenting at a relatively lower and higher frequency, due to the curvature effect of nanotubes. These two G mode components are known to be related with the optical transition processes coupled to the longitudinal optic (LO) and transverse optic (TO) phonons, respectively [125]. Due to the strong coupling of phonon to the electronic continuum, the G mode for metallic SWCNTs is characterized by a broadened lineshape with a significant spectral down-shifting (typically below 1600 cm^{-1}), which is known as the Breit-Wigner-Fano (BWF) profile and can be expressed as:

$$I(\omega) = I_0 \frac{[1 + (\omega - \omega_{BWF})/q\Gamma]^2}{1 + [(\omega - \omega_{BWF})/\Gamma]^2} \tag{5.1}$$

where the parameter q describes the coupling strength between the phonon and the electronic continuum, ω_{BWF} is the wavenumber of the maximum intensity I_0, and Γ describes the line broadening. Although the BWF lineshape is typical for metallic SWCNTs, it was only observed in non-armchair nanotubes. For armchair metallic SWCNTs, the G mode spectra is dominated by a G^+ peak at frequencies similar to that in semiconducting SWCNTs (1590-1600 cm^{-1}) while with the absence of the G^- peak.

5.1.2 Auger recombination in SWCNTs

Auger recombination is a non-radiative process occurs in a range of materials involving atoms, molecules, organic and inorganic semiconductors induced by multiparticle interaction [126; 127]. In bulk crystals, the Auger recombination is viewed as a three-particle interaction, where a conduction band electron and a valence band hole recombine, and the excess energy is transferred to a third particle (free electron or hole), which is reexcited to a higher-energy state [128]. The charge carriers involved are assumed to be noninteracting quasifree particles [129]. This non-radiative Auger recombination/relaxation path determines the carrier recombination dynamics at a high carrier density under intense photo-excitation and would depend on the spatial localization of carriers. The rate equation for recombination in bulk crystals is given as follows:

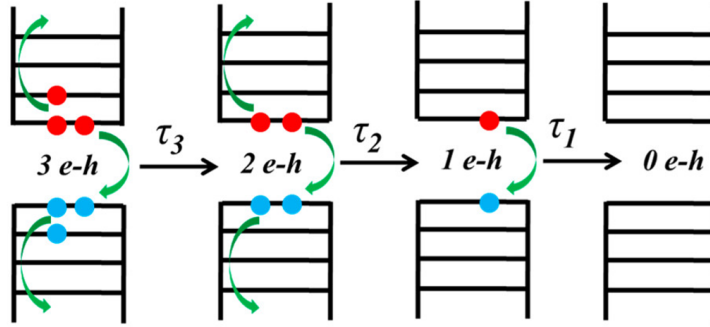$$\frac{dn(t)}{dt} = -An(t) - Bn^2(t) - Cn^3(t) \tag{5.2}$$

Figure 5.1: Schematic showing the sequential three e-h pairs, two e-h pairs and one e-h pair recombination processes in SWCNTs. Reproduced with permission from ref [132]. Copyright 2018 American Chemical Society.

Here $n(t)$ is the time-related density of carriers (electrons and holes). An represents recombination at interfaces and impurities. $Bn^2(t)$ represents the radiative band-to-band recombination, which determines the intensity of fluorescence. The third term $Cn^3(t)$ represents the nonradiative Auger recombination, whose rate is proportional to the third power of the carrier density. A, B and C are coefficients associated with these three processes.

As had been introduced in the previous chapters, tightly bound electron-hole pairs (excitons) are expected in the low-dimensional nanomaterials such as 1D nanowires and 2D quantum-well structures. A strong Coulomb interaction leads to the large exciton binding energy, while also resulting in rapid scattering involving multiple charge carriers. For 1D systems such as SWCNTs, the efficiency of multiple exciton generation and interaction between them would have a strong dependence on the electronic structure and thus the chirality of nanotubes [130; 131]. In addition, Kohn–Sham tight-binding density functional theory-(DFT-)based simulation also uncovered that the rate of Auger decay had a dependence on the aspect ratio of SWCNT due to coupling between the electronic states, with a slower recombination rate facilitated in a longer nanotube [132]. Due to the fact that Auger recombination is a non-radiative process, it can limit the quantum efficiency of light emission in SWCNTs [133; 134]. A schematic to describe the scattering processes leading to the two- and three-exciton Auger recombination in SWCNTs is shown in **Figure 5.1**.

Due to strong excitons in SWCNTs, the lowest-order Auger process involving Auger recombination is thus a two-exciton interaction, or bimolecular process, known as exciton-exciton annihilation (EEA). The process can be described as follows: one exciton is recombined to the ground state, a second exciton is promoted to a higher-energy excitonic state or dissociate into a free electron-hole pair

[135; 136; 137; 138]. The rate equation for SWCNTs is then given as follows:

$$\frac{dn(t)}{dt} = -kn(t) - \gamma n^2(t) \tag{5.3}$$

where $kn(t)$ and $\gamma n^2(t)$ stand for the monomolecular recombination and Auger bimolecular recombination, respectively. k and γ are the associated coefficients.

The Auger recombination rate coefficient γ is related to the Auger constant A by:

$$\gamma = \frac{A}{L} \cdot N(N-1) \approx A \cdot L \cdot n^2 \tag{5.4}$$

where N is the number of excitons and n is the line exciton density. Perturbation theory has been applied to calculate the Auger rate constant of SWCNTs [130]. Based on the calculation results, a strong link of Auger recombination rate with SWCNT exciton binding energy was revealed, which is expressed as:

$$A = 128\frac{\omega_{vc}}{k_{e0}} \times (\frac{\mu}{m_0})(\frac{E_b}{E_g})^3 \tag{5.5}$$

where ω_{vc} is the interband transition strength, k_{e0} the wave vector of electron at the eventual state, E_g the band gap energy and E_b the exciton binding energy, respectively.

5.2 Excitonic properties studied by steady-state absorption and photoluminescence

The growth of zig-zag NWs in both semiconducting and metallic SWCNTs from the CoMoCAT76 raw material was verified by ADF-STEM imaging (**Figure 5.2a** and **b**). The selected area electron diffraction (SAED) pattern of a bundle of HgTe-filled semiconducting SWCNTs revealed a feature corresponding to a d-spacing of ~1.92 nm^{-1} (**Figure 5.2c**, **d** and **e**), which agreed well with the experimental distance between Hg atoms in the NW. The steady-state UV-Vis-NIR absorption spectra of the separated metallic and semiconducting CoMoCAT76 SWCNTs are shown in **Figure 5.3**. The presented absorption peaks can be attributed to the oscillators due to interband transitions (S_{11}, S_{22} and S_{33} for semiconducting SWCNTs and
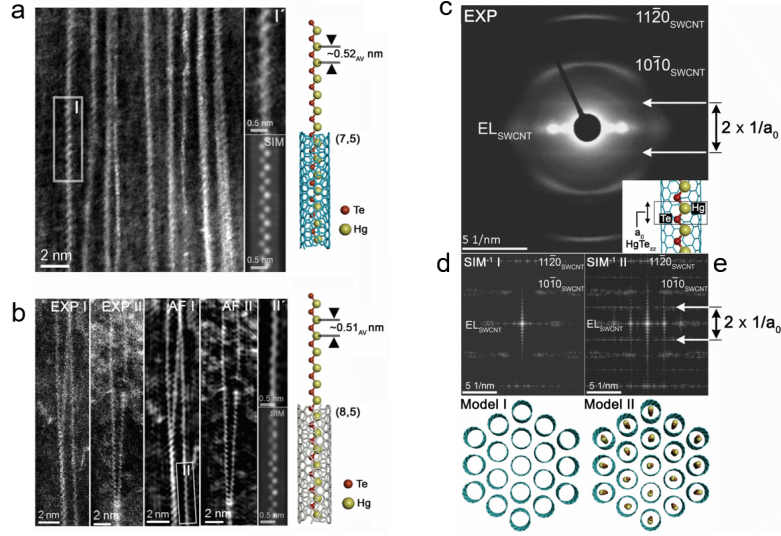
Figure 5.2: (a,b) ADF-STEM images showing zig-zag chains observed in (a) semiconducting and (b) metallic CoMoCAT76 SWCNT samples. Adapted filtered images (AF) of selected regions and simulated pictures (SIM) are also presented. (c) Experimental ED pattern of a bundle of re-agglomerated HgTe-filled semiconducting SWCNTs (inset is the microstructure) with repeating 1D unit cell (lattice parameter a_0). (d,e) SIM^{-1} I and SIM^{-1} II are fast Fourier Transform (FFTs) of multislice simulations of Models I (unfilled SWCNT bundle) and II (zig-zag HgTe filled bundle) respectively, imaged orthogonally to these end-on projections.

M_{11} for metallic SWCNTs). Higher-order transitions such as S_{44} and M_{22} were not well assigned here due to the relatively complicated (n, m) compositions of the samples. For filtrated thin film-state semiconducting and metallic SWCNTs, a dominant absorption peak presented in the UV regime was observed and can be ascribed to a π-plasma feature [139] (**Figure 5.3b** and **c**).

The excitonic absorption and emission energies for different semiconducting (n, m) species can be quantified using photoluminescence excitation (PLE) maps under S_{22} or S_{33} excitation. Following absorption, rapid relaxation to the lowest (S_{11}) excitonic state occurs before light is emitted. PLE maps of the unfilled (**Figure 5.4a**) and HgTe-filled (**Figure 5.4b**) semiconducting samples along with the theoretical transition wavelengths from the empirical Kataura model [28] for each (n, m) (black filled squares) are shown in **Figure 5.4**.

The PLE map of unfilled semiconducting SWCNTs reveals that (7,6) and (7,5) are the two most abundant (n, m) species. After HgTe filling, (8,3), (7,5), (10,2), (9,4) and (8,6) displayed a dramatic relative enhancement in their fluorescence, while the (7,6) fluorescence strength was relatively lower. PLE profiles aver-
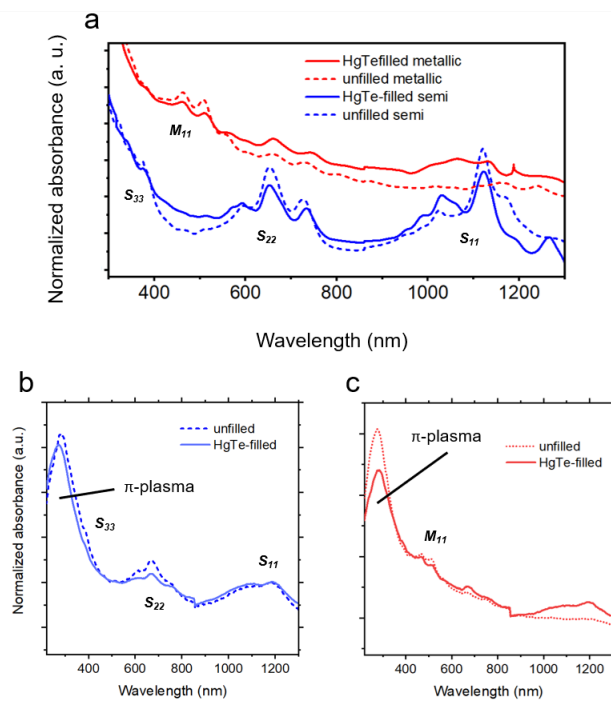
Figure 5.3: Steady-state UV-Vis-NIR absorption spectra of (a) solution-state semi-conducting and metallic CoMoCAT76 SWCNTs, (b) solid thin film-state semiconducting CoMoCAT76 SWCNTs and (c) metallic CoMoCAT76 SWCNTs.
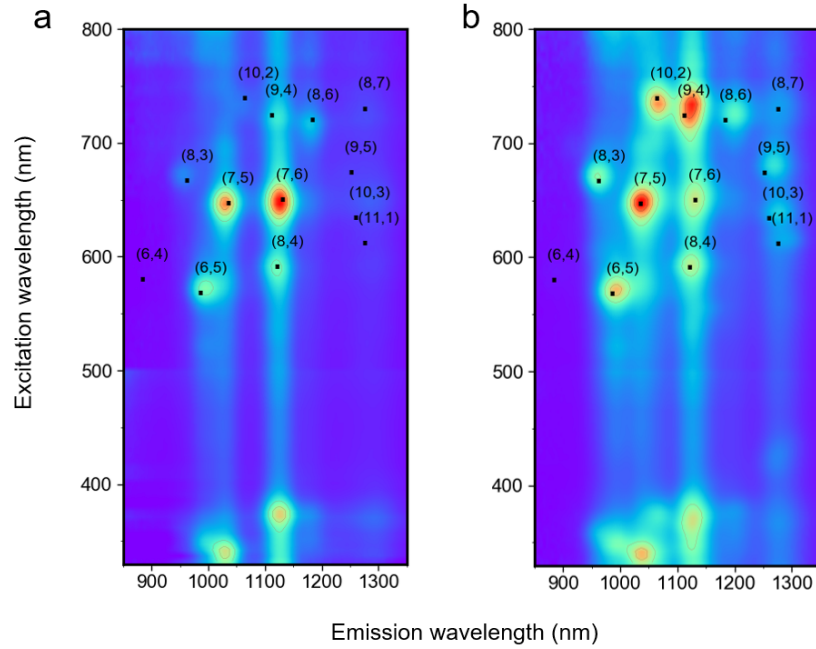
Figure 5.4: (a,b) PLE maps of the solution-state (a) unfilled and (b) HgTe-filled semiconducting SWCNTs. Black dots show the S_{22} and S_{11} wavelengths for each (n,m) species according to the empirical model.[28]

aged over the entire spectral window and for windows covering only particular species are shown in **Figures 5.5** and **Figure 5.6**. The higher fluorescence intensity from HgTe-filled semiconducting SWCNTs points towards either reduced non-radiative interactions for S_{11} excitons, or to a lower radiative rate. An adequate diameter-dependent change in the fluorescence efficiency of SWCNTs has been discovered after filling with organometallic molecular ferrocene, which was further found to be a result of charge transfer from encapsulated molecules that can alter the concentration of charges in SWCNTs [140]. It was thus assumed that the evolution of fluorescence intensity of SWCNTs after HgTe nanowire filling arose from a potential charge transfer between the materials. To know the exact mechanism, further spectroscopic measurements which are capable to characterize individual nanotubes instead of ensembles would be required.

In addition to changes in fluorescence intensity, small shifts in maxima were observed for specific (n,m) species (**Figure 5.4**): for instance the fluorescence peaks of (7,5), (9,4) and (8,6) shifted diagonally towards larger excitation and emission wavelengths. In contrast, the PLE peak for (6,5) SWCNTs (0.75 nm diameter) was not altered, suggesting that filling did not alter the energy of the excitonic states,
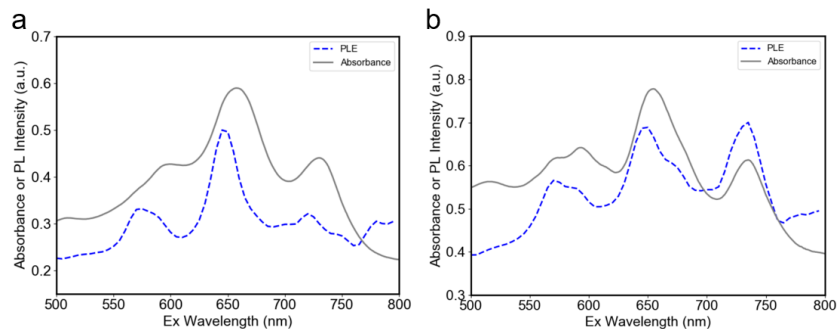
Figure 5.5: Absorbance spectrum and PLE averaged over the entire spectral window (850-1350 nm) of the (a) unfilled and (b) HgTe-filled semiconducting SWCNT sample.
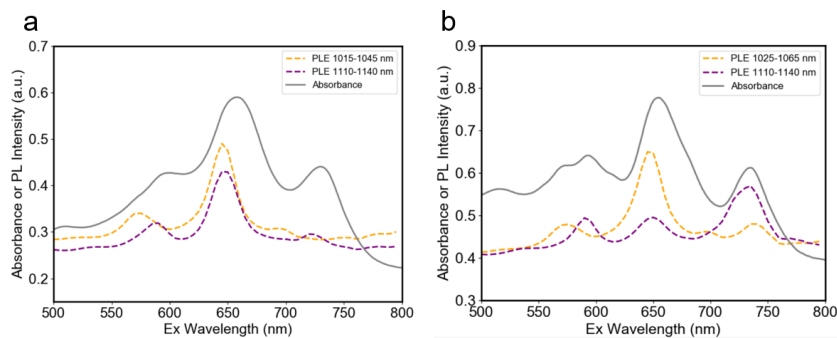
Figure 5.6: Absorbance spectrum and PLE averaged over two specific spectral windows of the (a) unfilled and (b) HgTe-filled semiconducting SWCNT sample. The orange and purple PLE profiles represent contributions of emission signals from (6,5)/(7,5) and (8,4)/(7,6)/(9,4), respectively.
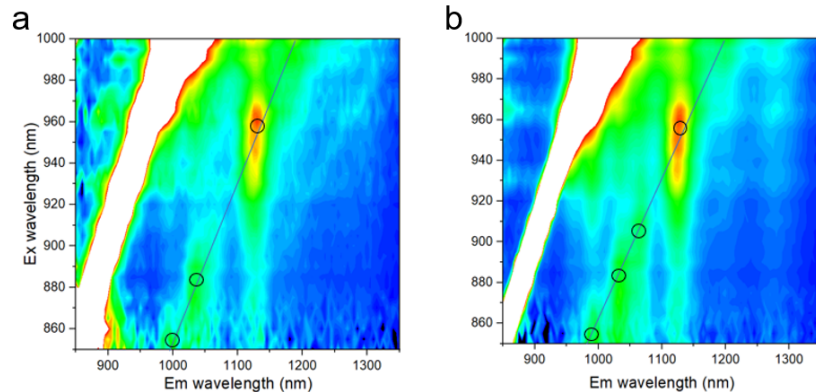
Figure 5.7: PLE maps of the unfilled and HgTe-filled semiconducting SWCNT samples by excitation in the NIR wavelengths. The phonon sidebands for S_{11} excitons of different (n, m) are marked by black open cycles.

or that the narrowest tubes were not filled.

By exciting the semiconducting samples at NIR wavelengths (850-1000 nm) close to S_{11}, additional PLE signals can be resolved (**Figure 5.7**, black circles) beneath the first order Rayleigh scattering line, and which can be assigned to emission at the G-mode phonon sidebands of the S_{11} excitons [87]. After HgTe NW filling the semiconducting SWCNTs presented an additional signal peak centered at $\sim$1060 nm (**Figure 5.7b**), further evidencing stronger emission from (10,2) CNTs after filling.

5.3 Phonon properties studied by resonant Raman spectroscopy

5.3.1 Vibration features of chirality-refined SWCNTs

The anti-Stokes Raman resonance features of SWCNTs were investigated in order to confirm chirality assignments, and to examine the vibrational modes and electronic properties of the material. For both of the semiconducting and metallic species sorted from the CoMoCAT76 SWCNTs, RBMs were observed at Raman shifts of 200-350 cm^{-1} (**Figure 5.8** and **Figure 5.9**), in accordance with the small (< 1 nm) diameters of these SWCNTs. Under an excitation wavelength of 660 nm (an energy of 1.88 eV), two intense peaks were found at 267 and 286 cm^{-1} (**Figure 5.8a**) for the semiconducting SWCNTs. According to the relation $d_t = a/\omega_{\mathrm{RBM}}$, where $a = 237$ nm cm^{-1} and ω_{RBM} is the wavenumber of the RBM [141], these two RBM features correspond to $d_t = 0.89$ nm and $d_t = 0.83$ nm. Together with the result of chirality assignment based on PLE maps (**Figure 5.4**), these two RBMs feature the
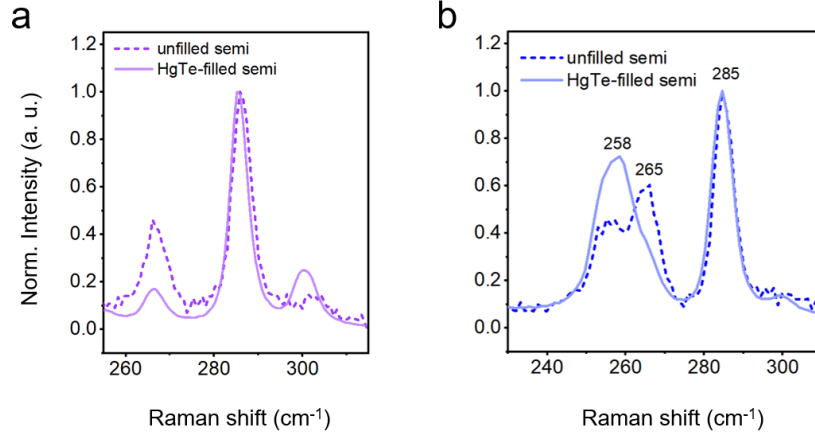
Figure 5.8: Raman RBM spectra of semiconducting SWCNT samples under (a) 660 nm and (b) 633 nm excitation. The spectra are background-subtracted and normalized to the intensity of data point at 500 cm^{-1}, where there is no feature related to carbon nanotubes or the substrate.

vibrations of (7,6) and (7,5) SWCNTs, respectively. In contrast, for the metallic samples which were examined at an excitation wavelength close to the M_{11} resonance (488 and 514 nm), the two main RBMs were found to be located at ~ 266 cm^{-1} and ~ 250 cm^{-1} (**Figure 5.9**), corresponding to SWCNTs with diameters of 0.891 nm and 0.948 nm, respectively. According to the experimentally determined M_{11} energies for various metallic (n, m) species in previous studies (**Appendix A**), (n, m) species belonging to $(2n + m) = 21$ family are more likely to be excited resonantly under these two excitation wavelengths and produce enhanced Raman intensities. Based on the above estimated nanotube diameters, we assigned these two RBMs to vibration features of (8,5) and (7,7), respectively.

It is noted that HgTe NW filling results in a slight softening (or redshifting) of the RBM's Raman shift for both semiconducting and metallic SWCNTs. This is somewhat unanticipated as molecular filling normally favors the hardening (blue shifting) of the RBM as previously demonstrated by both theoretical [142] and experimental [80; 15] results. More details of the analysis were shown in **Chapter 7**.

The Raman spectra of SWCNTs at higher frequencies, such as the tangential mode (G mode) and the double resonance G' mode, were further studied to investigate the changes in the electronic properties of the SWCNTs induced by the HgTe zig-zag filling. Spectra of the G modes for the semiconducting SWCNTs under 660 nm and 633 nm excitation are shown in **Figure 5.10a** and **c**. In both cases, the best fit to experimental spectrum required 5 or 6 Lorentzians, which can be
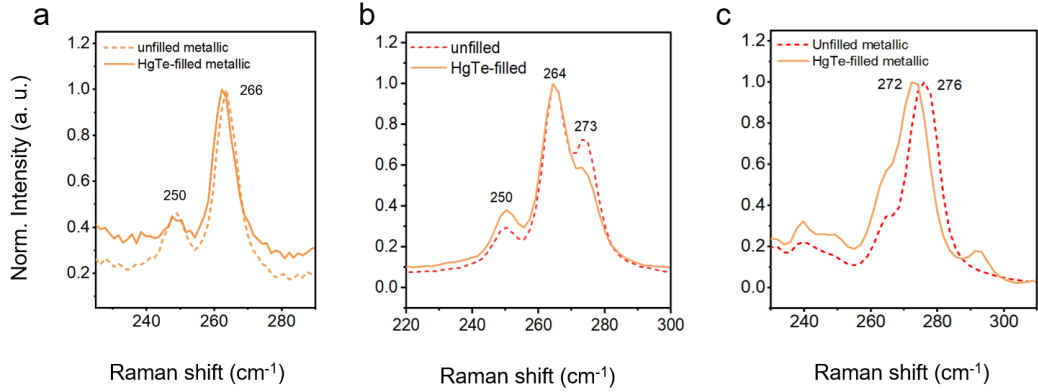
Figure 5.9: Raman RBM spectra of metallic SWCNT samples under (a) 488 nm, (b) 514 nm and (c) 532 nm excitation. The spectra are background-subtracted and normalized to the intensity of data point at 500 cm^{-1}, where there is no feature related to carbon nanotubes or the substrate.

attributed to zone-center phonon modes with A_{1g}, E_{1g} and E_{2g} symmetries [143]. The strongest, higher-frequency band (or G$^+$ band) consists of two Lorentzians centered at $\sim 1590\,\text{cm}^{-1}$ and $\sim 1600\,\text{cm}^{-1}$, which are assigned to the combined $A_{1g}+E_{1g}$ mode and E_{2g} mode, respectively. The low-frequency band (or G$^-$ band) comprised three Lorentzians, and which can be assigned to another E_{2g} and two $A+E$ modes. The double resonance G' modes which are linked to the two-phonon scattering processes near the K point,[22; 144] are reported in **Figure 5.10b** and **d** for the semiconducting SWCNTs. One strong peak was observed around $2600\,\text{cm}^{-1}$, which was decomposed into Lorentzian peaks.

The G and G' spectra of the metallic filled and unfilled SWCNTs (**Figures 5.11**) are more complex than those for the semiconducting samples and can be deconvoluted into a BWF lineshape and several Lorentzians. Here the BWF line at $1540\text{-}1550\,\text{cm}^{-1}$ and a Lorentzian component at $\sim 1580\,\text{cm}^{-1}$ are assigned to the non-armchair metallic species (8,5), while a narrower Lorentzian peak at $\sim 1590\,\text{cm}^{-1}$ is linked to the G^+ mode of armchair species[145; 146] or of residual semiconducting tubes.[147] The G' modes of the metallic tubes (**Figure 5.11d-f**) showed a clear double-peak structure, which is only found for non-armchair metallic tubes,[120] and which results from trigonal warping around the K point [120].

5.3.2 Spectral shift and linewidth broadening of Raman modes
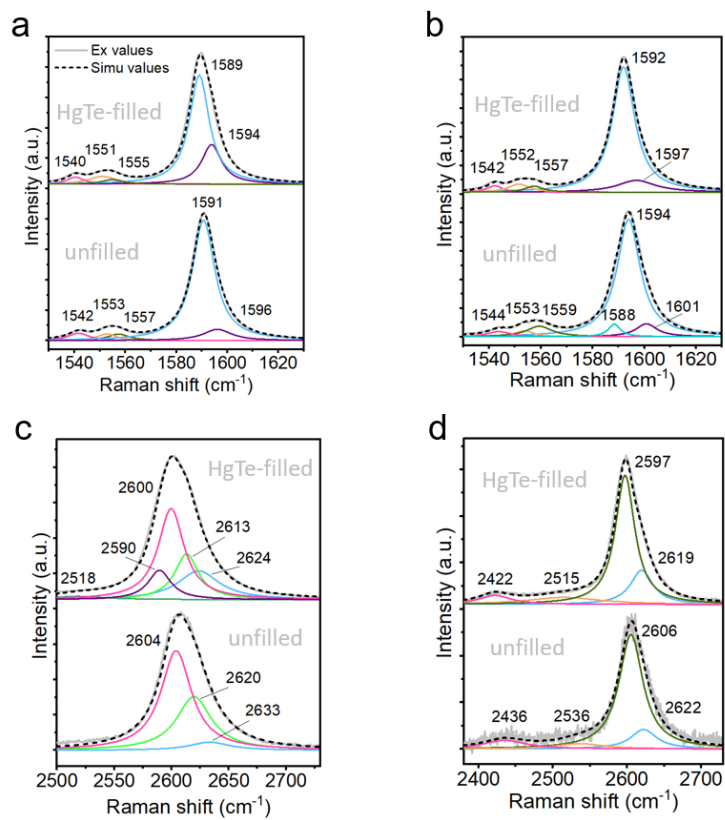
Figure 5.10: High-frequency G and G' modes of semiconducting SWCNTs under (a,c) 633 nm and (b,d) 660 nm excitation.
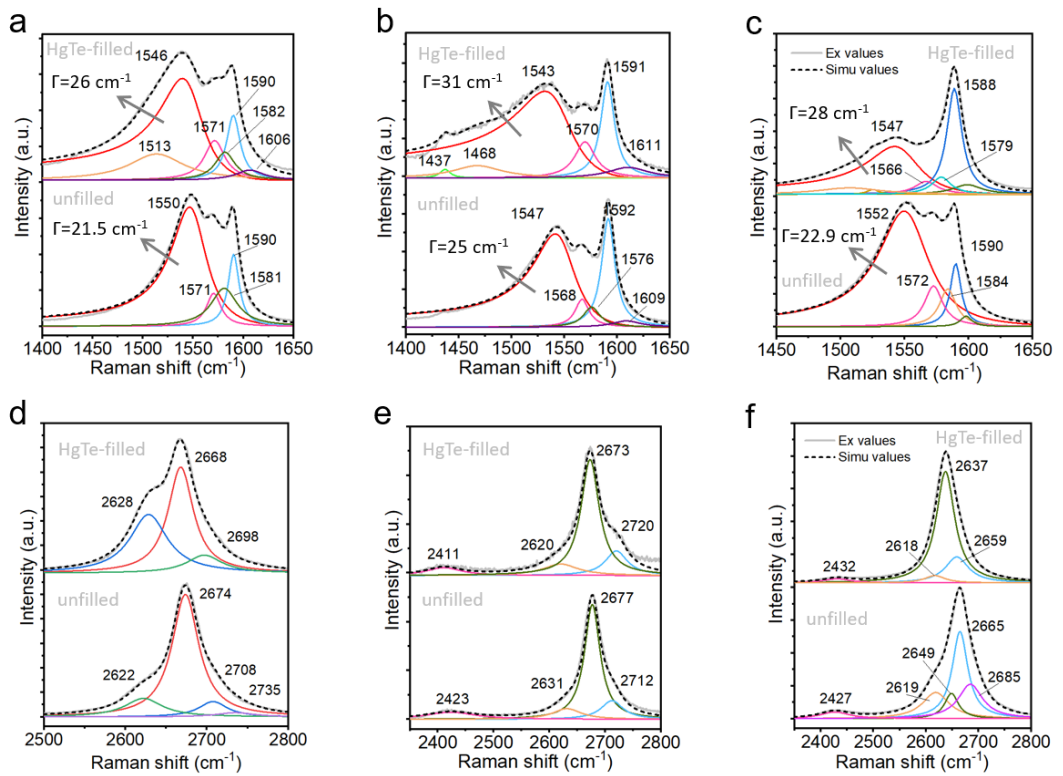
Figure 5.11: High-frequency G and G' modes of metallic SWCNTs under (a,d) 514 nm, (b,e) 488 nm and (c,f) 532 nm excitation.

Table 5.2: Fitting parameters for the BWF lines of unfilled
and HgTe-filled metallic SWCNTs

	ω_{BWF} (cm^{-1})	$1/q$	Γ (cm^{-1})
488 nm excitation			
unfilled	1547	-0.22	25
HgTe-filled	1543	-0.45	31
514 nm excitation			
unfilled	1550	-0.16	21.5
HgTe-filled	1546	-0.23	26
532 nm excitation			
unfilled	1552	-0.13	22.9
HgTe-filled	1547	-0.18	28

ω_{BWF}–frequency of the BWF lineshape, q–electron-phonon coupling coefficient,
Γ–linewidth of the BWF profile.

Filling with HgTe NWs redshifted nearly all of the G and G' components of the semiconducting and metallic SWCNTs, as indicated by the difference in Raman peak position after filling, $\Delta\omega$, in **Figure 5.10** and **5.11**. While the G^+ resonance position is insensitive to the SWCNT diameter, it redshifts when relatively more electrons are present on the SWCNTs [148; 120], suggesting the filling has acted like a weak donor.

The effect of HgTe NW filling on the BWF feature was also highlighted by a broadening in the linewidth (**Figure 5.11a-c**). Under 488 nm excitation the spectral broadening increased from $\Gamma = 24\,cm^{-1}$ to $32\,cm^{-1}$ after filling (from $21.5\,cm^{-1}$ to $26\,cm^{-1}$ with 514 nm excitation). A summary of the fit parameters for the BWF models is provided in **Table 5.2**. Such a broadening and frequency downshifting of the BWF line as a result of HgTe NW filling is interpreted as follows: The BWF line of metallic SWCNTs is an axial longitudinal optical (LO) phonon mode, arising from the strong electron-phonon coupling at the band crossing (zero charge) point, that is, single particle electronic excitations near the Fermi level to the phonon [149; 150]. If the metallic nanotube is charged such that the Fermi level lies away from the band crossing point, linewidth narrowing and frequency upshifting of such a mode are expected [151; 152]. Therefore, a linewidth broadening and frequency downshifting of the BWF line for metallic SWCNTs studied here can be regarded as the result of a stronger electron-phonon coupling that arises from the charge transfer

68
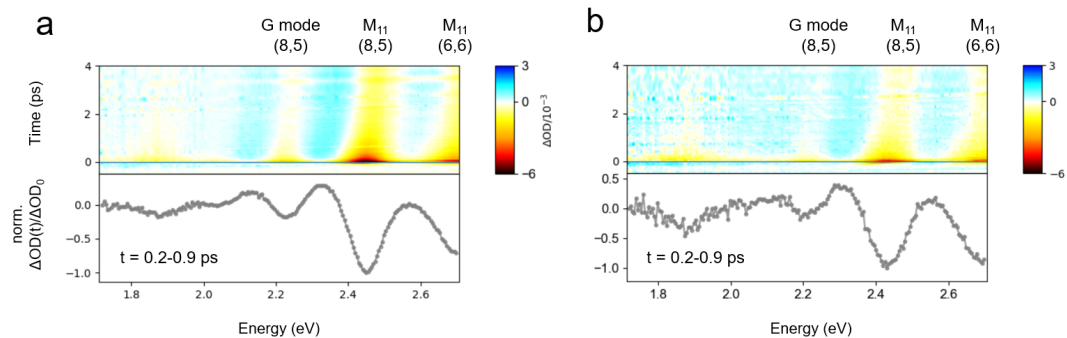
Figure 5.12: (a,b) Variations of the TA signals (ΔOD) against the pump-probe time delay and the probe energy for the solution-state (a) unfilled and (b) HgTe-filled metallic SWCNTs. The applied pump energy and fluence were $2.82\,\mathrm{eV}$ $(440\,\mathrm{nm})$ and $1.13\,\mathrm{mJ}\,\mathrm{cm}^{-2}$ per pulse, respectively.

induced by encapsulated HgTe NWs.

The type of charges donated by NWs was then discussed. A change in the G mode spectral property under a varying degree of charging had been investigated based on the electrostatical gating experiment reported elsewhere [153]. It was shown that the frequency increased monotonically at a more negative voltage. Given that the as-synthesized metallic SWCNTs lie well below the band crossing point (zero charge point), the discovered results implies that the Fermi level lies further away from the band crossing point for positively charged nanotubes compared to uncharged nanotubes, resulting in a reduced electron-phonon coupling. Since a frequency downshift of the BWF line for metallic SWCNTs after filling was found in our study, it is deduced that the HgTe NWs donated negative charges to the nanotubes.

5.4 Exciton and phonon decay dynamics investigated by transient absorption spectroscopy

Femtosecond transient absorption (TA) spectroscopy of the unfilled and HgTe-filled SWCNTs was studied to investigate the consequences of HgTe NW incorporation in more detail. In this chapter only features of metallic SWCNTs were discussed. Experimental TA signals (change in absorbance, ΔA) of the solution-state metallic SWCNTs against the probe energy and pump-probe delay are shown in **Figure 5.12**.

In the heat maps, several negative photo-bleaching (PB) features can be discerned in the experimental spectral range (dark red areas), which correspond
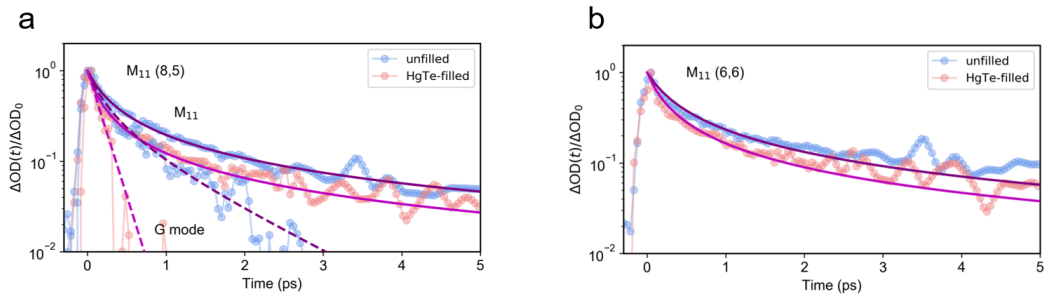
Figure 5.13: (a,b) TA kinetics of the M_{11} bands for (8,5) and (6,6) as well as the G mode of (8,5). Fits (purple for the unfilled and magenta for the HgTe-filled) are as described in the text, based on the bimolecular rate equation model in **eq 5.6**.

to the M_{11} excitonic states of (6,6) and (8,5) chiralities. The few positive photo-absorption (PA) features discovered at slightly lower energies than those of the PB features can be attributed to the transient band renormalization or a change in the linewidth of M_{11} resonances. According to the results of Raman measurements on metallic SWCNTs in the previous section (**Figure 5.9**), the RBM intensity of (8,5) SWCNTs was found to be significantly higher than the intensity of (7,7) SWCNTs. Due to the fact that these two types of SWCNTs show rather similar M_{11} transition energies (see the experimentally determined interband transition energies of them in **Figure A.1** in **Appendix A**), the feature at $2.45\,\mathrm{eV}$ was assumed to result mainly from (8,5) rather than (7,7). Also evident in the TA heat maps is a PB feature at around $2.25\,\mathrm{eV}$, $0.2\,\mathrm{eV}$ below M_{11} for (8,5), which we assign to an exciton-phonon sideband created by the G mode. The strong electron-phonon coupling in SWCNTs can create phonon sidebands that can be seen directly in the absorption spectra of SWCNTs [154].

In **Figure 5.13** the dynamics of features assigned to (8,5) and (6,6) are reported. The observed non-exponential transient absorption dynamics were modelled by assuming that the normalised transient absorption change $\Delta\mathrm{OD}(t)/\Delta\mathrm{OD}_0 = n(t)/n_0$, where $n(t)$ is the population of excitons, $n_0 = n(t = 0)$ is the maximum exciton density. Assuming that a rate of change of $n(t)$ can be given by the rate equation **eq 5.3**, the kinetics can be analyzed within the scheme of a bi-exciton Auger process.

After normalization by n_0, the time evolution of the transient absorption signal for times $t > 0$ is

$$\frac{n(t)}{n_0} = \frac{k}{(k + \gamma n_0)e^{kt} - \gamma n_0},$$ (5.6)

70

and hence k and γn_0 are the fit parameters. We adopted this approach to fit our TA data because the maximum exciton density n_0 was hard to quantify precisely. For the M_{11} states of (8,5) and (6,6) tubes, the decay dynamics were bimolecular throughout the experimental time window, according to a reasonable fit to the experimental trace without including the monoexponential term (*i.e.* assuming $k \approx 0$), which is the case when the monomolecular rate is much smaller than the Auger recombination rate. Good agreement between model and experiment was therefore found without the need for a contribution from k (*i.e.* $k \ll 0.1\,\mathrm{THz}$), by taking $\gamma n_0 = 4.13\,\mathrm{THz}$ and $3.27\,\mathrm{THz}$ for unfilled (8,5) and (6,6) tubes. The experiments were conducted under the same non-resonant excitation conditions and on samples with similar absorbance. Assuming the same internal conversion rate to M_{11} excitons for each sample (during the first $100\,\mathrm{fs}$ time resolution of the pump-probe experiment) we therefore assume n_0 did not vary with chirality or filling, and instead discuss the mechanisms that can alter γ.

The lower Auger rate γ for unfilled (6,6) SWCNTs in comparison to (8,5) can be understood as follows. Within a parabolic two-band approximation, *i.e.* ignoring any electron scattering processes between subbands, and neglecting the electron-phonon interaction, the Auger rate for nanotubes can be estimated from perturbation theory to scale as $\gamma \propto (E_b/E_g)^3$, where E_b is the exciton binding energy and E_g is the single-particle energy gap. The narrower diameter of (6,6) tubes $(0.814\,\mathrm{nm})$ increases E_g (as well as M_{11}) relative to that of (8,5) tubes $(0.889\,\mathrm{nm}$ diameter). Hence the lower γ for (6,6) tubes may result solely from diameter-driven changes to the electronic bandstructure. However, this discussion ignores the important role that electron-phonon coupling plays in metallic carbon nanotubes, as evident from their Raman features (discussed above) and also evidenced by time-domain atomistic simulations of Auger decay, where the bi-exciton Auger process is shown to be accompanied by energy loss to phonons with different frequencies and the rate of electron-phonon coupling is generally higher than the that of Auger recombination in carbon nanotubes [155]. The Auger decay processes were found to involve phonon-assisted transitions at energies up to and including the G mode [155]. Hence changes to the G mode's strength, energy and linewidth may be expected to alter Auger decay rates.

HgTe zig-zag filling directly increased the extracted Auger rates to $\gamma n_0 = 7.17\,\mathrm{THz}$ and $5.07\,\mathrm{THz}$ for (8,5) and (6,6) metallic SWCNTs. As there was negligible change in the M_{11} energy after filling, the around $60\,\%$ higher γ for the filled tubes can be interpreted as resulting from stronger electron-phonon coupling leading to a greater Auger rate. Further evidence for the enhanced role of electron-phonon

coupling comes from the G-mode sideband (at 2.25 eV), the dynamics of which are reported in **Figure 5.13**. Exciton-exciton annihilation creates a single, higher energy electron-hole pair, which then relaxes by optical phonon emission. The G-sideband's dynamic for the unfilled (8,5) tubes was modelled (dashed blue line) by the same Auger term ($\gamma n_0 = 4.13\,\text{THz}$) but with an additional monomolecular channel at rate $k = 1.0\,\text{THz}$, corresponding to a lifetime $\tau = 1/k = 1.0\,\text{ps}$. This is in excellent agreement with the lifetime of the G-mode phonon, $\tau = 1.1\,\text{ps}$, measured directly by time-resolved Raman spectroscopy [154]. After HgTe zig-zag filling, however, the G-mode sideband decayed much more rapidly, and was fit (dashed red line) by a single exponential decay with lifetime $\tau = 0.16\,\text{ps}$. This faster decay may signify that HgTe filling strains the SWCNTs [77], thereby boosting the anharmonic relaxation pathways for the G-mode phonons to relax into other phonons within the SWCNT. Alternatively, the prescence of encapsulated insulating nanowire chains has been shown theoretically to increase hot phonon relaxation rates by providing extra phonon decay channels [156]. A full list of parameters for the fitted dynamic curves at different probe energies can be found in **Table 5.3**.

Table 5.3: Fitting parameters for the M_{11} TA kinetics of unfilled and HgTe-filled metallic SWCNTs

	2.695 eV (M_{11} of (6,6))	2.445 eV (M_{11} of (8,5))	2.231 eV (G mode of (8,5))
γn_0 (THz)			
unfilled	3.27 ± 0.09	4.13 ± 0.06	4.13 ± 0.21
HgTe-filled	5.07 ± 0.20	7.17 ± 0.13	-
k (THz)			
unfilled	-	-	1
HgTe-filled	-	-	6.25

γ–bimolecular recombination rate constant, k–monomolecular decay rate constant, n_0–exciton population at $t = 0$.

It should be noticed that the investigated solution-state metallic SWCNT samples were exceptionally unstable. They were found to sediment within hours after the chromatography experiment. Therefore, conducting further TA characterization under varied testing conditions (*e.g.* different pump fluences) may become problematic as it may not give a trusted signal response. A future solution to

this issue is by using surfactants that can improve the monodispersivity of metallic nanotube samples.

5.5 Plasmonic resonance of SWCNTs investigated by far-infrared spectroscopy

To investigate the impact of HgTe filling on the conductivity of free carriers, mid- and far-infrared attenuation spectroscopy of the materials produced by the vacuum filtration method were studied to investigate the impact of HgTe filling on the conductivity of free carriers in SWCNTs. To carry out the study, the SWCNTs were prepared into thin films (30-200 nm thick as determined by AFM) on the quartz substrates by a vacuum filtration method. The spectra of semiconducting and metallic SWCNT films were reported in **Figure 5.14**. The broad absorption maxima in the free-carrier absorption regime (below 3000 cm^{-1}) result from the axial plasmon resonance of finite length nanotubes [99; 109; 110; 117]. The absorbance profiles for semiconducting and metallic SWCNTs are distinctly different. The semiconducting SWCNTs exhibited a narrower absorption peak centered at around 300 cm^{-1}, while the metallic tubes had a broader absorption peak around 1000 cm^{-1}. We note that the theory of axial plasmons in SWCNTs [109] predicts the plasmon resonance frequency to vary inversely with tube length, l, according to $\omega_0 = \pi v_q(l,d,N)/l$, where $v_q(l,d,N)$ is the plasmon mode velocity, a function of the tube diameter $d = 0.88$ nm and length, and also of the number of nanotubes in each bundle [109]. For a single nanotube, the resonance frequency ω_0 relates to the tube length l by $\omega_0 = v_q(\pi/l)$, where $v_q = 4v_F\{[e^2/(3\pi\epsilon a_0\gamma_0)^{0.5}]K_0(\pi d_t/2l)I_0(\pi d_t/2l)\}^{0.5}$, with v_F the fermi velocity, ϵ the static dielectric constant, a_0=0.142 nm the distance between nearest carbon atoms, d_t is nanotube diameter, $\gamma_0 \approx 3.2$ eV a force constant, K_0 and I_0 are the first and second type, respectively, of the modified Bessel function [99]. The bundle dependence has not been previously considered in comparisons between the experimental plasmon frequency and theory [99; 110; 157]. For the thin films studied here, each bundle can contain up to hundreds of SWCNTs. When a bundle contains N metallic nanotubes with same length, the kernel of the Coulomb interaction is effectively multiplied by N [109]. As a result, the frequency will be multiplied by $\sqrt{N}$. It thus interprets that the observed plasmon frequency is higher than would otherwise be expected for these tubes lengths (over 1 μm for semiconducting tubes and around 200 nm for the metallic tubes, according to AFM).

After HgTe filling, the infrared attenuation of the semiconducting SWCNTs was found to remain almost the same, whilst that of the metallic SWCNTs displayed
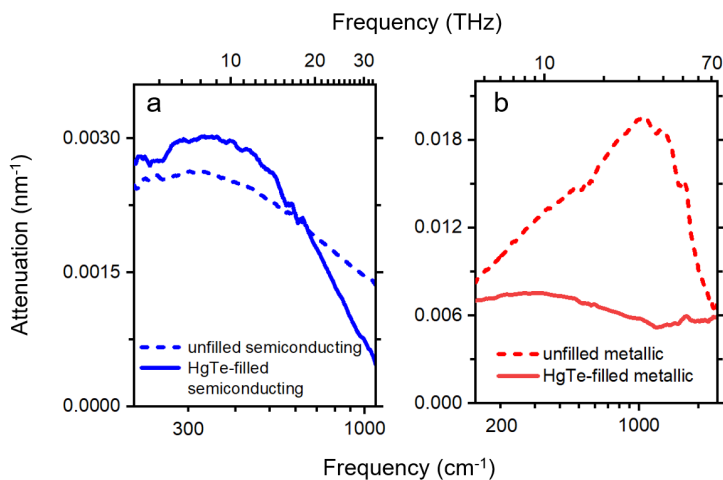
Figure 5.14: (a,b) Room-temperature infrared attenuation of the semiconducting and metallic SWCNT films divided by their thicknesses.

a significant reduction in strength and a substantial redshift. These results indicate that HgTe filling did not lead to a significant change in the equilibrium charge carrier density of the semiconducting SWCNTs but can efficiently lower the free carrier density in the metallic SWCNTs. Pseudogaps have been reported to open when metallic tubes form bundles [158], and which might reduce therefore reduce the free carrier density and conductivity of bundles of metallic SWCNTs. In this case however the pronounced difference between reference and filled metallic samples, which had similar bundle number, allows us to infer that the IR absorbance was changed by the presence of HgTe. We advance the hypotheses that the presence of HgTe NWs modifies either the bandstructure of each individual metallic SWCNT, or alters the pseudogap derived from intertube coupling in bundles, but further work is needed to clarify the observed changes.

5.6   Questions addressed in this chapter and conclusions

To summarize, we carried out optical characterizations on unfilled and HgTe NW-filled CoMoCAT76 SWCNTs. Using gel column chromatography, semiconducting and metallic nanotubes can be extracted from the raw SWCNT material, which both contained mainly (n, m) species with diameters of < 1 nm. Electron microscopy revealed that zig-zag nanowire is the dominant structure in both semiconducting and metallic SWCNTs. Based on Raman spectroscopy, a frequency downshifting and linewidth broadening of the characteristic G mode of metallic SWCNTs (Breit-Wigner-Fano (BWF) line) after the encapsulation by HgTe nanowires had been

discovered, suggesting an increased electron-phonon coupling strength.

Transient absorption measurements had been carried out in the next in order to investigate the exciton dynamics of metallic SWCNTs. Photo-bleaching features ($\Delta O.D. < 0$) assigned to the exciton and phonon of metallic SWCNTs were discovered. It was found that the exciton dynamics was dominated by a bi-exciton Auger recombination process and showed a faster decay rate after the SWCNT was filled by nanowire. As per the prediction that Auger recombination in SWCNTs was accompanied by energy loss to phonons, a change in the recombination rate after filling is deduced to be a consequence of created additional boosted phonon decay channels due to an enhanced electron-phonon coupling strength. As Auger recombination is a non-radiative process, it limits the quantum efficiency of carbon nanotubes, which can obstruct their applications in phototransistors and optoelectronics. Our experimental results showed that the Auger recombination dynamics of SWCNTs can be altered in a predictable manner by introducing 1D guest materials inside, which may create a new pathway to optimize the performance of SWCNT-based optoelectronic devices.

Chapter 6

Effect of SWCNT Filling by Nanowires with Different Atomic Structures

In this chapter we report the optical properties of filled carbon nanotubes with different average diameters (less than 1 nm for CHASM SWCNTs and ∼ 1.6 nm for TUBALL SWCNTs). It was revealed that the nanotube diameter is vital for the structure of filling NWs, in which way the optical properties of SWCNTs can be finely tuned.

6.1 Dependence of the nanowire structure on the size of SWCNT

In the last chapter the effect of zig-zag HgTe NWs, a distorted atomic chain, on the optical performance of SWCNT was described and discovered an enhancement of the electron-phonon coupling strength attributed to the potential vibration mode of the discrete structure. In this chapter, the effect of nanotube filling by NWs with other types of structures was discussed.

Thus far the discovered 1D NW structures inside SWCNTs with a width of less than two atoms include linear chains [70; 74; 77; 159], zig-zag chains [70; 74; 159], helical chains (3H coils) [70; 74] and two atom-by-one atom-thick chains with an ordered [74; 159] or twisted [77; 159] geometry. According to a dependence of estimated lowest formation energies of encapsulated nanowires on nanotube diameter based on results of *ab initio* calculations [74] (see details in **Appendix B**), it is expected that only linear or slightly distorted one atom-thick chains (*e.g.* zig-zag chains) can form
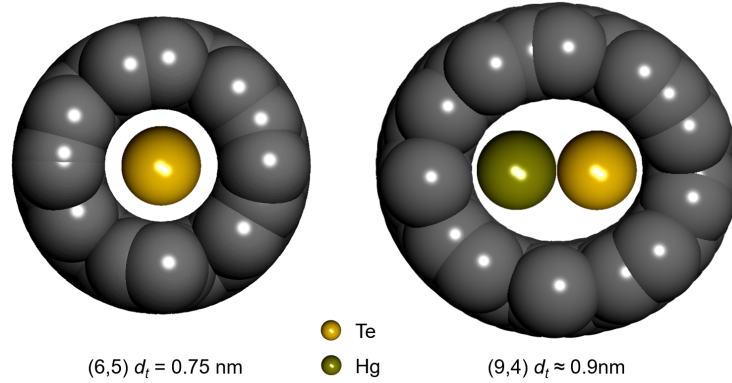
Figure 6.1: Proposed structure models of a (6,5) nanotube filled by linear HgTe nanowire and a (9,4) nanotube filled by two atom-by-one atom-thick 2×1 HgTe nanowire. The encapsulation of 2×1 nanowire can lead to a certain extent of structure distortion in (9,4), resulting in an oval-like cross section [77].

inside (6,5) (nanotube diameter $d_t \sim 0.75$ nm), while two atom-by-one atom-thick (2×1) chains shall exist in wider SWCNTs ($d_t \approx 1$ nm), such as (9,4) (~ 0.9 nm), (10,3) (~ 0.92 nm) and (8,6) (~ 0.95 nm). The proposed structure models for the two kinds of filled nanotubes are shown in **Figure 6.1**

Investigating such a structural evolution would help to understand the fundamental physics behind the design of unconventional 1D nanomaterials. In this chapter, optical properties of SWCNTs filled by NWs with different atomic structures, including one atom-thick linear chains, two atom-by-one atom-thick (2×1) chains and multiple atom-thick (n>2 along each direction in the lattice plane parallel to the nanowire cross section) chains, as were encapsulated in two types of SWCNT products, CHASM ($d_t \sim 0.7$-1.4 nm) and TUBALL ($d_t \sim 1.6$nm), and were characterized based on a range of spectroscopic measurements.

6.2 Absorption and photoluminescence of SWCNTs filled by different types of nanowires

To enable growth of NWs with different widths and study the effect quantitatively, SWCNTs from different raw product were used and materials purification was applied in order to extract desired chiralities. It was particularly discovered that the NWs grown inside CHASM SWCNTs ($d_t \sim$0.7-1.4 nm) which were treated by a simple centrifugation step showed dominant structures of one atom-thick chain (linear chain) and 2×1 chain (**Figure 4.12b** and **4.12c**). By subsequent gel column chro-
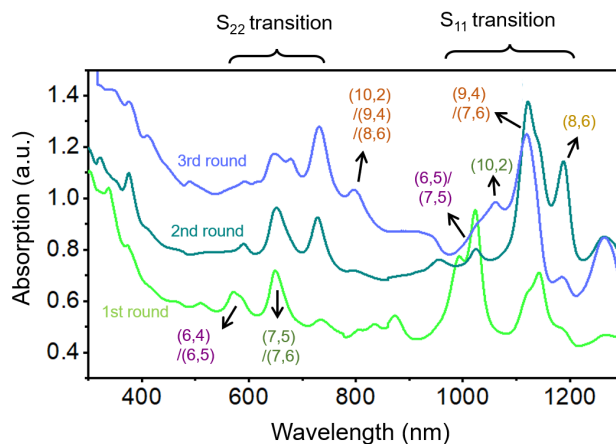
Figure 6.2: Steady-state UV-Vis-NIR absorption spectra of the CHASM SWCNTs sorted based on gel column chromatography (green, dark purple and light purple curves are the absorption spectra of SWCNTs obtained during the 1st, 2nd and 3rd round of separation experiment). Absorption lines assigned to different (n, m) species are marked in the graph.

matography purification, small-diameter semiconducting species can be extracted. The absorption spectra shown in **Figure 6.2** revealed that narrowest species such as (6,4), (6,5) and (7,5) can first be separated, followed by larger-diameter species. As one atom-thick chain was found to be the dominant nanowire structure in these extracted portions (**Figure 4.12d**), it suggests a strong link between the nanotube size and atomic structure of NWs, which was in a good agreement with the prediction by theoretical calculations.

Wider NWs were found to preferentially form inside the larger-diameter TUBALL SWCNTs (**Figure 4.13**) and HiPco SWCNTs (**Figure 6.3**). Since the TUBALL SWCNTs can offer a significantly higher yield of NW filling compared to the HiPco SWCNTs, we applied them as the source to selectively grow wide NWs. It was revealed that materials purification based on ATP extraction or gel column chromatography protocol did not lead to a notable refinement of chirality for such TUBALL SWCNTs.

The PLE contour maps of CHASM SWCNTs obtained after the centrifugation step are shown in **Figure 6.4**. The unfilled sample was found to display a surprisingly weak fluorescence, with the maximum emission observed at the excitonic energies of (7,6). A possible explanation for such a weak emission from these SWCNTs is the existence of heavily bundled nanotubes (as determined by the AFM image in **Figure 4.11b**), which increases the chance for metallic nanotubes to exist in them, leading to a strong exciton energy transfer (EET) and eventually quenching
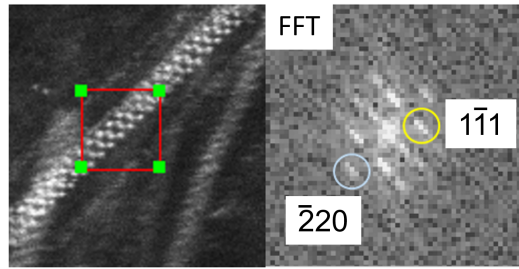
Figure 6.3: ADF-STEM image (left) showing two nanotubes filled by wide NWs picked up from HiPco SWCNT sample. The fast-Fourier-transform (FFT) of part of the ADF-STEM image marked by the red square is shown on the right, indicating that the NW has a zinc-blende (face-centered cubic) structure.

the fluorescence. For the HgTe-filled CHASM SWCNTs, a huge contrast in the PL feature can be found: the smallest (*e.g.* (5,4), (6,4))) and large-diameter ($d_t > 0.88$ nm, such as (7,6), (9,4), (8,6)) species produced a strong emission, whereas the fluorescence of medium-sized species (*e.g.* (6,5) and (7,5)) remained was significantly quenched.

The fluorescence of CHASM species extracted by gel column chromatography in the next step were then characterized. Both the unfilled and HgTe-filled CHASM SWCNTs displayed a trend towards the extraction of larger-diameter (n, m) species with an increase in the round of chromatography experiment (**Figure 6.5**). Additionally, it was found that the three (n, m) species in unfilled SWCNTs that gave highest intensities of emission during the first three rounds of experiment were (6,4), (7,5) and (7,6), which were different from the three (n, m) species in HgTe NW-filled SWCNTs ((7,5), (7,6) and (9,4)).

For a more detailed analysis, the extracted PLE profiles were compared with the steady-state absorption spectra of the SWCNT sample. In **Figure 6.6**, the PLE profiles averaged over the emission wavelength windows of fluorescence signals for different (n, m) species were plotted together with the absorption spectra of these SWCNTs. It was revealed that the energies for most of discovered absorption peaks matched well with those for the S_{22} states of different (n, m) species. The emergence of the rest of absorption features can, however, not be interpreted to be a result of inter-band transitions as can be clarified based on the PLE profiles. Their possible origins are instead EET between adjacent SWCNTs or the phonon sidebands. From the absorption spectra of fractions first extracted from the unfilled and HgTe-filled CHASM SWCNTs, a peak at just above 500 nm can be assigned to a phonon sideband (G mode) of (6,5) (**Figure 6.6a** and **d**). Additionally, a broad photoluminescence peak situated right at the wavelength of S_{11} transition for (6,4) can also

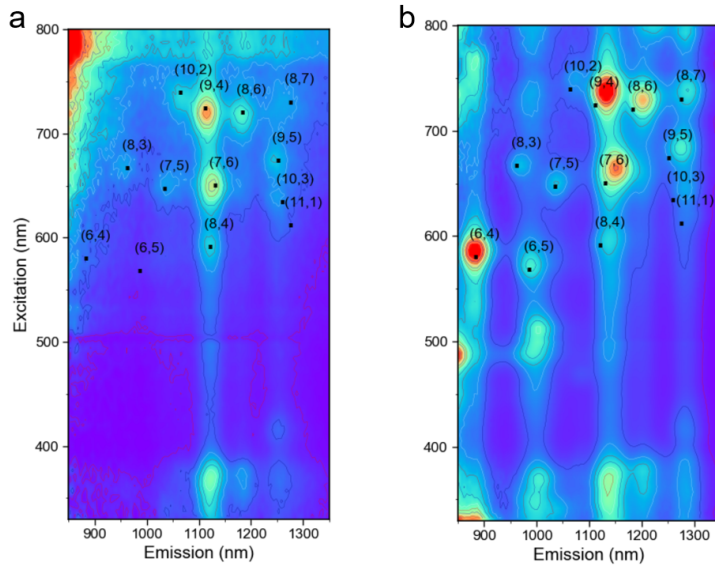Figure 6.4: Figure 5.1.4 PLE maps of the as-centrifuged CHASM SWCNTs without (a) and with (b) HgTe filling. Black dots show the S_{22} and S_{11} wavelengths for each (n, m) species according to the empirical model.[28]
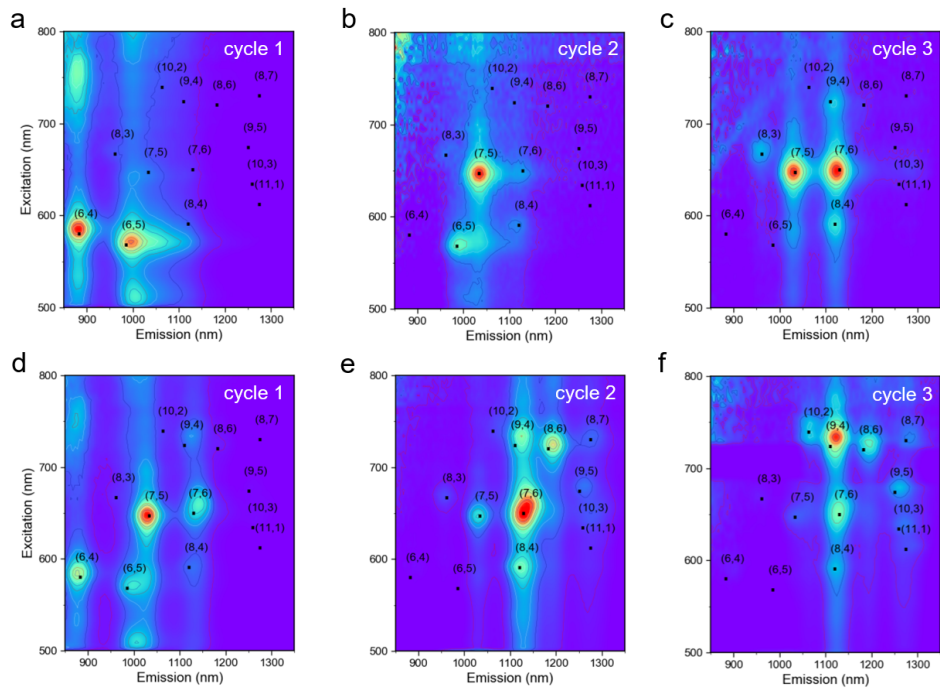
Figure 6.5: PLE maps of the chirality-sorted (a,b,c) unfilled and (d,e,f) HgTe-filled CHASM SWCNTs. Samples obtained in the first three cycles of sorting experiment were measured.
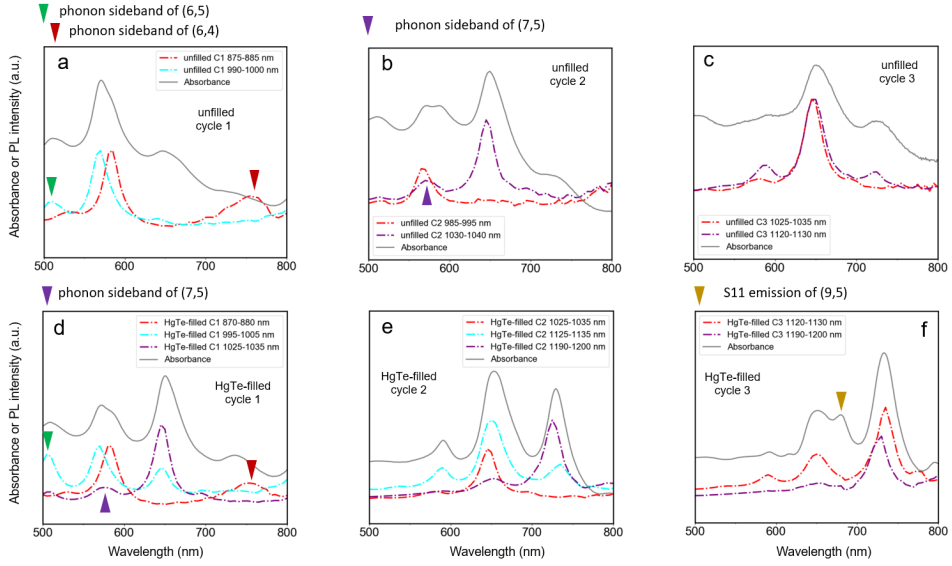
Figure 6.6: Absorption spectra and PLE profiles of CHASM SWCNTs obtained in the 1st-, 2nd- and 3rd-round of chromatography separation experiment

.

be assigned to a phonon sideband (**Figure 6.6a** and **d**). While phonon sidebands or vibrational modes can be easily seen on (n, m) species that have extremely small diameters, it is difficult to observe these features in the absorption or fluorescence spectra of wider-diameter (n, m) species. Apart from the photoluminescence features attributed to inter-band transitions and phonon sidebands, we detected no signals attributed to an EET process. For example, a shoulder feature lying at the higher excitation energy side of the emission maxima of (7,5) may possibly be induced by the EET from (6,4) or (6,5) to (7,5) SWCNTs (denoted in **Figure 6.6b** and **d**), but its wavelength deviated from those of the S_{22} transitions for (6,4) and (6,5). Therefore, this characteristic is likely to still be a phonon feature.

Since the origins of various emission peaks in the PLE maps can now be clarified according to the discussions and analyses above, we then proceed to investigate a change in the intensities of emission peaks associated with inter-band (S_{11}) transitions (refered to as I_{int} in the following contents) and phonon sidebands (refered to as I_{ph}) after NW filling. For the SWCNT fractions extracted in the 1st-round of chromatography experiment, an increase in the ratio of I_{ph}/I_{int} for (6,5) can be clearly seen after NW filling by comparing the PLE profiles shown in **Figure 6.6a** and **6.6d**. This raises the question of whether NW filling in (6,5) (which is likely to be linear atomic chain according to the electron microscopic characterizations in **Section 6.2**) enhances the electron-phonon coupling to give increased phonon side-

81

band emission or suppresses the fluorescence attributed to the inter-band transition.

Similar to the effect of SWCNT filling by zig-zag atomic NWs, which was discussed in the last chapter, it is expected that the linear atomic NW filling can also selectively enhance or suppress the SWCNT radiative recombination efficiency subjecting to their chirality or *mod* type. For (6,5) SWCNTs with a zig-zag HgTe NW filling, a slight increase in their fluorescence was discovered [75]. Filling by linear NWs, in contrast, is suspected to exert an opposite effect on the fluorescence of these SWCNTs due to a variation in the strain on nanotubes [160; 161; 162; 163; 84] or a change of the dielectric constant [164; 165; 166]. Therefore, the diminished photoluminescence from (6,5) SWCNTs shall be attributed to the result of a strong interaction between the nanotube and encapsulated nanowires, rather than their low abundance in the filled sample.

The (n, m) species with slightly larger diameters, such as (7,5) and (7,6), are not wide enough for 2×1 chain to present and the geometry of NWs inside them are therefore predicted to still be the one atom-thick linear chains. Comparing the wavelengths of interband fluorescence features of different (n, m) species from unfilled and HgTe-filled SWCNTs, it was discovered that (6,5), (7,5) and (7,6) displayed nearly no spectral shifting, a slight blue-shifting (towards shorter S_{11} wavelengths) and a substantial red-shifting (towards longer S_{22} and S_{11} wavelengths), respectively. Such a dependence of spectral shift on the *mod* type offers further evidence of a strain-induced effect.

The impact of atomic NW filling on the fluorescence efficiency of various (n, m) species is, so far, not fully understood. For zig-zag NW-filled (6,5) and (7,5), a slight enhancement of emission can be attributed to a reduced Auger recombination rate based on results from the transient absorption analysis [75]. However, for the (6,5) and (7,5) species in CHASM SWCNTs, filling with NWs resulted in a massively decreased fluorescence (**Figure 6.5d**). These discoveries suggest that the mechanism of NW filling altering the fluorescence efficiency of SWCNTs can be complicated and may depend on factors such as nanotube bundling or a change in the external dielectric environment due to a variation in the configuration of SDS micelle coating. For wider (n, m) species (*e.g.* (9,4), (10,6)) in CoMaCAT76 and CHASM SWCNTs, an increased fluorescence intensity and significant spectral red-shifting were discovered after the NW filling (**Figure 5.4** and **Figure 6.5**). This result implied that the optical properties of larger-diameter SWCNTs are relatively insensitive to the conformation of NWs (*i.e.* zig-zag and 2 atom-by-1 atom-thick chains).

PLE contour maps of the solution-state unfilled and HgTe-filled TUBALL
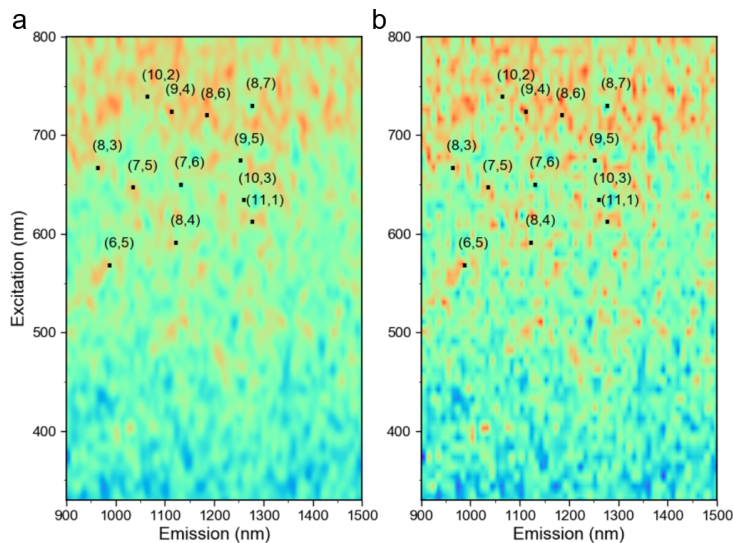
Figure 6.7: PLE maps of the solution-state (a) unfilled and (b) HgTe-filled TUBALL SWCNTs.

SWCNTs are shown in **Figure 6.7**, where almost no fluorescence from SWCNTs were detected. This is possibly due to the presence of thick nanotube bundles, which creates fast non-radiative relaxation pathways.

6.3 Raman spectroscopy of SWCNTs filled by different types of nanowires

The possible strain effect attributed to NW filling can also be examined based on the evolution of Raman features. The Raman spectra of as-centrifuged CHASM SWCNTs under an excitation wavelength of 785 nm is shown in **Figure 6.8**. The spectra at the G mode region consisted of 4 to 5 Lorentzian components. According to previous studies, G modes with an E_{2g} (or E_2 in case of chiral SWCNTs) symmetry at low (< 1580 cm^{-1}) and high (~ 1600 cm^{-1}) frequencies represent signatures of zigzag / near-zigzag and armchair / near-armchair SWCNTs, respectively [143]. For the G mode spectra of CHASM SWCNTs under 785 nm excitation, a E_{2g} mode shown at 1578-1579 cm^{-1} was found (**Figure 6.8b**). Jorio and colleagues determined the frequencies of G modes with different phonon mode symmetries and nanotube diameters according to Raman measurements on substrate-supported individualized SWCNTs [121], revealing that it can be described by the following expression:
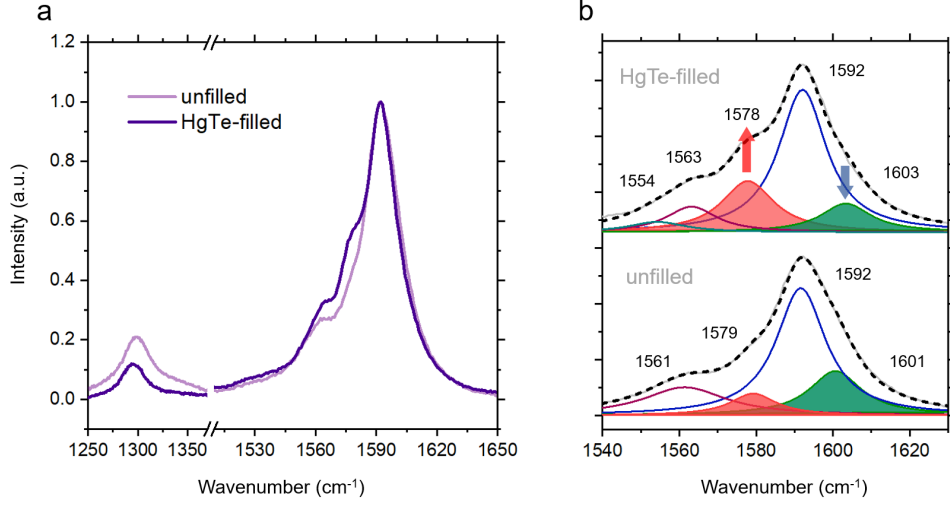
Figure 6.8: (a) Raman spectra of unfilled and HgTe-filled as-centrifuged CHASM SWCNTs in the D and G mode region. The spectra are background-subtracted and normalized to the maximum intensity of the G mode peak. The lower- and higher-frequency G mode components with a E_{2g} (E_2) symmetry are highlighted in red and green in panel (b). Red and blue arrows are added to denote an increase in the intensity of low-frequency mode whilst a decrease in the intensity of high-frequency mode due to filling.

$$\omega_G(cm^{-1}) = 1592(cm^{-1}) - 32.6(cm^{-1} \cdot nm^{1.4})/d_t(nm^{1.4}) \tag{6.1}$$

The estimated diameter of SWCNTs producing an E_{2g} mode at 1578-1579 cm^{-1} was then estimated to be ~1.8 nm, indicating that large-diameter SWCNTs were excited resonantly. According to the (n,m) composition revealed by the PLE maps, **Figure 6.4**, this E_{2g} component could be attributed to the feature of (10,2), (9,4), (8,6) or (8,7). Since Raman features of these large-diameter SWCNT species were detected by excitating in the near-infrared wavelength, it is possible to study the effect of the filling associated with 2×1 NWs.

Theoretical studies have demonstrated that a symmetric breaking due to the SWCNT deformation, *i.e.* stretching and bending, can lead to a change of electronic properties (*e.g.* opening of a small band gap in metallic SWCNTs [167; 168]). It was also shown the change of band gap with added axial strain is the largest for zigzag nanotubes and reduces with the increase of chiral angle. Armchair nanotubes, in contrast, show the largest change of their band gap under torsional strain. A decrease of this change occurs with a reduction in the chiral angle. The deformation of
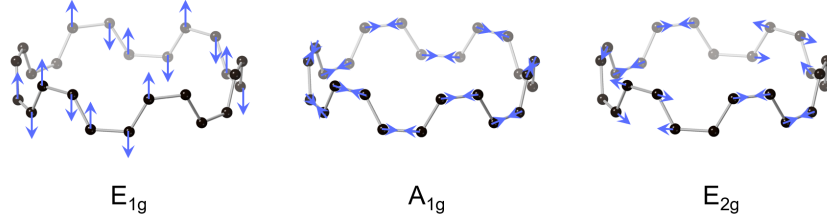
Figure 6.9: The atomic displacements of three Raman-active tangential modes of (6,6) tube [168].

nanotubes under strain results in certain changes in their Raman modes (especially the higher-frequency G mode), leading to a frequency shift (vibration mode hardening or softening, depending on weather tensile or torsional strain exists), intensity variation and splitting (symmetry breaking).

From the experimental Raman results, we indeed saw a change in the feature of G mode with a E_{2g} symmetry. It was discovered that NW filling induced a prominent enhancement in the intensity (comparing to the intensity of strongest $A_1 + E_1$ (G$^+$) mode at $\sim$1590 cm^{-1}) and a slight blue-shifting by $\sim$1 cm^{-1} of the lower-frequency E_{2g} mode (highlighted peak shaded red) whilst a noticeably suppressed intensity and a red-shifting by $\sim$3 cm^{-1} of the higher-frequency E_{2g} mode (green shading). Both theoretical and experimental studies revealed that molecular filling would only modify the strain in SWCNT radial direction [84; 163]. With asymmetric 2 atom-by-1 atom-thick NWs encapsulated, the large-diameter (n, m) are likely to distort and their cross-sections can be turned into ovals [77]. This, presumably, gives rise to additional anisotropic strain in the circumferential or radial direction. Since the E_{2g} vibration mode is the tangential with atomic displacement perpendicular to the tube axis (**Figure 6.9**), it is not a surprise that such a vibration mode would display a more prominent variation than the A_{1g} (perpendicular to the tube axis but has a symmetric atom displacement) and E_{1g} (parallel to the tube axis) modes due to nanotube distortion. The reason for an opposite change in the intensity of lower- and higher-frequency E_{2g} mode after HgTe filling might be due to a different strain effect of filling NWs on zigzag/near-zigzag and armchair/near-armchair (n, m).

Raman features of the unfilled and HgTe-filled TUBALL SWCNTs were also investigated. From the spectra of unfilled TUBALL SWCNTs, two prominent RBMs presented at 196.3 and 163.6 cm^{-1} were discovered under the 633 and 785 nm excitation, respectively (**Figure 6.10**). The faint features emerged at low frequencies (170 cm^{-1}) from the spectrum of HgTe-filled SWCNTs were possibly ascribed to

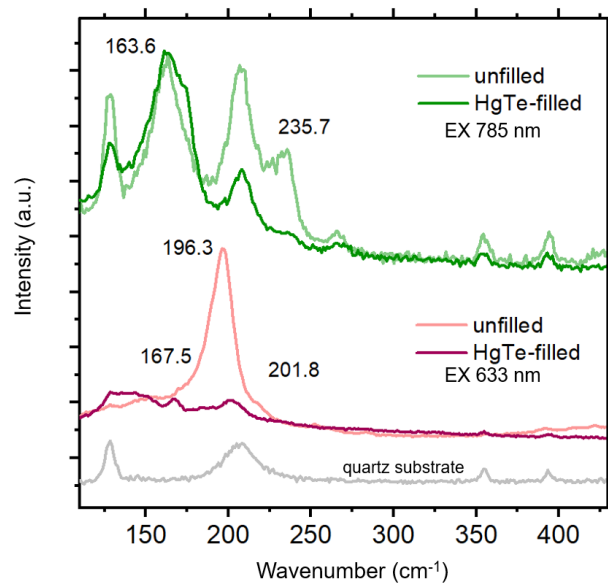Figure 6.10: Raman spectra of unfilled and HgTe-filled TUBALL SWCNTs in the RBM region. The grey curve is the spectrum of the quartz substrate without SWC-NTs lying on it. To directly compare the intensities of RBM peaks before and after NW filling, the spectra are background-subtracted and normalized to the intensity of the data point at $500\,\mathrm{cm}^{-1}$, where there is no feature related to carbon nanotubes or the substrate.
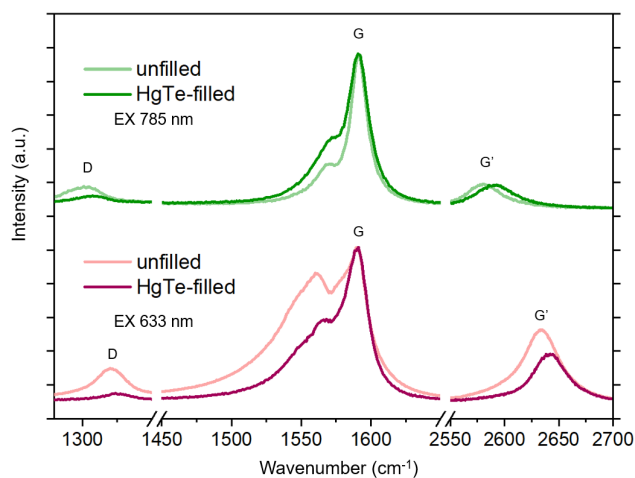
Figure 6.11: Raman spectra of unfilled and HgTe-filled TUBALL SWCNTs in the G and G' mode region. The spectra are background-subtracted and normalized to the maximum intensity of the G mode peak.

RBMs of wider nanotubes.

The corresponding spectra in the G and G' mode regions were found to display a large difference at different excitation wavelengths. Under the excitation wavelength of 633 nm, the displayed G mode consisted of a G^- branch that had a substantially high intensity, which features a BWF line shape, indicating that the metallic SWCNTs were excited resonantly (**Figure 6.11**). Under an excitation wavelength of 785 nm, the intensity of the G^- peak is reasonably low compared to that of the G^+ peak and is well separated from the D band (disorder mode), suggesting that the semiconducting SWCNTs were in resonance (**Figure 6.11**). In addition, the intensity ratio of G' to G mode $I_{G'} : I_G$ at 633 nm was significantly larger than that at 785 nm, providing additional evidence that the metallic SWCNTs were resonantly excited at a wavelength of 633 nm [169]. Based on these results, it was estimated that the TUBALL SWCNTs contained relatively narrower metallic species ($d_t \sim 1.2$ nm) and relatively wider semiconducting species (~ 1.45 nm). After filling by NWs, it was found that the RBM at 196.3 cm^{-1} was hugely suppressed and blue-shifted, whilst the peak at 163.6 cm^{-1} underwent a much smaller change. This suggested that NW filling can lead to a more prominent evolution of the Raman features for metallic nanotubes.

Ehli et al. investigated the spectroelectrochemistry of SWCNTs in the presence of strongly electron-accepting dye molecules [170]. It was shown that a reduction in the Raman mode intensity was attributed to a suppressed resonant enhancement effect due to the extraction of charges from nanotubes [170]. The observed

decrease in the RBM intensity after SWCNT filling is therefore assumed to be a result of HgTe NWs extracting electrons on the transition states of metallic TUBALL SWCNTs (*e.g.* excitonic and pseudogap states). Nevertheless, a more comprehensive investigation on such a charge transfer effect is hindered due to the polydispersive nature of thin film-state SWCNT samples. In this regard, characterizations on SWCNTs in an isolated state would need to be carried out in the future.

6.4 Modifying carrier dynamics by atomic nanowire filling

6.4.1 Free carrier property and conductivity of SWCNTs

The charge carrier properties of these SWCNT samples in the equilibrium and photoexcitation states were examined by time-domain THz (THz-TDS) and optical pump-THz probe (OPTP) spectroscopy. The features in the far-infrared spectral region ($\sim 0.3 - 2.5$ THz) were studied with a probe beam size of $\sigma \sim 0.5$ mm. At equilibrium state, under the thin-film approximation [171; 172] and assuming that the conductivity of the tested sample was much larger than the substrate, the complex conductivity of thin film medium can be linked to the transmission function by:

$$\sigma(\omega) = \frac{\epsilon_0 c(1 + \tilde{n}_S)}{d}(\frac{1}{T(\omega) - 1}) \qquad (6.2)$$

where ϵ_0 is the dielectric permitivity of free space (8.854×10^{-12} Fm^{-1}), c is the light speed in vacuum (2.998×10^8 m/s), $\tilde{n}_S$ is the complex frequency-dependent refractive index of substrate and d is the thickness of film.

The transmission of thin films in the equilibrium state (T_{off}) and photoexcited state (T_{on}) can be expressed as:

$$T_{off/on}(\omega) = \frac{2}{2 - i(n_{off/on}^2 + 1)\omega d/c} \qquad (6.3)$$

where $n_{off/on}$ is the refrective index of film at the equilibrium or photoexcited state.

The relative change of the time-domain THz electric field after photoexcitation can be obtained by:

$$\frac{\Delta E}{E} = \frac{E_{on} - E_{off}}{E_{off}} = \frac{T_{on} - T_{off}}{T_{off}} \tag{6.4}$$

With the thin-film approximation, the complex conductivity can be given as:

$$\Delta\sigma(\omega) = \frac{\delta \cdot \Delta E(\omega)}{E_{off}(\omega)} \cdot \frac{n_i + n_k}{Z_0} \tag{6.5}$$

where n_i and n_k are the refractive indices of mediums before and after the film sample. δ is film thickness. Z_0 is the impedance of free space and equals to 377 Ω.

Since the investigated SWCNT samples here are thin films deposited on quartz substrate, the mediums before and after SWCNTs should be air and quartz, respectively. Assuming that their frequency-dependent refractive indices were the same before and after photoexcitation, the conductivity change of the SWCNT film was dependent solely on the differential transmission $\Delta T/T_{off}$.

6.4.2 Theoretical models of conductivity

Physical parameters of SWCNTs such as carrier density and scattering rate can be extracted from the experimental conductivity spectrum by fitting with the theoretical models. A Drude-plasmon model that describes the movement of charges beyond and within the boundary of a nanoparticle is normally used to fit the experimental SWCNT conductivity spectrum, which can be expressed as [117]:

$$\sigma(\omega) = \sigma_D(\omega) + \sigma_p(\omega) \tag{6.6}$$

σ_D and σ_p are the Drude and surface plasmon conductivities.

In this model, the Drude conductivity is given as:

$$\sigma_D(\omega) = \frac{Ne^2}{m^*} \frac{i}{\omega + i\gamma_D} \tag{6.7}$$

where e is the electron charge (1.602×10^{-19} C), N and m^* are the density and effective mass of carriers, γ_D is the momentum scattering rate.

The surface plasmon conductivity is a modified Drude model with the introduction of a resonance:

$$\sigma_p(\omega) = \frac{Ne^2}{m^*} \frac{i\omega}{\omega^2 - \omega_p^2 + i\omega\gamma_p} \qquad (6.8)$$

where ω_p and γ_p are the plasmon resonant frequency and scattering rate.

6.4.3   Experimental results and discussion

Table 6.1: Fitting parameters for the Drude-plasma conductivity model

sample name	σ_D ($\Omega^{-1}cm^{-1}$)	γ_D (ps^{-1})	σ_p ($\Omega^{-1}cm^{-1}$)	γ_p (ps^{-1})	ω_p (THz)
unfilled	12 ± 0.3	40 ± 12	64 ± 1	90 ± 1.4	7 ± 0.1
HgTe-filled	18 ± 0.1	20 ± 1.5	42 ± 0.7	90 ± 1.2	7.5 ± 0.03

The time-domain THz spectra of the unfilled and HgTe-filled CHASM SWCNT films detected in the equilibrium state are shown in **Figure 6.12a**. The THz pulses passing through such two SWCNT films displayed a slightly different shift in time, which is due to the different phase shift caused by a variation in materials type and thickness. The frequency-domain transmission spectra of thin films converted from the time-domain spectra by Fourier transform were used to calculate complex conductivity based on **eq 6.2**, which were shown in **Figure 6.12b**. Experimental conductivity spectra were fitted based on the Drude-plasmon model ($\sigma(\omega) = \sigma_D(\omega) + \sigma_p(\omega)$). The extracted parameters were shown in **Table 6.1**. Here the error for each parameter represents the standard deviation calculated during the fitting.

It was found that filling by HgTe led to an increase in the ratio of Drude conductivity to plasmon conductivity (σ_D/σ_p) and a reduction of Drude scattering rate (σ_D), but had no significant change in parameters for surface plasmon model (*i.e.* plasmon scattering rate γ_p and plasmon resonance frequency ω_p). According to our analyses on zig-zag NW-filled SWCNTs in **Chapter 4**, the plasmon resonance frequency is dependent on SWCNT geometry such as nanotube length, bundle thickness and number of tubes in the bundle. A similar plasmon resonance frequency before and after HgTe filling indicates that the SWCNT structure and morphology
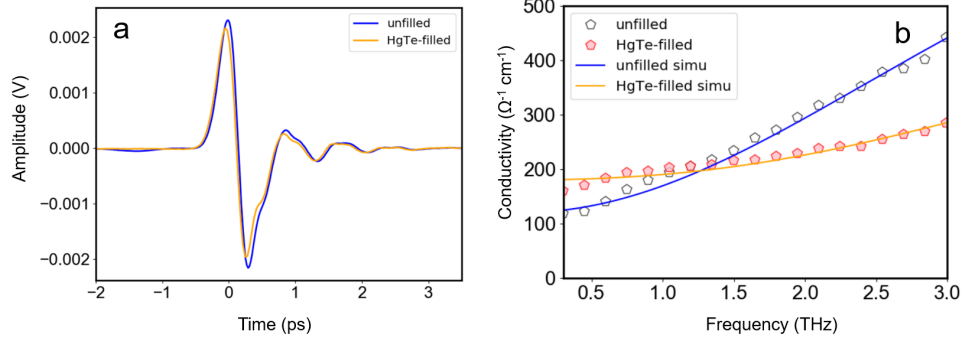
Figure 6.12: (a) Time-domain equilibrium THz spectra and (b) frequency-domain conductivity curves of the thin films of as-centrifuged unfilled and HgTe-filled CHASM SWCNTs deposited on the quartz substrate.
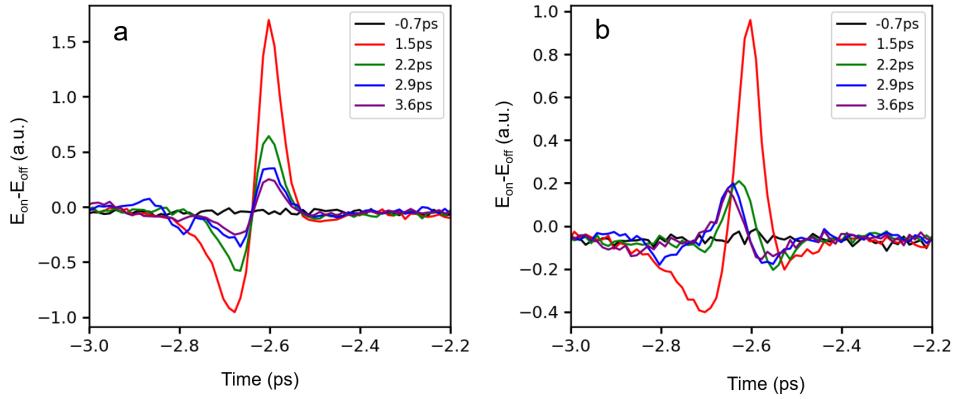
Figure 6.13: (a,b) Differential THz ($E_{on} - E_{off}$) waveforms of the thin films of as-centrifuged unfilled and HgTe-filled CHASM SWCNTs deposited on the quartz substrate.

in unfilled and filled thin films should be almost the same. We thus deduced that the increase in σ_D/σ_p was a result of higher concentration of free carriers in SWCNTs due to the doping effect. The decrease in γ_D indicated suppression of carrier scattering after HgTe filling.

The transient change of the time-domain THz spectrum and signal amplitude ($\Delta E/E$) for thin films of the unfilled SWCNTs and HgTe-filled CHASM SWCNTs, which are dominated by the linear chain and 2×1 chain structures, were shown in **Figure 6.13**. For the unfilled and HgTe-filled CHASM SWCNTs, the evolution of differential signal ($E_{on} - E_{off}$) with time delay was found to be significantly different. The time-dependent THz dynamics at the maximum signal amplitude of THz pulse is shown in **Figure 6.14a**. It can be seen clearly that the transient curves for unfilled and HgTe-filled SWCNTs displayed a negative and positive $\Delta E/E$, re-
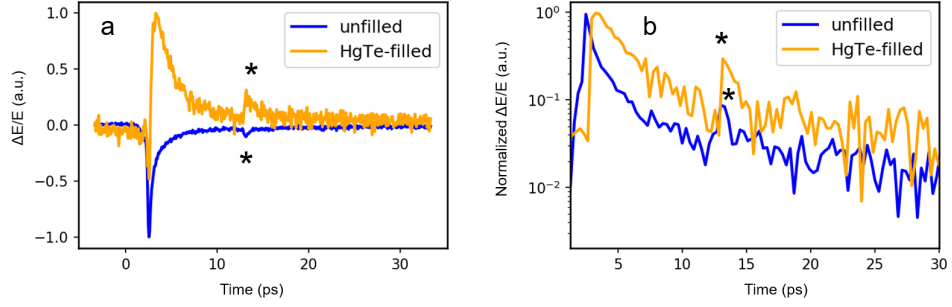
Figure 6.14: (a) Variation of differential signal amplitude with pump-probe delay for the thin films of as-centrifuged unfilled and HgTe-filled CHASM SWCNTs. (b) is drawn by flipping the trace of unfilled SWCNT film and plotting data in a semilog scale. The spikes denoted by asterisks are due to the reflection of pump beam on the back surface of the substrate, causing re-excitation of the sample.

spectively. By normalizing the transient curves and plotting in a semilog scale, it was found that the dynamics of HgTe-filled SWCNTs showed a slower decay rate (**Figure 6.14b**). Negative $\Delta E/E$, which is more commonly found in traditional semiconductor materials, indicates the generation of photoexcited charge carriers that can attenuate the transmitted THz field strength. Positive $\Delta E/E$ is less common and can be due to several reasons such as trion formation [116] or temperature effects [173]. Since the SWCNT sample applied for the study here are thin films consisting of thick bundles, such a positive $\Delta E/E$ may also arise from an enhanced intertube interaction as both metallic and semiconducting carbon nanotubes can exist within a bundle.

6.5 Questions addressed in this chapter and conclusions

In this chapter, the optical properties of carbon nanotubes in different ranges of diameter (0.7-1.4 nm for CHASM SWCNTs and ~1.6 nm for TUBALL SWCNTs) were studied. In the CHASM SWCNTs, the majority of nanowires are one atom-thick linear chain and two atom-by-one atom-thick (2×1) chain. Via SWCNT diameter refinement based on gel column chromatography, small-diameter (n, m) species (*e.g.* (6,5) and (7,5)) which were filled mainly by the one atom-thick linear chains were successfully extracted. For larger-diameter TUBALL SWCNTs, multiple atom-thick (n>2 along each direction in the lattice plane parallel to the nanowire cross section) nanowires were shown to be the major structure type.

Steady-state absorption and photoluminescence measurements were performed on CHASM SWCNTs. A substantial quenching of the fluorescence was observed on

the small-diameter (6,5) as a result of filling, indicating a potential strong interaction between the nanotube and atomic nanowire. Importantly, the fluorescence discovered here is in contrast with the results on SWCNTs filled by zig-zag nanowires, which implies a strong effect of the nanowire geometry on SWCNT optical performance. Raman measurements revealed a change in the G mode spectrum for these CHASM SWCNTs due to nanowire filling. A dependence of the spectral evolution on the chiral structure of nanotubes was demonstrated by comparing features of the near-zigzag and near-armchair SWCNTs. Due to the fact that the structures of encapsulated nanowires were highly refined and the chiralities of nanotubes are possible to be accurately assigned based on a range of spectroscopic characterizing methods, we have the opportunity to investigate explicitly the roles of nanowire geometry and nanotube structure within the 1D nanosystem. For investigations in the next step, we hope to expand our knowledge on the spectroscopic response of nanowire-filled nanotubes and especially the effect of changes in the structures of both nanotubes and the encapsulated nanowires on an atomic level. To investigate further the charge carrier properties, we carried out terahertz spectroscopic characterizations on CHASM SWCNT thin films. Based on results of time-domain terahertz spectroscopy (THz-TDS), it was found that HgTe nanowire filling can lead to an increased concentration of the free carriers, which was associated with the effect of doping. Using time-resolved terahertz spectroscopy (OPTP), it was revealed that the unfilled and HgTe-filled SWCNTs displayed a negative and a positive relative change in the electric field after photoexcitation ($\Delta E/E$), respectively. An unconventional positive $\Delta E/E$, which indicates a negative photoconductivity, may be explained by the formation of trions or a temperature effect. It is foreseen that the atomic nanowire-filled SWCNTs have a promise of applications in the ultrafast nanoelectronics, devices and terahertz modulators.

Spectroscopic properties of the large-diameter TUBALL SWCNTs were also primarily studied. Due to the difficulties of monodispersing and separating these SWCNTs, their optical features are not well resolved at the moment. To overcome this challenge, developing chemical protocols to more efficiently isolate these large-diameter nanotubes would be required in the future.

Chapter 7

Effect of Environment on the Spectroscopic Properties of SWCNTs

In this chapter I compare the properties of filled SWCNTs in different environments. The strain effect caused by nanowires encapsulation was revealed by temperature-dependent spectroscopic measurements. This study can help investigate unconventional interactions within 1D heterostructures. Part of the results in **Section 7.3**-**7.7** appear in the following publication: Ziyi Hu, Ben Breeze, Marc Walker, Eric Faulques, Jeremy Sloan, James Lloyd-Hughes Spectroscopic Insights into the Influence of Filling Carbon Nanotubes with Atomic Nanowires for Photophysical and Photochemical Applications. *ACS Applied Nano Materials* 2023, 6, 4, 2883–2893.

7.1   Evolution of the optical properties due to SWCNT bundling or a change of the suspending medium

The optical properties of SWCNTs are structure-sensitive. The spectral features and dynamics of SWCNTs were found to be dominated by various parameters, such as chirality, tube length and bundle size. Control of SWCNT bundling can be readily achieved through post-processing steps like capillary electrolysis [174], sonication [175] and density gradient centrifugation [176], which makes it a useful manner to study the effect of inter-tube interaction on the optical performance of SWCNTs and comprehensively understand the photophysics of these materials. Previous studies revealed that the SWCNT bundle size can influence the feature of generated inter-tube excitons [176] and relative intensity of fluorescence to Raman scattering

($I_\mathrm{PL}/I_\mathrm{RBM}$) [175]. Meanwhile, SWCNT bundling has been demonstrated to facilitate exciton energy transfer (EET) between the nanotubes, which can increase the dephasing rate and broaden the excitonic lines [87].

Apart from aqueous solutions, SWCNTs suspended in other types of mediums such as ice and polymer (*e.g.* gelatin) have also been studied [177; 178; 160]. Based on optical measurements, it was demonstrated that strain along the tube axis (known as uniaxial strain) can be modified by a change in the condition of surrounding medium, which then resulted in a shift in the excitonic energies of SWCNTs [177; 160]. An energy shift caused by a change in the uniaxial strain was found to be dependent on the SWCNT *mod* type [160; 161; 162], which is expressed as:

$$\Delta E_{ii} = (-1)^{i+1}(-1)^{k+1}3t_0(1+v)\epsilon\cos 3\theta \qquad (7.1)$$

where i is the transition order, $k = mod(n-m, 3)$ and t_0 is estimated to be $3\,\mathrm{eV}$. ϵ is the uniaxial strain. v is the Poisson ratio (~ 0.2). It is clear that ΔE_{11} and ΔE_{22} satisfy $\Delta E_{11} = -\Delta E_{22}$.

In previous studies it was reported that the infiltration of CNTs by molecules can expand the nanotube circumference, hence shifting the interband transition energy due to increased radial strain[163; 77; 84]. The energy shift with radial strain σ varies with chiral angle θ according to [179] (the same to **eq 2.13** introduced in **Chapter 1**):

$$\Delta E_{ii} = (-1)^{i+1}(-1)^{k+1}3t_0\sigma\sin 3\theta \qquad (7.2)$$

where k is the *mod* index and σ is the radial strain. With this prediction, a strong *mod* family type dependence of the energy shift would be expected. In our characterizations, a dependence of filling-induced ΔE_{ii} on the *mod* index can be clearly seen from the solution-state SWCNTs [75], with a generally larger ΔE_{ii} being observed on the type 1 SWCNTs such as (7,5) and (10,2) than on the type 2 SWCNTs such as (8,4) and (6,5).

In this chapter, properties of HgTe-filled SWCNTs in different existing states (*i.e.* isolated in solution, suspended in gelatin matrix, bundled within a thin film network) were characterized. Results showed that HgTe NW filling can modify the vibrational frequencies along both in-plane (tangential) and radial directions. The effect of HgTe filling on the optical dynamics of SWCNTs in these different states

was also investigated.

7.2 Preparation of SWCNT samples in different environment

For the experiments conducted in this chapter, we examined SWCNTs in three different morphologies, which include the solution-state SWCNTs (nanotubes dispersed in the SDS aqueous solution), the gelatin-embedded SWCNTs (nanotubes embedded in the gelatin thin film) and SWCNT thin film network (nanotube film fabricated by vacuum filtration). Here, the semiconducting CoMoCAT76 SWCNT solutions which had been studied in **Chapter 5** were used as the solution-state SWCNT samples.

To fabricate gelatin-embedded SWCNT films, a mixture containing SWCNTs, gelatin and water was first prepared. This was achieved by dissolving gelatin in DI water (where a mass ratio of $m_{gelatin} : m_{water} = 1 : 10$ was applied) and then adding this gelatin solution into the semiconducting CoMoCAT76 SWCNT solution (where a mass ratio of $m_{gelatin\,solution} : m_{SWCNT\,solution} = 11 : 2$ was applied). The final mixture was dropcasted on the quartz substrate and left to dry at room temperature for 12 h. The thicknesses of final dried films were $\sim 0.1 - 0.2$ mm.

SWCNT networks with a large degree of bundling were fabricated based on a vacuum filtration approach, which had been detailed in **Section 4.6** (see **Figure 4.17** and related description in the text). The thickness of final dried films was typically ~ 75 nm (**Figure 7.1**). Experimental procedures to prepare the above two types of thin film-state SWCNT samples based on solution-state SWCNTs are described in **Figure 7.2**.

7.3 Steady-state spectroscopic properties of SWCNTs

Excitonic transition features of SWCNTs in different existing states were studied by steady-state absorption spectroscopic measurements. The UV-Vis-NIR spectra of SWCNT samples in different environments (vacuum-filtered thin-film, solution state, and gelatin film) with and without HgTe infiltration are shown in **Figure 7.3**. HgTe infiltrated samples (solid purple lines) had similar absorption spectra to unfilled samples (blue dashed lines), while the morphology of the nanotubes created more significant changes. The excitonic absorption lines of thin film-state SWCNTs (top) were markedly red-shifted and broadened as compared to those of isolated solution-state (middle) and gelatin-embedded (bottom) samples. The sig-
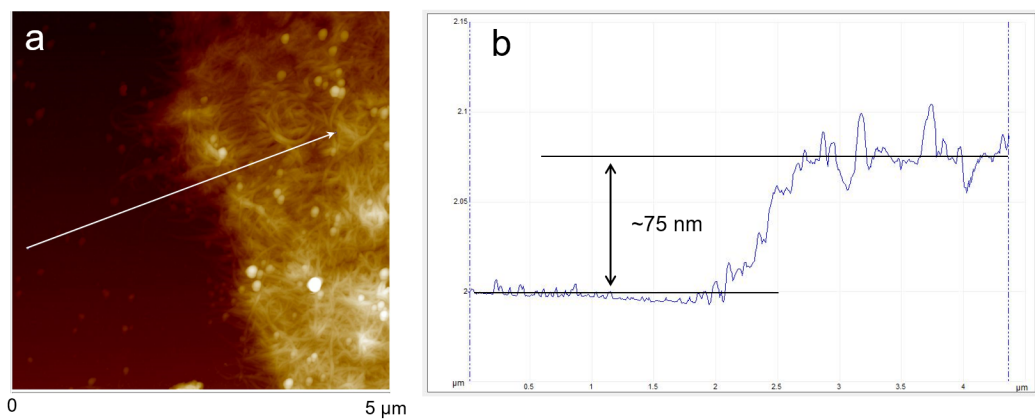
Figure 7.1: (a) AFM height measurement near the edge of a filtrated SWCNT thin film. (b) Cross-section profile along the line indicated by the white arrowed line in panel (a). The estimated thickness of the film is ~ 75 nm.
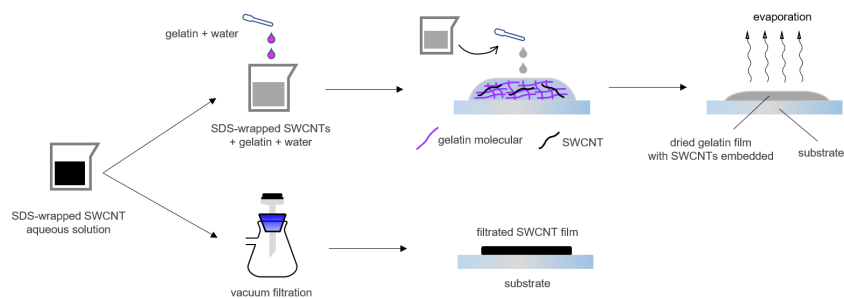

Figure 7.2: Schematic diagram illustrating the experimental procedures to prepare the gelatin-embedded SWCNT film and vacuum-filtrated SWCNT film. The vacuum filtration experiment had been described in **Section 4.6**.
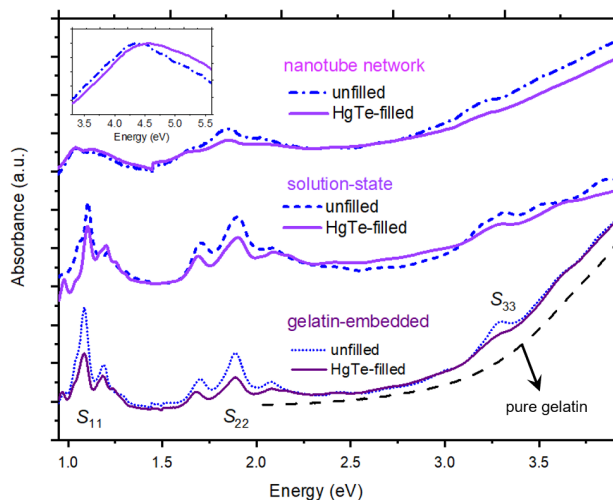
Figure 7.3: UV-Vis-NIR absorption spectra of SWCNT samples in different states. The dashed curve is the rescaled absorption spectrum of blank gelatin film. The inset shows the absorption spectra of the vacuum-filtered thin films at higher energies, which revealed the π-plasma feature.

nificant nanotube bundling of SWCNTs within the vacuum-filtered film results in the strongly modified excitonic properties, such as band renormalization, which can be interpreted by a change in the electronic dispersion due to inter-tube interaction within the bundle [180], different dielectric environment, altering the excitonic energies, while ultrafast tube-tube energy transfer within bundles increases the dephasing rate [7], broadening the excitonic lines (most clearly seen for the S_{11} and S_{22} peaks). Stronger UV absorption in the gelatin-embedded samples arose from the gelatin matrix (long-dashed line).

To analyze further, the linewidths of these oscillators before and after HgTe filling were analyzed by fitting the experimental absorption spectra with Gaussian functions. For solution-state SWCNTs, nearly all SWCNT oscillators showed an increased linewidth (**Figure 7.4**). For gelatin-embedded SWCNT samples, in contrast, only components for medium-sized (n, m) species such as (7,6) and (8,4) showed an increase in linewidth, whilst those for smaller- or larger-size species such as (7,5) and (9,5)/(10,3) displayed the opposite trend (**Figure 7.5**). A consistent change in the linewidth of exciton transition peaks observed on various (n, m) species in the solution may possibly attributed to an increased heterogeneity of the internal environment with the presence of nanowire filling, as had been demonstrated on water-filled SWCNTs in a study elsewhere [85]. For SWCNTs embedded in the gelatin matrix, a small degree of nanotube bundling is expected to occur due to
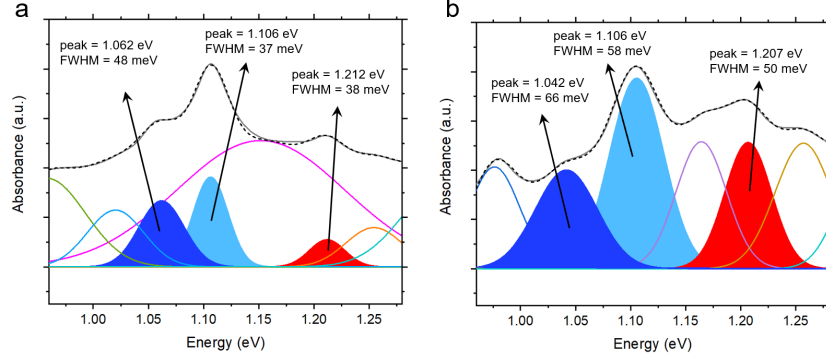
Figure 7.4: Absorption spectra of the solution-state (a) unfilled and (b) HgTe-filled SWCNTs at the S_{11} regime and fits based on Gaussian functions. The figures in black, white/grey and yellow are the center frequencies (in eV) and FWHM (in meV) of different Gaussian components. The components highlighted in red, light blue and darker blue are assigned to S_{11} excitonic transitions of (7,5), (7,6)/(8,4) and (8,6), respectively.

a loss of solvent upon sample preparation. As well as that, a change of the suspension medium can probably also result in the reorganization and coverage of the surfactant micelle shell surrounding the SWCNTs due to the difference in miscibility [181], which results in an altered environment outside of SWCNTs. Therefore, it is deduced that the change of linewidth in different ways for SWCNTs in the gelatin film is driven by a complicated mechanism, in which both the fluctuations of internal environment due to nanowire filling and external environment due to nanotube bundling or surfactant molecular reorganization could play a role.

We then studied the conductivity of vacuum-filtered SWCNT films by characterizing their far-infrared transmittance via terahertz time-domain spectroscopy (THz-TDS). The experimental transmittance was converted into the ac conductivity, the real part of which is shown in **Figure 7.6** (points), based on the thin-film approximation [182]. The conductivity for both unfilled and HgTe-filled SWCNT films increased toward higher frequencies. Spectra were simulated by the axial plasmon model for a number of different plasmon frequencies, corresponding to different SWCNT lengths or bundle number,[117] creating the solid curves in **Figure 7.6**. The model was expressed as follows:

$$\sigma(\omega) = \sum_{j=1}^{n} \frac{i \cdot \sigma_{p,j} \cdot \omega \cdot \gamma_{p,j}}{\omega^2 - \omega_{p,j}^2 + i \cdot \omega \gamma_{p,j}} \tag{7.3}$$

where $\omega_{p,j}$ is the plasmon resonance frequency, $\sigma_{p,j}$ is the plasmon conductivity at
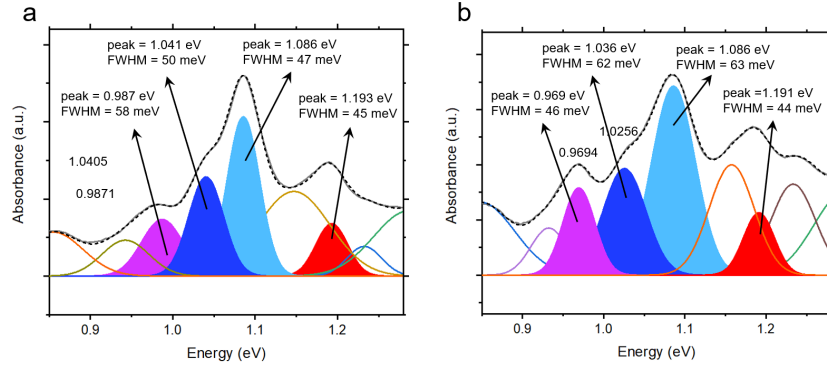
Figure 7.5: Absorption spectra of the gelatin-embedded (a) unfilled and (b) HgTe-filled SWCNTs at the S_{11} regime and fits based on Gaussian functions. The figures in black, white/grey and yellow are the center frequencies (in eV) and FWHM (in meV) of different Gaussian components. The components highlighted in red, light blue, darker blue and magento are assigned to S_{11} excitonic transitions of (7,5), (7,6)/(8,4), (8,6) and larger-diameter (n, m) species (*e.g.* (9,5), (10,3)), respectively.

the resonance frequency $(\omega = \omega_{p,j})$, and $\gamma_{p,j}$ is the plasmon scattering rate for each of the n oscillators. A small number of plasmon oscillators can model the physical situation, which has a continuous distribution of SWCNT bundle lengths.

The fit results show the existence of a strong plasmon oscillator located at a relatively high frequency. The plasmon resonance frequencies (7-9 THz) according to the fits are very similar to those determined from the FTIR spectra (8-9 THz) (**Figure 5.14**). HgTe filling resulted in both a broadening (damping rate increased from 70 to 90 ps^{-1} from unfilled to filled) and blue-shifting (central frequency increased from 7 to 9 THz) of the plasmon resonance peak. The additional extra conductivity in the spectrum of HgTe-filled SWCNT film from 0.5 THz to 2.0 THz is modelled by additional plasmon resonances at 1.1 THz and 2.4 THz. The small extra optical conductivity of the NW-filled SWCNT composite may imply a weak doping of the SWCNTs after infiltration, or it may result from subtle differences in film morphology in comparison to the reference film. We return to discuss electronic doping later in the manuscript.

7.4 X-ray photoelectron spectroscopy of SWCNTs

XPS Hg 4f, Te 3d and C 1s core-level spectra of filtrated film-state SWCNTs are shown in **Figure 7.7**. In crystals or alloyed compounds containing tellurium, the stoichiometry and chemical state depend heavily on reactions with the external environment [183; 184; 185]. Te element can therefore be in forms of Te(2-), Te(0)
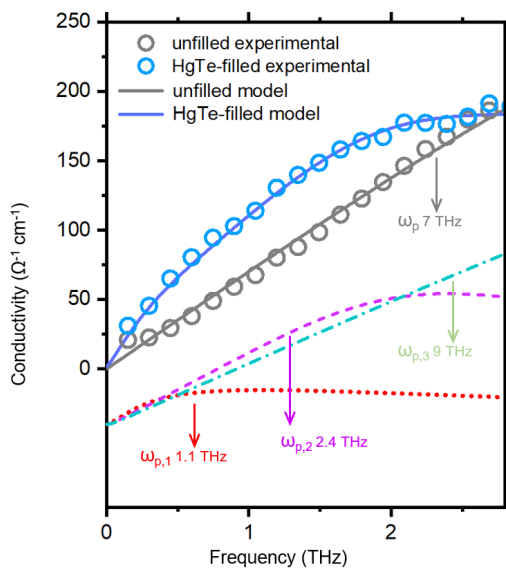
Figure 7.6: Absolute alternative-current conductivity of vacuum-filtered SWCNT films and simulated values based on the surface plasmon model. The experimental conductivity was converted from the far-infrared transmittance of samples measured based on THz-TDS. Dotted, dashed and dot-dash curves shown at the bottom of figure are the three plasma oscillators contributing to the simulated conductivity spectrum of HgTe-filled SWCNT film (blue solid curve). Plasma resonance frequency for each oscillator is denoted in the figure.
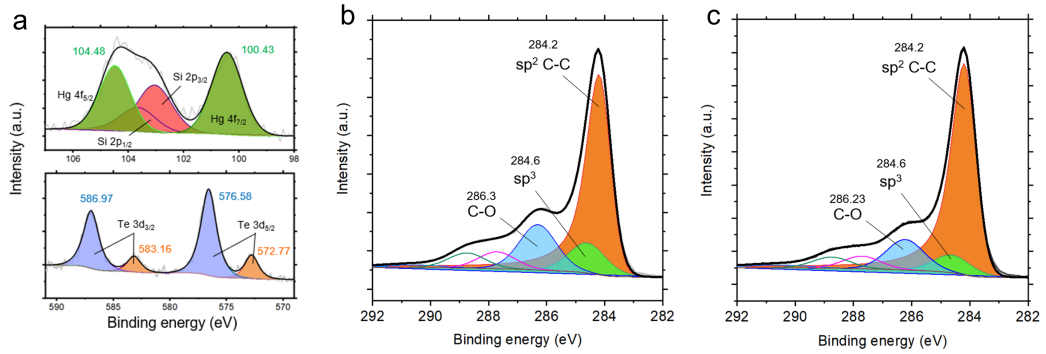
Figure 7.7: XPS spectra of the vacuum-filtered HgTe-filled semiconducting SWCNT thin films: (a) Hg 4f (top) and Te 3d (bottom) level spectra of HgTe-filled SWCNTs, (b,c) C 1s level spectra (b for unfilled SWCNTs and c for HgTe-filled SWCNTs).

and Te(4+). On the basis of their binding energy separation we assigned the Te peaks to a stronger Te(4+) component and a weaker contribution from Te(0)/Te(2-) [183; 185]. In the Hg 4f core level spectrum, two peaks related to Hg were assigned to the split $4f_{7/2}$ and $4f_{5/2}$ levels (**Figure 7.7a**). The position and shape of the Hg $4f_{7/2}$ peak allows the Hg(2+) or Hg(0) valence states to be distinguished [186; 187]. Here, the Hg $4f_{7/2}$ peak can be fit by a single Gaussian peak with a central binding energy 100.43 eV, suggesting that Hg(2+) ions were detected by XPS. Via charge balance the Te element in HgTe NWs would then be Te(2-). The assignment of this smaller doublet in the Te 4f region is further corroborated by the composition ratio between the total Hg 4f intensity and the smaller doublet of the Te 4f region of 1:1.06. We suggest that the prominent Te(4+) feature results from residual surface oxides on extraneous material grown outside the nanotubes, such as $Te^{4+}O_4^{2-}$. The Si 2p signal, which partially overlaps the Hg 4f signal, originates from the carbon tape used to secure the sample. To sum up, we confirmed that the filling material underwent nearly no depletion after the synthesis experiment, which was in good agreement with the result of EDX analysis above (**Figure 4.14**).

Comparing the C 1s spectrum of HgTe-filled SWCNTs (**Figure 7.7c**) to that of unfilled SWCNTs (**b**), it is shown that there was nearly no spectral shift of the sp^2 peak, which differs from a prominent change observed in previous studies as a result of nanocrystal formation inside carbon nanotubes [14; 76; 188]. These observed results link to a little substantial doping created by the HgTe NWs.
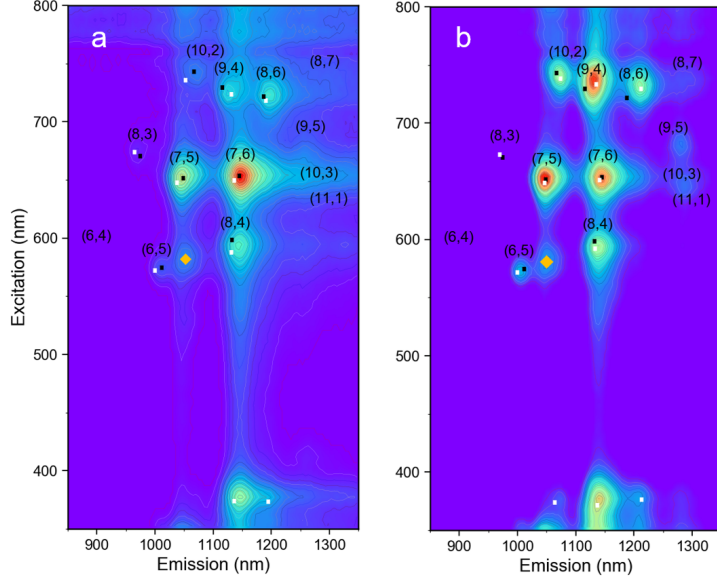
Figure 7.8: Room-temperature PLE contour maps of the (a) unfilled and (b) HgTe-filled SWCNTs embedded in the gelatin film. Black and white dots are the interband energy values obtained based on the model described in **eq 7.4** and the experimental energy values of these SWCNTs in a solution state. The orange diamonds are an assigned phonon sideband feature of (7,5).

7.5 Temperature-depended photoluminescence of SWC-NTs

The photoluminescence properties of SWCNTs at different temperatures were then studied. Due to the phase change of solvent at low temperatures, characterizing solution-state SWCNTs would be challenging. As a result, gelatin films containing suspended SWCNTs were used for the tests.

Here the photoluminescence of SWCNTs in gelatin films at the liquid-nitrogen temperature (~ 80 K) was characterized and compared to that at room temperature. Photoluminescence-excitation maps of unfilled and HgTe-filled SWCNTs in the gelatin film at these two temperatures are shown in **Figure 7.8**, **7.9** and **7.10**, where emissions originating from different (n, m) were discovered.

Theoretical interband transition energies of the first- and second-order transitions (S_{11} and S_{22}) were calculated based on the model introduced by a previous study [189]:

$$E_{ii} = a \left[\frac{p}{d_t} + b \frac{p}{d_t} \log \frac{c}{p/d_t} \right] + \frac{\beta_p}{d_t^2} \cos 3\theta + \frac{\gamma}{d_t} \tag{7.4}$$

103

Figure 7.9: PLE contour maps of the unfilled SWCNTs embedded in the gelatin film measured at (a) 298 K and (b) 80 K. Arrows indicate the orientation of interband energy shift. The diagonal lines presenting at upper right of the contours were induced by the Rayleigh scattering.
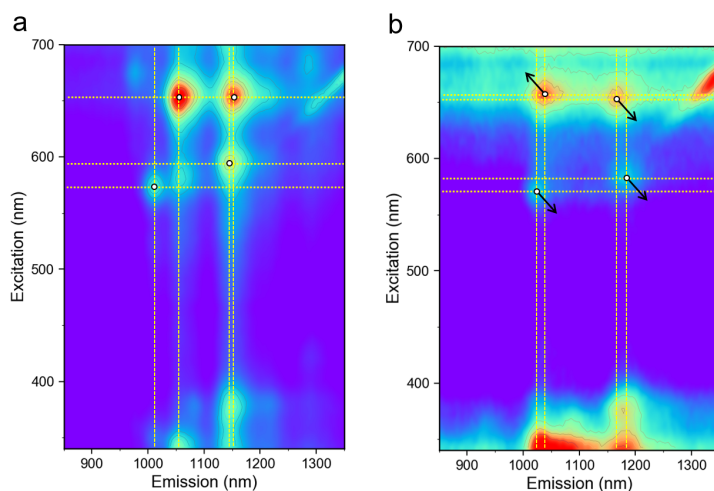
Figure 7.10: PLE contour maps of the HgTe-filled SWCNTs embedded in the gelatin film measured at (a) 298 K and (b) 80 K. Arrows indicate the orientation of interband energy shift. The diagonal lines presenting at upper right of the contours were induced by the Rayleigh scattering.
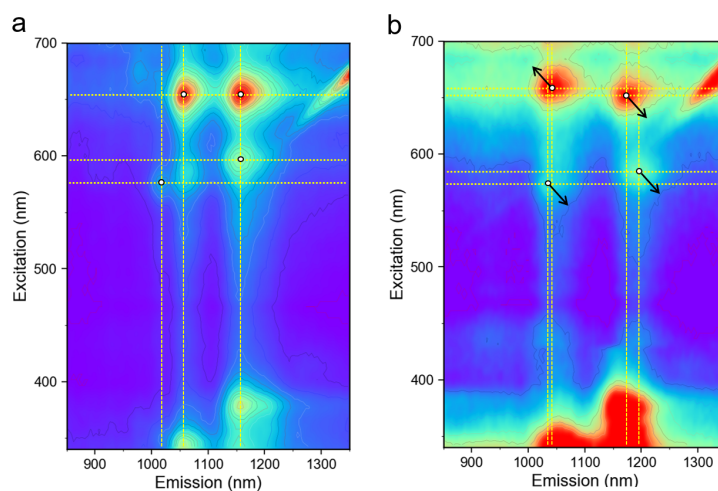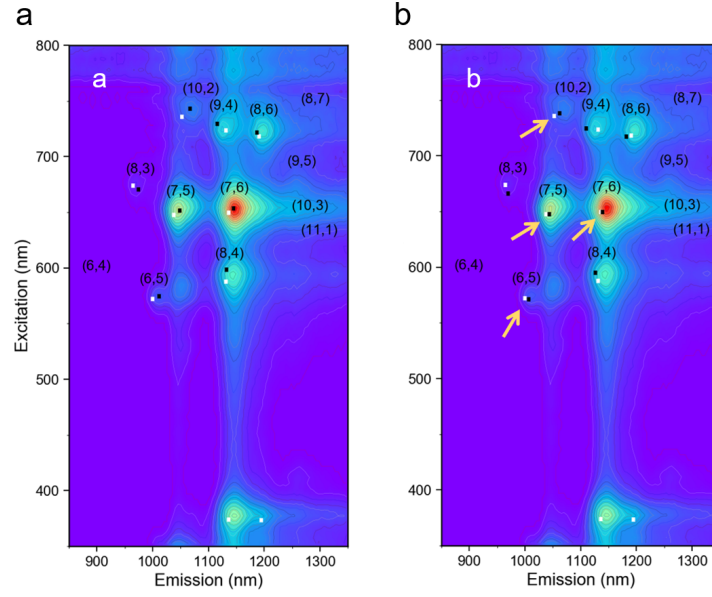
Figure 7.11: PLE contour maps of the unfilled SWCNTs embedded in the gelatin film with black dots showing the E_{ii} energies calculated based on different values of c parameters: (a) 0.795 nm^{-1} and (b) 0.814 nm^{-1}. White dots represent E_{ii} of the corresponding SWCNTs in solution.

where $p = 1, 2$ depending on the transition order and a, b and c are all constants. d_t and θ are the diameter and chiral angle of SWCNT. In the model, the quantum confinement of the 2D electronic structure of graphene is represented by a linear relationship of E_{ii} with p/d_t; the logarithmic term and chiral angle-dependent term are included to take into account the many-body effect and correct for a variation of SWCNT chirality; the γ/d_t term links to the exciton binding energy. We found that the first- and second-order experimental transition energies for most (n, m) species in the gelatin-embedded SWCNTs can be simulated using parameters $a = 1.049$ eV, $b = 0.456$ nm, $c = 0.795$ nm^{-1}, $\beta_1 = 0.05$ nm^2 (mod$(n - m) = 1$)/-0.07 nm^2 (mod$((n - m) = 2)$), $\beta_2 = $ -0.19 $(mod = 1)$/0.14 $(mod = 2)$ and $\gamma = 0.305$ eV (**Figure 7.8**). By increasing the constant value of log term c from 0.795 nm^{-1} to 0.814 nm^{-1}, the recalculated energies for these small-diameter (n, m) (*e.g.* (6,5), (7,5), (7,6) and (10,2)) were found closer to the experimental energies of those in a solution state (**Figure 7.11**), indicating that gelatin matrix encapsulation can potentially modify the many-body interaction within the SWCNTs.

The difference between the experimentally determined E_{ii} of solution-state and gelatin-embedded SWCNT samples, $\Delta E_{ii} = E_{ii,\text{gelatin}} - E_{ii,\text{solution}}$, is shown in **Figure 7.12**. For the unfilled SWCNTs (dashed lines) both S_{11} and S_{22} are at
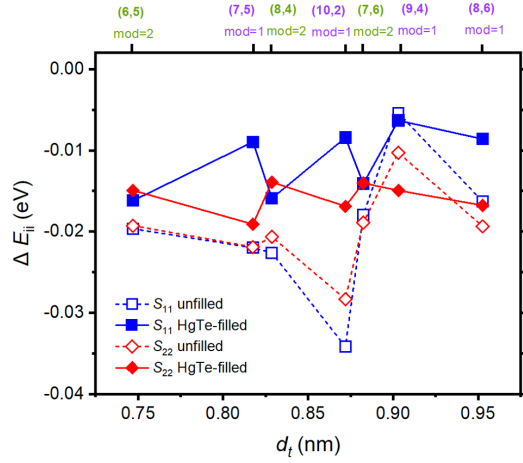
Figure 7.12: Excitonic energy shifts of various (n, m) species as a result of change in the surrounding medium, $\Delta E_{\mathrm{ii}} = E_{\mathrm{ii, \, solution}}$ - $E_{\mathrm{ii, \, gelatin}}$.

lower energies in solution than in gelatin ($\Delta E_{ii} \simeq -20 \, \mathrm{meV}$) as a result of the gelatin matrix changing the many-body interactions, whereas for the filled SWCNTS (solid lines) $\Delta E_{ii} \simeq -10 \, \mathrm{meV}$. Interestingly, for the HgTe-filled SWCNTs, ΔE_{11} displays an observable dependence on the CNT family, with the mod 1 family having a smaller ΔE_{11} than for mod 2 SWCNTs. Thus, when filled, changing the outer dielectric environment alters the excitonic energies in a way that depends on the CNT family. To investigate further, ΔE_{11} was plotted against nanotube diameter d_t (**Figure 7.12**) and against $\cos 3\theta$ and $\sin 3\theta$ (**Figure 7.13**), where θ is the chiral angle of SWCNT. No clear dependence of ΔE_{ii} on d_t or θ was discernible, suggesting that multiple parameters in **eq 7.4** are altered simultaneously.

We now propose a physical mechanism by which the optical properties of SWCNTs depend on the environment. In an SDS solution a SWCNT is believed to have an outer micellar coating with a configuration depending on various factors, such as SWCNT chirality or metallicity [59; 61], the pH of the medium [190] and the length of SWCNTs [63]. Presumably, immobilizing the micelle-coated SWCNTs in a gelatin matrix can result in a change in the configuration of surfactant coatings by, for example, replacing SDS at the surface with gelatin molecules. This can modify the local dielectric constant felt by charges in the SWCNTs and lead to a change in their excitonic and optical properties.

The experimental E_{ii} energies determined from the room-temperature PLE map of gelatin-embedded SWCNT samples were compared with those in solutions, based on E_{ii} energies determined from **Figure 5.4**. It was found that shifts in the first-order exciton energies (ΔS_{11}) for different (n, m) species due to a change

106
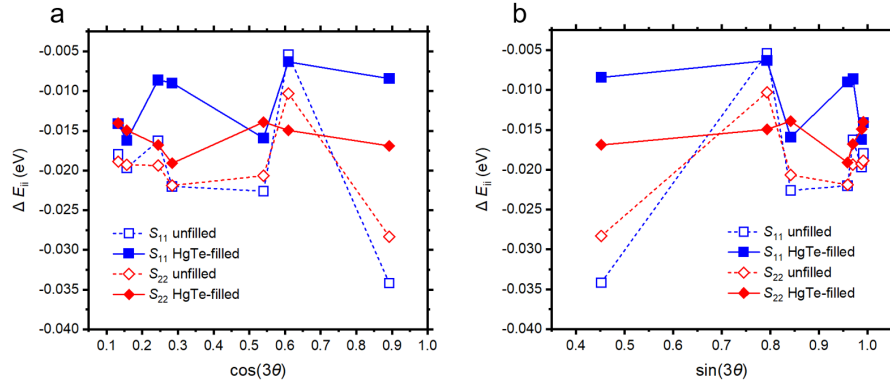
Figure 7.13: Energy difference (ΔE_{ii}) between the solution-state and gelatin-embedding (n, m) species determined from the PLE contour map. The ΔE_{ii} was plotted against (a) $cos(3\theta)$ and (b) $sin(3\theta)$, where θ is the chiral angle of (n, m).
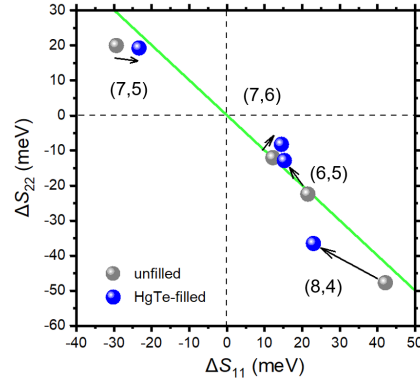
Figure 7.14: Excitonic energy shifts induced by a change in the temperature, ΔE_{ii} = $E_{ii, 80\ K}$ - $E_{ii, 298\ K}$.

of encapsulating medium displayed an observable *mod* family dependence (**Figure 7.12**). The temperature-induced E_{ii} shifts ($\Delta E_{ii} = E_{ii,80\ K}$ - $E_{ii,298\ K}$) of four different (n, m) species in the gelatin-embedded film samples were shown in **Figure 7.14**. Taking into account a significant difference in the thermal expansion constant between SWCNT and gelatin matrix, the observed energy shift upon cooling can arise from a change in the uniaxial strain on SWCNTs. Based on the relation between ΔE_{ii} and strain described in **eq 7.1**, the shifts of 1st- and 2nd-order excitonic energies should obey the rule $\Delta S_{11} = \Delta S_{22}$. We indeed observed such a trend for different (n, m) species (**Figure 7.14**). A reduction in ΔS_{ii} was found for (6,5), (7,5) and (8,4) SWCNTs after filling with nanowires, suggesting that the filling may result in a decreased uniaxial strain constant for these (n, m) species.

7.6 Temperature-dependent Raman measurement on SWC-NTs

The Raman features of filtrated SWCNT thin films at various temperatures (room temperature to 400 °C) were measured to analyze temperature-induced changes. To conduct the measurement, the thin film sample was placed in a Linkam stage (THMS600) which was purged with nitrogen in prior to temperature rising. The Raman signals were measured firstly at room temperature and then from 100 °C to 400 °C at a ramping rate of 40 °C/min. Spectrum was acquired 2 min after the temperature reached the set value. The issue of sample moving and defocusing during heating can be neglected as the Raman spectra were normalized to their background signal intensities afterward. The temperature-dependent Raman spectra of SWCNT films under two different excitation wavelengths (660 and 532 nm) were shown in **Figure 7.15** and **7.16**.

Most of Raman modes were found to display a decreased intensity, increased linewidth broadening, and lower Raman shifts with a rise in temperature. Such a spectral evolution at higher temperatures has been reported in a previous work where both semiconducting and metallic SWCNTs were investigated [191] and can be attributed to the faster dephasing of the excitonic state at elevated temperatures.

Under 660 nm excitation and 532 nm excitation, a notable reduction in the temperature coefficients after HgTe filling was found for the RBM modes (**Figure 7.17a** and **7.17b**). The temperature coefficients for the G^+ and G^- modes also reduced after filling under 660 nm and 532 nm excitation, except for the G^+ band for 532 nm excitation which appeared unaffected. For SWCNTs forming into thick bundles, as in the thin-film morphology in this Raman study, an increased temperature is thought to weaken both the intratube bonds and the intertube van der Waals forces, redshifting the RBMs and G modes, whereas thermal expansion in the radial direction contributes less than 10 % of the redshift [192]. Hence one hypothesis consistent with the above experimental results is that while HgTe NW filling may marginally increase the diameter of the SWCNT, accounting for the lower RBM frequencies after filling, the lower temperature coefficient may result from modified force constants for the intratube or intertube bonds [192].
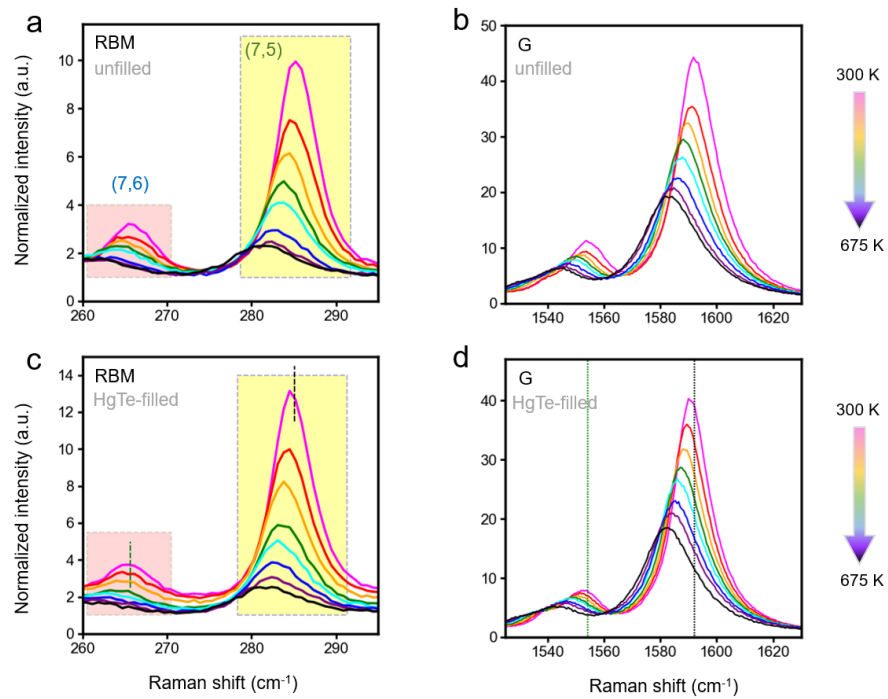
Figure 7.15: Temperature-dependent Raman spectra of the vacuum-filtered thin film of unfilled SWCNTs in the (a,c) RBM and (b,d) G mode regions under an excitation wavelength of 660 nm. The spectra are background-subtracted and normalized to the intensity of data point at 500 cm^{-1}, where there is no feature related to carbon nanotubes or the substrate. The dashed vertical lines in panel (c) and (d) mark the central frequencies of room-temperature RBM peaks for the corresponding unfilled SWCNT samples.
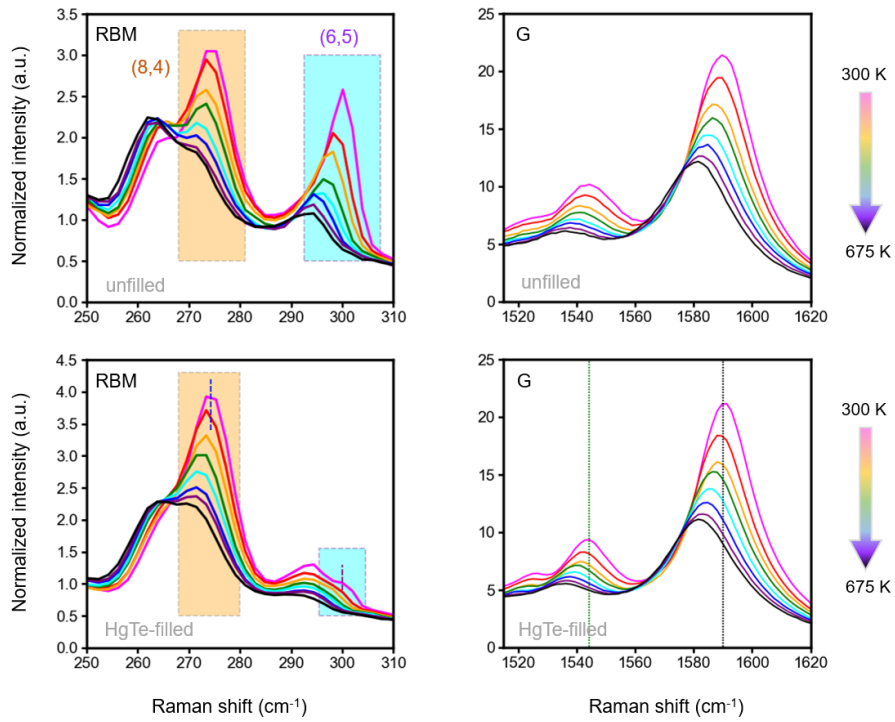
Figure 7.16: Temperature-dependent Raman spectra of the vacuum-filtered thin film of HgTe-filled SWCNTs in the (a,c) RBM and (b,d) G mode regions under an excitation wavelength of 532 nm. The spectra are background-subtracted and normalized to the intensity of data point at 500 cm^{-1}, where there is no feature related to carbon nanotubes or the substrate. The dashed vertical lines in panel (c) and (d) mark the central frequencies of room-temperature RBM peaks for the corresponding unfilled SWCNT samples.
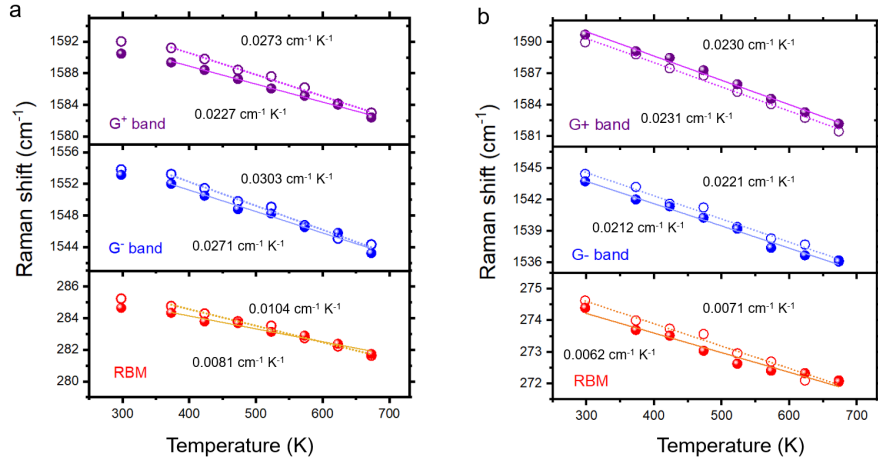
Figure 7.17: (a,b) Changes in the Raman shifts of different Raman modes for the unfilled (open circles) and HgTe-filled (filled circles) SWCNT film samples against temperature under 660 nm (a) and 532 nm (b) excitation. The dotted and solid straight lines are linear fits to the data points. Gradient for each fit is given in the graph.

7.7 Transient dynamics of SWCNTs in different environment

We then studied the transient absorption features of SWCNTs in aqueous solutions and gelatin matrices, where nanotubes are expected to have a similar dispersivity but quite a different interaction with the surrounding environment. To enable different electronic pathways in SWCNTs to be probed, a substantially high pump fluence of 17 mJ cm^{-2} pulse^{-1} was applied.

The TA spectra of unfilled and HgTe-filled SWCNTs measured at a pump wavelength of 625 nm were shown in **Figure 7.18**. A main photo-bleaching (PB) peak discovered at around 1.2 eV was attributed to the photoexcitation-induced exciton population onto the S_{11} state of (7,5) nanotubes. An second PB peak at around 1.25 eV which is identifiable only in some of the transient spectra can be ascribed to the population onto the S_{11} state of (6,5) nanotubes.

It was found that a change of suspended medium from aqueous solution to gelatin led to a small blue-shifting of (7,5) PB peak for both unfilled (~ 25 meV) and HgTe-filled (~ 7 meV) SWCNTs. According to our earlier fluorescence studies, gelatin matrix can slightly modify the many-body interactions in SWCNTs. The observed blue-shifts in TA spectra, therefore, can be due to a change of exciton properties such as increased binding energy.

111
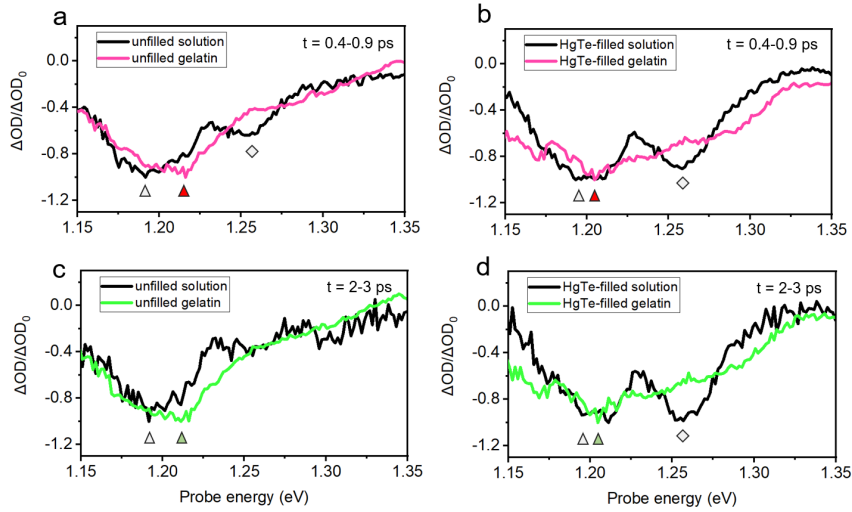
Figure 7.18: Transient absorption spectra of the unfilled or HgTe-filled SWCNTs in solution and embedded in the gelatin film averaged over different time windows. The measurements were conducted under a pump wavelength of 625 nm and at a fluence of 17 mJ cm^{-2} pulse^{-1}. The triangle and diamond symbols denotes the photobleach (PB) features of (7,5) and (6,5), respectively.

7.8   Questions addressed in this chapter and conclusions

In this chapter, I investigated the effect of environment on the optical properties of semiconducting SWCNTs. By means of changing the suspending medium from water to gelatin matrix and fabricating nanotube thin film networks based on vacuum filtration, the environment of these SWCNTs were altered. It was shown that a change of the suspending medium from water to gelatin matrix resulted in a modification of the many-body interaction in small-diameter SWCNTs. The bundling of nanotubes upon the formation of thin film network results in the remarkable broadening and red-shifting of the absorption peaks, which indicated a significant change in the excitonic properties due to band renormalization and tube-tube energy transfer upon SWCNT bundling. Based on the temperature-dependent fluorescence and Raman studies, it was demonstrated that filling with NWs alters the intratube bond stiffness of the SWCNTs, as well as the intertube interactions within SWCNT bundles. The experimental studies here demonstrate that both filling with atomic nanowires and changing the surrounding environment can finely tune the optical properties of SWCNTs. This could pave the way for a comprehensive understanding on the interactions within ultrathin 1D heterostructures. In particular, for applications involving semiconducting nanotubes (*e.g.* photocatalysis, transistors, and photovoltaics), our results identify the important role of the filling in modifying the

SWCNT structure and tube–tube interactions.

Chapter 8

Conclusions

Filling a material into the pore of a SWCNT provides the opportunity of understanding how extremely small species interact within a 1D nanosystem. A lot of studies in the past had demonstrated that such filling by the guest material can modify the physiochemical properties of SWCNTs. The implications of SWCNT filling include distortion of the nanotube structure, modification of the electronic and excitonic performances, change in the chemical reactivity and induced energy flow between the species. In this thesis, structures and spectroscopic properties of the diameter- and chirality-refined SWCNTs filled by atomic HgTe nanowires were studied. Based on electron microscopic characterizations, appearance of nanowires with desecrate atomic structures inside nanotubes can be observed. It was particularly found that nanowires with a cross-sectional thickness of just one atom arranged in either a linear or a zig-zag geometry can preferentially form inside small-diameter SWCNTs ($d_t \approx 0.8$ nm). With increased tube diameter, two atom-by-one atom-thick (2×1) and multiple atom-thick nanowires were found to be grown. The observed trend is in good agreement with the results of *ab initio* calculations reported earlier. Based on a range of spectroscopic characterization tools, it was discovered that encapsulation by nanowires can result in the modification of exciton, phonon and charge carrier features of SWCNTs.

In **Chapter 4**, we demonstrated the successful filling of different SWCNTs products (CoMoCAT76, CHASM, TUBALL, etc.) by the atomic nanowires. Based on subsequent gel column chromatography experiments, we extracted nanotubes in different diameters and of different chiralities. As a result of such diameter refinement, the structure of encapsulated nanowire can also be efficiently selected.

For CoMoCAT76 SWCNTs ($\bar{d}_t \approx 0.84$ nm), the gel column chromatography experiment led to a separation of small-diameter semiconducting and metallic nan-

otubes, in both of which a zig-zag-type one atom-thick chain was shown to be the dominant nanowire structure. For CHASM SWCNTs ($d_t = 0.8 - 1.4$ nm), linear one atom-thick chain and 2×1 atom-thick chain were found to be the two major structure type. After tube diameter refinement by gel column chromatography, small-sized SWCNTs can be extracted, which were found to be filled mainly by the linear one atom-thick nanowires. In large-diameter TUBALL SWCNTs ($d_t \approx 1.6$ nm), multiple atom-thick nanowires were found to be the main structure type. It was shown that the liquid phase-based chemical separation cannot lead to an efficient diameter refinement for these wide nanotubes.

In **Chapter 5** we carried out spectroscopic investigations on the metallic and semiconducting nanotubes extracted from the CoMoCAT76 SWCNTs. Based on Raman spectroscopy, a notable frequency downshifting and linewidth broadening of the G$^-$ peak (Breit-Wigner-Fano line) were discovered on metallic SWCNTs after filling by the zig-zag nanowires, which indicated an enhanced electron-phonon coupling. Based on subsequent transient absorption measurements, an increased decay rate of exciton dynamics for the metallic SWCNTs was demonstrated. It thus revealed an enhanced bi-exciton Auger recombination rate for these nanotubes after the filling. The experimental observations are in good agreement with previous theoretical studies, which reveal that the Auger process in SWCNTs is assisted by phonons and predict filling by nanowires can boost fast phonon relaxation channels for Auger recombination. Results here can thus be applied in the prediction of quantum efficiency for SWCNT-based nanoelectronics and devices.

In **Chapter 6**, we further investigated the filling effect on small-diameter CHASM and large-diameter TUBALL SWCNTs. For the diameter-refined CHASM SWCNTs, in which the one atom-thick chain is a dominant nanowire structure, we observed a substantial quenching of the fluorescence from nanotubes. The discovery was in contrast with results on zig-zag nanowire-filled SWCNT, which indicated the vital role of nanowire structure type on the optical performance of SWCNTs. A dependence of spectroscopic response on the SWCNT chirality was further demonstrated by Raman measurements, highlighting the effect of nanotube structure on the optical properties of SWCNTs with the filling. For investigations in the next step, it is hope to expand our knowledge on the spectroscopic response of nanowire-filled nanotubes as a function of changes in both the structures of nanotubes and encapsulated nanowires on an atomic level. The conductivity and free charge carrier features of the CHASM SWCNTs were also studied by using equilibrium-state and time-resolved terahertz spectroscopy. It was shown that encapsulating atomic nanowires led to modified free carrier concentration and transient spectral response

for the SWCNTs. The discoveries revealed that the nanowire-filled SWCNTs can have a potential of applications in ultrafast nanoelectronics and devices.

We also studied the spectroscopic features of large-diameter, polydispersed (bundled) TUBALL SWCNTs. Due to the fact that these bundled SWCNTs had extremely weak photoluminescence, we cannot efficiently assign their composition and chiralities. Developing chemical protocols to achieve the individualization of these nanotubes would be required for examining optical response from a chirality-known unfilled or nanowire-filled SWCNT.

Finally in **Chapter 7** we investigated the effect of environment on the optical properties of semiconducting SWCNTs. By means of changing the suspending medium from water to gelatin matrix and fabricating nanotube thin film networks based on vacuum filtration, the environment of these SWCNTs were altered. It was shown that a change of the suspending medium from water to gelatin matrix resulted in a modification of the many-body interaction in small-diameter SWC-NTs. The bundling of nanotubes upon the formation of thin film network results in the remarkable broadening and red-shifting of the absorption peaks, which indicated a significant change in the excitonic properties due to band renormalization and tube-tube energy transfer upon SWCNT bundling. Based on the temperature-dependent photoluminescence and Raman measurements in following investigations, it was demonstrated that filling with nanowires can alter the intratube bond stiffness of the SWCNTs, as well as the intertube interactions within SWCNT bundles. The above experimental studies hence demonstrate that both filling and changing the surrounding environment can be ways to finely tune the optical properties of SWCNTs.

Based on above experimental results and discussions, the outcomes and implications of research here are summarized as follows:

(i) The atomic nanowire-filled SWCNTs can be successfully separated based on diameters and chiralities by applying a gel column chromatography approach. Since different types of SWCNTs are desired for different applications (*e.g.* semiconducting SWCNTs can be applied for photocatalysis and photochemistry, while metallic SWCNTs have the potential in thin-film transistors and logic circus), chirality separation and consequently a purification based on the electronic type are therefore essential for achieving the numerous benefits of SWCNTs.

(ii) Encapsulation of atomic nanowires has been demonstrated to enhance electron-phonon coupling and change the Auger recombination rate of metallic SWCNTs in a predictable manner. These experimental studies are vital for the optimization of the device performance of SWCNT-based nanoelectronics, as Auger

recombination is known to limit the quantum efficiency.

(iii) The successful filling of HgTe nanowires into SWCNTs with different diameters can open doors for designing novel terahertz nanomaterials. With a size-dependent optical response in the IR regime, low-dimensional HgTe nanocrystals are convinced to be a candidate for terahertz materials [193]. Based on the results of time-resolved terahertz spectroscopy, a cross-over from negative to positive relative change in the time-domain electric field after photoexcitation ($\Delta E/E$) was found after filling SWCNTs by HgTe nanowires, which indicated a dynamic change of the spectral response with time. Further spectroscopic investigations will be needed to explicitly interpret the origin for such a change. However, they are beyond the scope of this thesis.

Appendix A

Transition Energies of Metallic SWCNTs

Resonant Raman spectroscopy based on tunable excitation energies is extensively used for experimental determination of the interband transition energies of metallic SWCNTs [194; 146], since they provide no photoluminescence. Due to trigonal warping, the M_{ii} transition state splits into two, M_{ii}^{-} and M_{ii}^{+} [16; 195]. **Figure A.1** shows summarized experimental energies of the M_{11}^{-} state of different metallic (n, m) species with diameters ranging from 0.7 to 1.4 nm. A excitation energy of 2.54 eV (488 nm) or 2.41 eV (514 nm) preferentially excite (n, m) species belonging to the $(2n + m) = 21$ family.
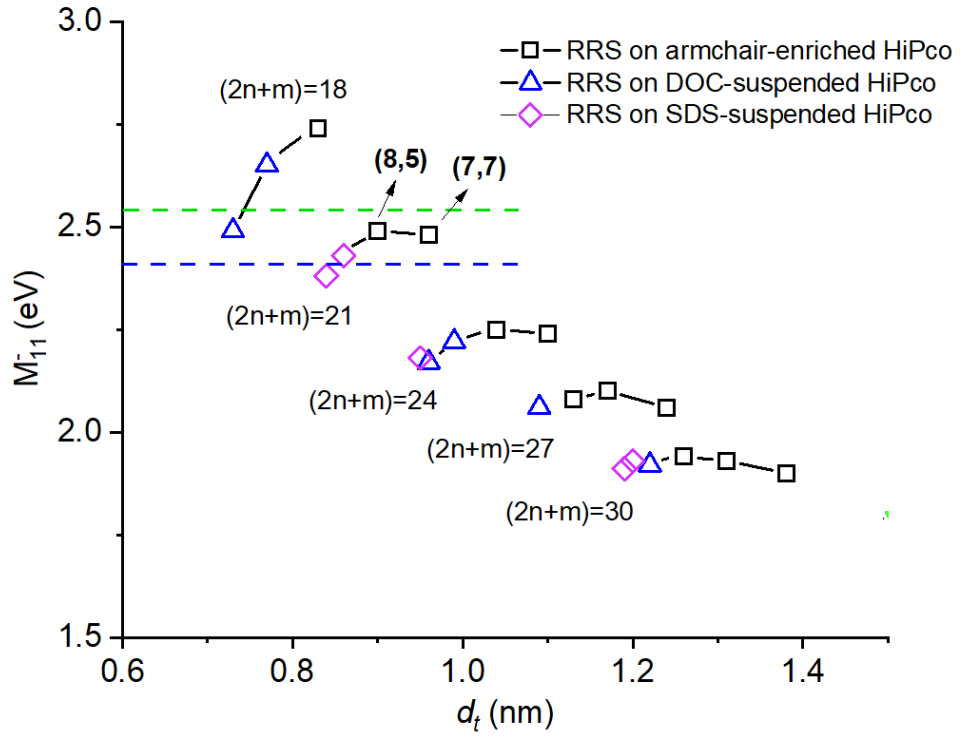
Figure A.1: Experimentally determined M_{11}^- energies of metallic SWCNT species belonging to different families in the HiPco product based on resonant Raman scattering (RRS) spectroscopy. Each data point relates to the transition energy verses diameter for a particular metallic (n, m) species, although they are not all annotated in the figure. Open squares and triangles data obtained from **Ref [146]**. Open diamonds are data obtained from **Ref [194]**. Horizontal green and blue dashed lines indicate the excitation energies applied for the Raman measurements in this thesis (see results in **Figure 5.9** in **Chapter 5**).

Appendix B

Prediction of Nanowire Structure in Nanotubes of Different Diameters

A previous study reported the filling of SWCNTs with tin telluride (SnTe) by a sublimation approach (formation of nanowires from gaseous Sn and Te). To predict the structure and stoichiometry of SnTe nanowires encapsulated in SWCNTs, *ab initio* random structure searching (AIRSS) [196] analyzed via a convex hull construction [197] was employed. This technique optimizes geometries of random structures in confinement of explicit SWCNT or confining potential [70]. Sampling of the stoichiometries is performed for investigating the potential disproportionation of the Sn:Te ratio during sublimation of the solid. In the convex hull construction, formation energy ϵ of the randomly generated structures upon *ab initio* optimization of their geometries is plotted against stoichiometry. In this way, per-atom formation energy is calculated with respect to the chemical potentials in a reservoir of ideal gas of Sn and Te atoms.

$$\epsilon = \frac{E_{Total} - E_{SWCNT}}{N} - \mu_{Sn} - X_{Te}(\mu_{Te} - \mu_{Sn}) \tag{B.1}$$

where E_{Total} and E_{SWCNT} are the total energy of nanowire encapsulated in a SWCNT and the energy of a pristine SWCNT, N is the number of atoms, μ is the chemical potential of each species and X_{Te} the ratio of Te atoms in the nanowire. The calculation reveals that with the increase in SWCNTs diameters, the difference between the formation energy of the encapsulated nanowires decreases, and com-
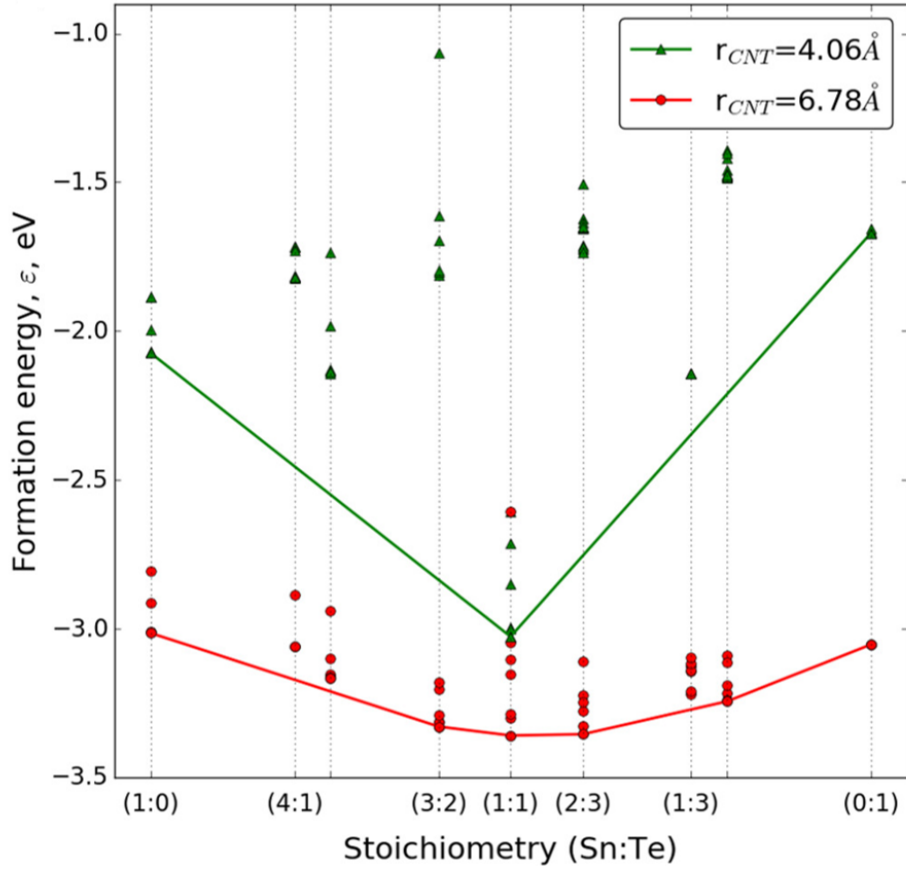
Figure B.1: Convex hull construction for SnTe nanowires with different stoichiometries embedded in SWCNT (6,6), r = 4.06 Å and SWCNT (10,10), r = 6.78 Å. The formation energy per atom is plotted for chemical potentials of Sn and Te relevant to an ideal gas 1:1 mixture with a density of 5.00 g/L at 300 K. Reproduced with permission from ref [74]. Copyright 2018 American Chemical Society.

pounds with varying stoichiometry other than a 1:1 ratio become more competitive, as shown by **Figure B.1**.

After identifying the lowest energy nanowire structures via AIRSS searches, their relative stability as a function of degree of confinement within SWCNT controlled by its diameter can be studied. The calculations reveal that the formation energies of different SnTe structures (linear (blue), single zig-zag (green), 2 atom-by-1 atom (red), double zig-zag (cyan) and 2 atom-by-2 atom (orange) chains) demonstrate the same trend as the diameters of the encapsulating SWCNT increases: first a rapid drop followed by a leveling off at the value corresponding to noninteracting nanowire–SWCNTs (see **Figure B.2**).

By comparing the formation energy of the predicted structures within differ-
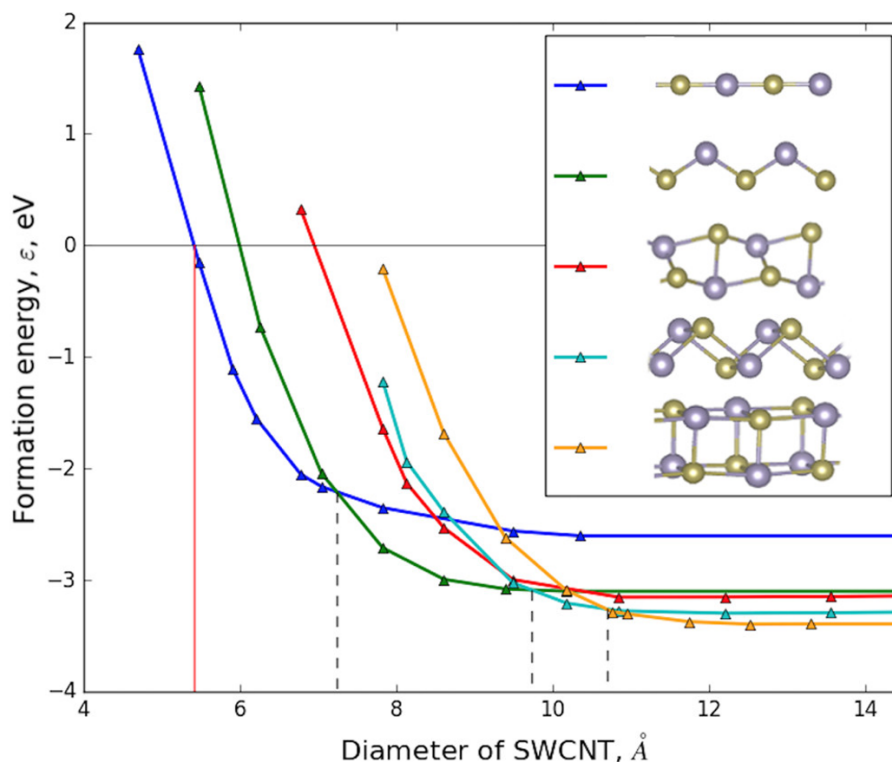
Figure B.2: Evolution of lowest formation energy of the nanowire as a function of SWCNT diameter. Red solid line denotes the smallest SWCNT diameter at which the formation of SnTe nanowire from gas is energetically accessible. Dashed vertical lines indicate where a potential structural transition between two types of nanowires can occur. Reproduced with permission from ref [74]. Copyright 2018 American Chemical Society.

ent diameters of SWCNTs, a dependence of the nanowire structure formed on the diameter of the encapsulating SWCNTs can be established. It can be found that the formation of linear or single zig-zag chain is favorable in the narrow nanotube with a typical diameter of less than 1 nm (**Figure B.2**). For wider nanotube, the rest of nanowire structures are more likely to form and a transition between these structures can occur since their formation in a SWCNT of the same diameter is energetically competitive.

Bibliography

[1] Amanda R. Amori, Zhentao Hou, and Todd D. Krauss. Excitons in single-walled carbon nanotubes and their dynamics. *Annual Review of Physical Chemistry*, 69:81–99, 4 2018.

[2] Yoichi Murakami, Shohei Chiashi, Yuhei Miyauchi, Minghui Hu, Masaru Ogura, Tatsuya Okubo, and Shigeo Maruyama. Growth of vertically aligned single-walled carbon nanotube films on quartz substrates and their optical anisotropy. *Chemical Physics Letters*, 385:298–303, 2 2004.

[3] Nima Akima, Yoshihiro Iwasa, Sonal Brown, Andi M Barbour, Jinbo Cao, Janice L Musfeldt, Hiroshi Matsui, Naoki Toyota, Masashi Shiraishi, Hideo Shimoda, Otto Zhou, Y Iwasa, S Brown, A M Barbour, J Cao, J L Musfeldt, H Matsui, N Toyota, M Shiraishi, H Shimoda, and O Zhou. Strong anisotropy in the far-infrared absorption spectra of stretch-aligned single-walled carbon nanotubes. *Advanced Materials*, 18:1166–1169, 5 2006.

[4] Pavel Nikolaev. Gas-phase production of single-walled carbon nanotubes from carbon monoxide: A review of the hipco process. *Journal of Nanoscience and Nanotechnology*, 4:307–316, 4 2004.

[5] J. Tittmann-Otto, S. Hermann, J. Kalbacova, M. Hartmann, M. Toader, R. D. Rodriguez, S. E. Schulz, D. R.T. Zahn, and T. Gessner. Effect of cleaning procedures on the electrical properties of carbon nanotube transistors—a statistical study. *Journal of Applied Physics*, 119:124509, 3 2016.

[6] Giulio Lolli, Liang Zhang, Leandro Balzano, Nataphan Sakulchaicharoen, Yongqiang Tan, and Daniel E. Resasco. Tailoring (n,m) structure of single-walled carbon nanotubes by modifying reaction conditions and the nature of the support of como catalysts. *Journal of Physical Chemistry B*, 110:2108–2115, 2 2006.

[7] Randy D. Mehlenbacher, Thomas J. McDonough, Maksim Grechko, Meng-Yin Wu, Michael S. Arnold, and Martin T. Zanni. Energy transfer pathways in semiconducting carbon nanotubes revealed using two-dimensional white-light spectroscopy. *Nature Communications*, 6(1):6732, dec 2015.

[8] Hagen Telg, Juan G. Duque, Matthias Staiger, Xiaomin Tu, Frank Hennrich, Manfred M. Kappes, Ming Zheng, Janina Maultzsch, Christian Thomsen, and Stephen K. Doorn. Chiral index dependence of the g + and g - raman modes in semiconducting carbon nanotubes. *ACS Nano*, 6:904–911, 1 2012.

[9] B. W. Smith, M. Monthioux, and D. E. Luzzi. Encapsulated C60 in carbon nanotubes. *Nature 1998 396:6709*, 396(6709):323–324, nov 1998.

[10] Sofie Cambré, Jochen Campo, Charlie Beirnaert, Christof Verlackt, Pegie Cool, and Wim Wenseleers. Asymmetric dyes align inside carbon nanotubes to yield a large nonlinear optical response. *Nature Nanotechnology 2015 10:3*, 10(3):248–252, feb 2015.

[11] Martin Hart, Edward R. White, Ji Chen, Catriona M. McGilvery, Chris J. Pickard, Angelos Michaelides, Andrea Sella, Milo S. P. Shaffer, and Christoph G. Salzmann. Encapsulation and Polymerization of White Phosphorus Inside Single-Wall Carbon Nanotubes. *Angewandte Chemie*, 129(28):8256–8260, jul 2017.

[12] Masataka Nagata, Shivani Shukla, Yusuke Nakanishi, Zheng Liu, Yung-Chang Lin, Takuma Shiga, Yuto Nakamura, Takeshi Koyama, Hideo Kishida, Tsukasa Inoue, Naoyuki Kanda, Shun Ohno, Yuki Sakagawa, Kazu Suenaga, and Hisanori Shinohara. Isolation of Single-Wired Transition-Metal Monochalcogenides by Carbon Nanotubes. *Nano Letters*, 19(8):4845–4851, aug 2019.

[13] Jing Kai Qin, Pai Ying Liao, Mengwei Si, Shiyuan Gao, Gang Qiu, Jie Jian, Qingxiao Wang, Si Qi Zhang, Shouyuan Huang, Adam Charnas, Yixiu Wang, Moon J. Kim, Wenzhuo Wu, Xianfan Xu, Hai Yan Wang, Li Yang, Yoke Khin Yap, and Peide D. Ye. Raman response and transport properties of tellurium atomic chains encapsulated in nanotubes. *Nature Electronics*, 3(3):141–147, mar 2020.

[14] A. A. Eliseev, L. V. Yashina, N. I. Verbitskiy, M. M. Brzhezinskaya, M. V. Kharlamova, M. V. Chernysheva, A. V. Lukashin, N. A. Kiselev, A. S. Kumskov, B. Freitag, A. V. Generalov, A. S. Vinogradov, Y. V. Zubavichus,

E. Kleimenov, and M. Nachtegaal. Interaction between single walled carbon nanotube and 1D crystal in CuX@SWCNT (X = Cl, Br, I) nanostructures. *Carbon*, 50(11):4021–4039, sep 2012.

[15] J. Campo, Y. Piao, S. Lam, C. M. Stafford, J. K. Streit, J. R. Simpson, A. R. Hight Walker, and J. A. Fagan. Enhancing single-wall carbon nanotube properties through controlled endohedral filling. *Nanoscale Horizons*, 1(4):317–324, jun 2016.

[16] R. Saito and G. Dresselhaus. Trigonal warping effect of carbon nanotubes. *Physical Review B*, 61(4):2981, jan 2000.

[17] Ernesto Joselevich, Hongjie Dai, Jie Liu, Kenji Hata, and Alan H. Windle. Carbon nanotube synthesis and organization. *Topics in Applied Physics*, 111:101–164, 2008.

[18] Andreas Thess, Roland Lee, Pavel Nikolaev, Hongjie Dai, Pierre Petit, Jerome Robert, Chunhui Xu, Young Hee Lee, Seong Gon Kim, Andrew G. Rinzler, Daniel T. Colbert, Gustavo E. Scuseria, David Tománek, John E. Fischer, and Richard E. Smalley. Crystalline Ropes of Metallic Carbon Nanotubes. *Science*, 273(5274):483–487, jul 1996.

[19] D. S. Bethune, C. H. Klang, M. S. De Vries, G. Gorman, R. Savoy, J. Vazquez, and R. Beyers. Cobalt-catalysed growth of carbon nanotubes with single-atomic-layer walls. *Nature 1993 363:6430*, 363(6430):605–607, 1993.

[20] Xiao-Di Wang, K. Vinodgopal, and Gui-Ping Dai. Synthesis of Carbon Nanotubes by Catalytic Chemical Vapor Deposition. *Perspective of Carbon Nanotubes*, oct 2019.

[21] S. N. Bondi, W. J. Lackey, R. W. Johnson, X. Wang, and Z. L. Wang. Laser assisted chemical vapor deposition synthesis of carbon nanotubes and their characterization. *Carbon*, 44(8):1393–1403, jul 2006.

[22] M. S. Dresselhaus, G. Dresselhaus, A. Jorio, A. G. Souza Filho, M. A. Pimenta, and R. Saito. Single nanotube Raman spectroscopy. *Accounts of Chemical Research*, 35(12):1070–1078, dec 2002.

[23] Jeroen W.G. Wildöer, Liesbeth C. Venema, Andrew G. Rinzler, Richard E. Smalley, and Cees Dekker. Electronic structure of atomically resolved carbon nanotubes. *Nature 1998 391:6662*, 391:59–62, 1 1998.

[24] H. Kataura, Y. Kumazawa, Y. Maniwa, I. Umezu, S. Suzuki, Y. Ohtsuka, and Y. Achiba. Optical properties of single-wall carbon nanotubes. *Synthetic Metals*, 103:2555–2558, 6 1999.

[25] R. Saito, M. Fujita, G. Dresselhaus, and M. S Dresselhaus. Electronic structure of chiral graphene tubules. *Applied Physics Letters*, 60:2204–2206, 5 1992.

[26] R Saito, G Dresselhaus, and M S Dresselhaus. Physical properties of carbon nanotubes. *Imperial College Press: London*, 7 1998.

[27] Noriaki Hamada, Shin Ichi Sawada, and Atsushi Oshiyama. New one-dimensional conductors: Graphitic microtubules. *Physical Review Letters*, 68:1579, 3 1992.

[28] R. Bruce Weisman and Sergei M. Bachilo. Dependence of optical transition energies on structure for single-walled carbon nanotubes in aqueous suspension: An empirical Kataura plot. *Nano Letters*, 3(9):1235–1238, sep 2003.

[29] Gordana Dukovic, Feng Wang, Daohua Song, Matthew Y. Sfeir, Tony F. Heinz, and Louis E. Brus. Structural dependence of excitonic optical transitions and band-gap energies in carbon nanotubes. *Nano Letters*, 5:2314–2318, 11 2005.

[30] Zhenjia Wang, Hermen Pedrosa, Todd Krauss, and Lewis Rothberg. Determination of the exciton binding energy in single-walled carbon nanotubes. *Physical Review Letters*, 96:047403, 2 2006.

[31] Vasili Perebeinos, J. Tersoff, and Phaedon Avouris. Scaling of excitons in carbon nanotubes. *Physical Review Letters*, 92:257402, 6 2004.

[32] Rodrigo B. Capaz, Catalin D. Spataru, Sohrab Ismail-Beigi, and Steven G. Louie. Diameter and chirality dependence of exciton properties in carbon nanotubes. *Physical Review B*, 74:121401, 9 2006.

[33] Larry Lüer, Sajjad Hoseinkhani, Dario Polli, Jared Crochet, Tobias Hertel, and Guglielmo Lanzani. Size and mobility of excitons in (6, 5) carbon nanotubes. *Nature Physics 2009 5:1*, 5:54–58, 11 2008.

[34] A. Ishii, M. Yoshida, and Y. K. Kato. Exciton diffusion, end quenching, and exciton-exciton annihilation in individual air-suspended carbon nanotubes. *Physical Review B - Condensed Matter and Materials Physics*, 91:125427, 3 2015.

[35] Jevgenij Chmeliov, Jonas Narkeliunas, Matt W. Graham, Graham R. Fleming, and Leonas Valkunas. Exciton–exciton annihilation and relaxation pathways in semiconducting carbon nanotubes. *Nanoscale*, 8:1618–1626, 1 2016.

[36] Catalin D. Spataru, Sohrab Ismail-Beigi, Lorin X. Benedict, and Steven G. Louie. Excitonic Effects and Optical Spectra of Single-Walled Carbon Nanotubes. *Physical Review Letters*, 92(7):077402, feb 2004.

[37] Ying Zhong Ma, Leonas Valkunas, Sergei M. Bachilo, and Graham R. Fleming. Exciton binding energy in semiconducting single-walled carbon nanotubes. *Journal of Physical Chemistry B*, 109(33):15671–15674, aug 2005.

[38] Jack Deslippe, Catalin D. Spataru, David Prendergast, and Steven G. Louie. Bound excitons in metallic single-walled carbon nanotubes. *Nano Letters*, 7:1626–1630, 6 2007.

[39] Feng Wang, David J. Cho, Brian Kessler, Jack Deslippe, P. James Schuck, Steven G. Louie, Alex Zettl, Tony F. Heinz, and Y. Ron Shen. Observation of excitons in one-dimensional metallic single-walled carbon nanotubes. *Physical Review Letters*, 99:227401, 11 2007.

[40] C. Manzoni, A. Gambetta, E. Menna, M. Meneghetti, G. Lanzani, and G. Cerullo. Intersubband exciton relaxation dynamics in single-walled carbon nanotubes. *Physical Review Letters*, 94(20):207401, may 2005.

[41] Aditya Mohite, Ji Tzuoh Lin, Gamini Sumanasekera, and Bruce W. Alphenaar. Field-enhanced photocurrent spectroscopy of excitonic states in single-wall carbon nanotubes. *Nano Letters*, 6(7):1369–1373, jul 2006.

[42] M. F. Lin. Optical spectra of single-wall carbon nanotube bundles. *Physical Review B*, 62:13153, 11 2000.

[43] A. Kis, G. Csányi, J. P. Salvetat, Thien Nga Lee, E. Couteau, A. J. Kulik, W. Benoit, J. Brugger, and L. Forró. Reinforcement of single-walled carbon nanotube bundles by intertube bridging. *Nature Materials 2004 3:3*, 3:153–157, 2 2004.

[44] Koray Yurekli, Cynthia A. Mitchell, and Ramanan Krishnamoorti. Small-angle neutron scattering from surfactant-assisted aqueous dispersions of carbon nanotubes. *Journal of the American Chemical Society*, 126(32):9902–9903, aug 2004.

[45] Matteo Calvaresi, Marco Dallavalle, and Francesco Zerbetto. Wrapping nanotubes with micelles, Hemimicelles, and cylindrical micelles. *Small*, 5(19):2191–2198, oct 2009.

[46] Naga Rajesh Tummala and Alberto Striolo. SDS Surfactants on carbon nanotubes: Aggregate morphology. *ACS Nano*, 3(3):595–602, mar 2009.

[47] Jinyu Pang and Guiying Xu. Molecular dynamics simulations of the interactions between SWNT and surfactants. *Computational Materials Science*, 65:324–330, dec 2012.

[48] Timothy J. McDonald, Chaiwat Engtrakul, Marcus Jones, Garry Rumbles, and Michael J. Heben. Kinetics of PL quenching during single-walled carbon nanotube rebundling and diameter-dependent surfactant interactions. *Journal of Physical Chemistry B*, 110(50):25339–25346, dec 2006.

[49] Lifeng Dong, Katherine L. Joseph, Colette M. Witkowski, and Michael M. Craig. Cytotoxicity of single-walled carbon nanotubes suspended in various surfactants. *Nanotechnology*, 19(25):255702, may 2008.

[50] Chih Jen Shih, Shangchao Lin, Michael S. Strano, and Daniel Blankschtein. Understanding the stabilization of single-walled carbon nanotubes and graphene in ionic surfactant aqueous solutions: Large-scale coarse-grained molecular dynamics simulation-assisted DLVO theory. *Journal of Physical Chemistry C*, 119(2):1047–1060, jan 2015.

[51] Xiang Zeng, Dehua Yang, Huaping Liu, Naigen Zhou, Yanchun Wang, Weiya Zhou, Sishen Xie, Hiromichi Kataura, X Zeng, D H Yang, H P Liu, Y C Wang, W Y Zhou, S S Xie, N G Zhou, and H Kataura. Detecting and Tuning the Interactions between Surfactants and Carbon Nanotubes for Their High-Efficiency Structure Separation. *Advanced Materials Interfaces*, 5(2):1700727, jan 2018.

[52] Michael S. Arnold, Alexander A. Green, James F. Hulvat, Samuel I. Stupp, and Mark C. Hersam. Sorting carbon nanotubes by electronic structure using density differentiation. *Nature Nanotechnology 2006 1:1*, 1(1):60–65, oct 2006.

[53] Saunab Ghosh, Sergei M. Bachilo, and R. Bruce Weisman. Advanced sorting of single-walled carbon nanotubes by nonlinear density-gradient ultracentrifugation. *Nature Nanotechnology 2010 5:6*, 5(6):443–450, may 2010.

[54] Erik H. Hároz, William D. Rice, Benjamin Y. Lu, Saunab Ghosh, Robert H. Hauge, R. Bruce Weisman, Stephen K. Doorn, and Junichiro Kono. Enrichment of armchair carbon nanotubes via density gradient ultracentrifugation: Raman spectroscopy evidence. *ACS Nano*, 4(4):1955–1962, apr 2010.

[55] Michael S. Arnold, Samuel I. Stupp, and Mark C. Hersam. Enrichment of single-walled carbon nanotubes by diameter in density gradients. *Nano Letters*, 5(4):713–718, apr 2005.

[56] Alexander A. Green and Mark C. Hersam. Nearly Single-Chirality Single-Walled Carbon Nanotubes Produced via Orthogonal Iterative Density Gradient Ultracentrifugation. *Advanced Materials*, 23(19):2185–2190, may 2011.

[57] Jeffrey A. Fagan, Constantine Y. Khripin, Carlos A. Silvera Batista, Jeffrey R. Simpson, Erik H. Hároz, Angela R. Hight Walker, and Ming Zheng. Isolation of Specific Small-Diameter Single-Wall Carbon Nanotube Species via Aqueous Two-Phase Extraction. *Advanced Materials*, 26(18):2800–2804, may 2014.

[58] Navaneetha K. Subbaiyan, Sofie Cambré, A. Nicholas G. Parra-Vasquez, Erik H. Hároz, Stephen K. Doorn, and Juan G. Duque. Role of surfactants and salt in aqueous two-phase separation of carbon nanotubes toward simple chirality isolation. *ACS Nano*, 8(2):1619–1628, feb 2014.

[59] Jeffrey A. Fagan, Erik H. Hároz, Rachelle Ihly, Hui Gui, Jeffrey L. Blackburn, Jeffrey R. Simpson, Stephanie Lam, Angela R. Hight Walker, Stephen K. Doorn, and Ming Zheng. Isolation of ¿1 nm diameter single-wall carbon nanotube species using aqueous two-phase extraction. *ACS Nano*, 9(5):5377–5390, may 2015.

[60] Han Li, Georgy Gordeev, Oisin Garrity, Stephanie Reich, and Benjamin S. Flavel. Separation of small-diameter single-walled carbon nanotubes in one to three steps with aqueous two-phase extraction. *ACS Nano*, 13(2):2567–2578, feb 2019.

[61] Huaping Liu, Daisuke Nishide, Takeshi Tanaka, and Hiromichi Kataura. Large-scale single-chirality separation of single-wall carbon nanotubes by simple gel chromatography. *Nature Communications 2011 2:1*, 2(1):1–8, may 2011.

[62] Huaping Liu, Takeshi Tanaka, Yasuko Urabe, and Hiromichi Kataura. High-efficiency single-chirality separation of carbon nanotubes using temperature-controlled gel chromatography. *Nano Letters*, 13(5):1996–2003, may 2013.

[63] Benjamin S. Flavel, Katherine E. Moore, Moritz Pfohl, Manfred M. Kappes, and Frank Hennrich. Separation of single-walled carbon nanotubes with a gel permeation chromatography system. *ACS Nano*, 8(2):1817–1826, feb 2014.

[64] Adrian Nish, Jeong Yuan Hwang, James Doig, and Robin J. Nicholas. Highly selective dispersion of single-walled carbon nanotubes using aromatic polymers. *Nature Nanotechnology 2007 2:10*, 2(10):640–646, sep 2007.

[65] Suman Kalyan Samanta, Martin Fritsch, Ullrich Scherf, Widianta Gomulya, Satria Zulkarnaen Bisri, and Maria Antonietta Loi. Conjugated polymer-Assisted dispersion of single-wall carbon nanotubes: The power of polymer wrapping. *Accounts of Chemical Research*, 47(8):2446–2456, aug 2014.

[66] Alexander L. Antaris, Jung Woo T. Seo, Alexander A. Green, and Mark C. Hersam. Sorting single-walled carbon nanotubes by electronic type using non-ionic, biocompatible block copolymers. *ACS Nano*, 4(8):4725–4732, aug 2010.

[67] Geyou Ao, Jason K. Streit, Jeffrey A. Fagan, and Ming Zheng. Differentiating Left- and Right-Handed Carbon Nanotubes by DNA. *Journal of the American Chemical Society*, 138(51):16677–16685, dec 2016.

[68] Jason K. Streit, Jeffrey A. Fagan, and Ming Zheng. A Low Energy Route to DNA-Wrapped Carbon Nanotubes via Replacement of Bile Salt Surfactants. *Analytical Chemistry*, 89(19):10496–10503, oct 2017.

[69] Daniel Roxbury, Jeetain Mittal, and Anand Jagota. Molecular-basis of single-walled carbon nanotube recognition by single-stranded DNA. *Nano Letters*, 12(3):1464–1469, mar 2012.

[70] Paulo V. C. Medeiros, Samuel Marks, Jamie M. Wynn, Andrij Vasylenko, Quentin M. Ramasse, David Quigley, Jeremy Sloan, and Andrew J. Morris. Single-Atom Scale Structural Selectivity in Te Nanowires Encapsulated Inside Ultranarrow, Single-Walled Carbon Nanotubes. *ACS Nano*, 11(6):6178–6185, jun 2017.

[71] R. Carter, J. Sloan, A. I. Kirkland, R. R. Meyer, P. J. D. Lindan, G. Lin, M. L. H. Green, A. Vlandas, J. L. Hutchison, and J. Harding. Correlation of Structural and Electronic Properties in a New Low-Dimensional Form of Mercury Telluride. *Physical Review Letters*, 96:215501, 2006.

[72] L. V. Yashina, A. A. Eliseev, M. V. Kharlamova, A. A. Volykhov, A. V. Egorov, S. V. Savilov, A. V. Lukashin, R. Püttner, and A. I. Belogorokhov.

Growth and Characterization of One-Dimensional SnTe Crystals within the Single-Walled Carbon Nanotube Channels. *Journal of Physical Chemistry C*, 115(9):3578–3586, mar 2011.

[73] Joseph H. Spencer, John M. Nesbitt, Harrison Trewhitt, Reza J. Kashtiban, Gavin Bell, Victor G. Ivanov, Eric Faulques, Jeremy Sloan, and David C. Smith. Raman Spectroscopy of Optical Transitions and Vibrational Energies of ∼1 nm HgTe Extreme Nanowires within Single Walled Carbon Nanotubes. *ACS Nano*, 8(9):9044–9052, sep 2014.

[74] Andrij Vasylenko, Samuel Marks, Jamie M. Wynn, Paulo V. C. Medeiros, Quentin M. Ramasse, Andrew J. Morris, Jeremy Sloan, and David Quigley. Electronic Structure Control of Sub-nanometer 1D SnTe via Nanostructuring within Single-Walled Carbon Nanotubes. *ACS Nano*, 12(6):6023–6031, jun 2018.

[75] Ziyi Hu, Ben Breeze, Reza J. Kashtiban, Jeremy Sloan, and James Lloyd-Hughes. Zigzag hgte nanowires modify the electron–phonon interaction in chirality-refined single-walled carbon nanotubes. *ACS Nano*, page 6789–6800, 4 2022.

[76] A. A. Eliseev, L. V. Yashina, M. M. Brzhezinskaya, M. V. Chernysheva, M. V. Kharlamova, N. I. Verbitsky, A. V. Lukashin, N. A. Kiselev, A. S. Kumskov, R. M. Zakalyuhin, J. L. Hutchison, B. Freitag, and A. S. Vinogradov. Structure and electronic properties of AgX (X = Cl, Br, I)-intercalated single-walled carbon nanotubes. *Carbon*, 48(10):2708–2721, aug 2010.

[77] Reza J. Kashtiban, Maria G. Burdanova, Andrij Vasylenko, Jamie Wynn, Paulo V. C. Medeiros, Quentin Ramasse, Andrew J. Morris, David Quigley, James Lloyd-Hughes, and Jeremy Sloan. Linear and Helical Cesium Iodide Atomic Chains in Ultranarrow Single-Walled Carbon Nanotubes: Impact on Optical Properties. *ACS Nano*, 15(8):13389–13398, aug 2021.

[78] Alexandr V. Talyzin, Ilya V. Anoshkin, Arkady V. Krasheninnikov, Risto M. Nieminen, Albert G. Nasibulin, Hua Jiang, and Esko I. Kauppinen. Synthesis of Graphene Nanoribbons Encapsulated in Single-Walled Carbon Nanotubes. *Nano Letters*, 11(10):4352–4356, oct 2011.

[79] P. M. Rafailov, C. Thomsen, and H. Kataura. Resonance and high-pressure Raman studies on carbon peapods. *Physical Review B*, 68(19):193411, nov 2003.

[80] Wim Wenseleers, Sofie Cambré, Jelena Čulin, August Bouwen, and Etienne Goovaerts. Effect of water filling on the electronic and vibrational resonances of carbon nanotubes: Characterizing tube opening by Raman spectroscopy. *Advanced Materials*, 19(17):2274–2278, sep 2007.

[81] Yuanchun Zhao, Li Song, Ke Deng, Zheng Liu, Zengxing Zhang, Yanlian Yang, Chen Wang, Haifang Yang, Aizi Jin, Qiang Luo, Changzhi Gu, Sishen Xie, and Lianfeng Sun. Individual Water-Filled Single-Walled Carbon Nanotubes as Hydroelectric Power Converters. *Advanced Materials*, 20(9):1772–1776, may 2008.

[82] Guan Lunhui, Suenaga Kazu, Shi Zujin, Gu Zhennan, and Sumio Iijima. Polymorphic Structures of Iodine and Their Phase Transition in Confined Nanospace. *Nano Letters*, 7(6):1532–1535, jun 2007.

[83] Stein van Bezouw, Dylan H. Arias, Rachelle Ihly, Sofie Cambré, Andrew J. Ferguson, Jochen Campo, Justin C. Johnson, Joeri Defillet, Wim Wenseleers, and Jeffrey L. Blackburn. Diameter-Dependent Optical Absorption and Excitation Energy Transfer from Encapsulated Dye Molecules toward Single-Walled Carbon Nanotubes. *ACS Nano*, 12(7):6881–6894, jul 2018.

[84] Haoran Qu, Archith Rayabharam, Xiaojian Wu, Peng Wang, Yunfeng Li, Jeffrey Fagan, Narayana R. Aluru, and Yu Huang Wang. Selective filling of n-hexane in a tight nanopore. *Nature Communications 2021 12:1*, 12(1):1–8, jan 2021.

[85] Sofie Cambré, Silvia M. Santos, Wim Wenseleers, Ahmad R.T. Nugraha, Riichiro Saito, Laurent Cognet, and Brahim Lounis. Luminescence properties of individual empty and water-filled single-walled carbon nanotubes. *ACS Nano*, 6(3):2649–2655, mar 2012.

[86] Quanzi Yuan and Ya Pu Zhao. Hydroelectric voltage generation based on water-filled single-walled carbon nanotubes. *Journal of the American Chemical Society*, 131(18):6374–6375, may 2009.

[87] P. H. Tan, A. G. Rozhin, T. Hasan, P. Hu, V. Scardaci, W. I. Milne, and A. C. Ferrari. Photoluminescence spectroscopy of carbon nanotube bundles: Evidence for exciton energy transfer. *Physical Review Letters*, 99(13):137402, sep 2007.

[88] Huihong Qian, Carsten Georgi, Neil Anderson, Alexander A. Greeny, Mark C. Hersam, Lukas Novotny, and Achim Hartschuh. Exciton energy transfer in

pairs of single-walled carbon nanotubes. *Nano Letters*, 8(5):1363–1367, may 2008.

[89] Rolf Koole, Peter Liljeroth, Celso De Mello Donegá, Daniël Vanmaekelbergh, and Andries Meijerink. Electronic coupling and exciton energy transfer in CdTe quantum-dot molecules. *Journal of the American Chemical Society*, 128(32):10436–10441, aug 2006.

[90] Ziyi Hu, Ryan O'Neill, Rostyslav Lesyuk, and Christian Klinke. Colloidal Two-Dimensional Metal Chalcogenides: Realization and Application of the Structural Anisotropy. *Accounts of Chemical Research*, 54(20):3792–3803, oct 2021.

[91] Yani Chen, Laëtitia Marty, and Nedjma Bendiab. New Light on Molecule–Nanotube Hybrids. *Advanced Materials*, 31(48):1902917, nov 2019.

[92] Christa M. Homenick, Robert James, Gregory P. Lopinski, Jeffrey Dunford, Junfeng Sun, Hyejin Park, Younsu Jung, Gyoujin Cho, and Patrick R.L. Malenfant. Fully printed and encapsulated swcnt-based thin film transistors via a combination of r2r gravure and inkjet printing. *ACS Applied Materials and Interfaces*, 8:27900–27910, oct 2016.

[93] Masayoshi Tange, Toshiya Okazaki, and Sumio Iijima. Selective extraction of large-diameter single-wall carbon nanotubes with specific chiral indices by poly(9,9-dioctylfluorene-alt-benzothiadiazole). *Journal of the American Chemical Society*, 133(31):11908–11911, aug 2011.

[94] Arko Graf, Laura Tropf, Yuriy Zakharko, Jana Zaumseil, and Malte C. Gather. Near-infrared exciton-polaritons in strongly coupled single-walled carbon nanotube microcavities. *Nature Communications 2016 7:1*, 7(1):1–7, oct 2016.

[95] Azure D. Avery, Ben H. Zhou, Jounghee Lee, Eui Sup Lee, Elisa M. Miller, Rachelle Ihly, Devin Wesenberg, Kevin S. Mistry, Sarah L. Guillot, Barry L. Zink, Yong Hyun Kim, Jeffrey L. Blackburn, and Andrew J. Ferguson. Tailored semiconducting carbon nanotube networks with enhanced thermoelectric properties. *Nature Energy 2016 1:4*, 1(4):1–9, apr 2016.

[96] Dominick J. Bindl, Nathaniel S. Safron, and Michael S. Arnold. Dissociating excitons photogenerated in semiconducting carbon nanotubes at polymeric photovoltaic heterojunction interfaces. *ACS Nano*, 4(10):5657–5664, oct 2010.

[97] Samuel D. Stranks, Severin N. Habisreutinger, Beate Dirks, and Robin J. Nicholas. Novel Carbon Nanotube-Conjugated Polymer Nanohybrids Produced By Multiple Polymer Processing. *Advanced Materials*, 25(31):4365–4371, aug 2013.

[98] Yanmei Piao, Brendan Meany, Lyndsey R. Powell, Nicholas Valley, Hyejin Kwon, George C. Schatz, and Yuhuang Wang. Brightening of carbon nanotube photoluminescence through the incorporation of sp3 defects. *Nature Chemistry 2013 5:10*, 5(10):840–845, jul 2013.

[99] Yin Zhang, Nicholas Valley, Alexandra H. Brozena, Yanmei Piao, Xiaoping Song, George C. Schatz, and Yuhuang Wang. Propagative sidewall alkylcarboxylation that induces red-shifted near-IR photoluminescence in single-walled carbon nanotubes. *Journal of Physical Chemistry Letters*, 4(5):826–830, mar 2013.

[100] Xiaojian Wu, Mijin Kim, Hyejin Kwon, and Yu Huang Wang. Photochemical Creation of Fluorescent Quantum Defects in Semiconducting Carbon Nanotube Hosts. *Angewandte Chemie International Edition*, 57(3):648–653, jan 2018.

[101] Tomohiro Shiraki, Yuhei Miyauchi, Kazunari Matsuda, and Naotoshi Nakashima. Carbon nanotube photoluminescence modulation by local chemical and supramolecular chemical functionalization. *Accounts of Chemical Research*, 53(9):1846–1859, sep 2020.

[102] Peng Wang, Jacob Fortner, Hongbin Luo, Jacek Kłos, Xiaojian Wu, Haoran Qu, Fu Chen, Yue Li, and YuHuang Wang. Quantum Defects: What Pairs with the Aryl Group When Bonding to the sp2 Carbon Lattice of Single-Wall Carbon Nanotubes? *Journal of the American Chemical Society*, jul 2022.

[103] Donghun Kang, Noejung Park, Ju hye Ko, Eunju Bae, and Wanjun Park. Oxygen-induced p-type doping of a long individual single-walled carbon nanotube. *Nanotechnology*, 16:1048–1052, 8 2005.

[104] R. S. Lee, H. J. Kim, J. E. Fischer, A. Thess, and R. E. Smalley. Conductivity enhancement in single-walled carbon nanotube bundles doped with k and br. *Nature*, 388:255–257, 7 1997.

[105] Soo Min Kim, Jin Ho Jang, Ki Kang Kim, Hyeon Ki Park, Jung Jun Bae, Woo Jong Yu, Il Ha Lee, Gunn Kim, Duong Dinh Loc, Un Jeong Kim, Eun-

Hong Lee, Hyeon-Jin Shin, Jae-Young Choi, and Young Hee Lee. Reduction-controlled viologen in bisolvent as an environmentally stable n-type dopant for carbon nanotubes. *Journal of the American Chemical Society*, 131:327–331, 1 2009.

[106] Shohei Horike, Qingshuo Wei, Kouki Akaike, Kazuhiro Kirihara, Masakazu Mukaida, Yasuko Koshiba, and Kenji Ishida. Bicyclic-ring base doping induces n-type conduction in carbon nanotubes with outstanding thermal stability in air. *Nature Communications*, 13:3517, 12 2022.

[107] Yoshiyuki Nonoguchi, Motohiro Nakano, Tomoko Murayama, Harutoshi Hagino, Shota Hama, Koji Miyazaki, Ryosuke Matsubara, Masakazu Nakamura, and Tsuyoshi Kawai. Simple salt-coordinated n-type nanocarbon materials stable in air. *Advanced Functional Materials*, 26:3021–3028, 5 2016.

[108] V. Derycke, R. Martel, J. Appenzeller, and Ph Avouris. Controlling doping and carrier injection in carbon nanotube transistors. *Applied Physics Letters*, 80:2773–2775, 4 2002.

[109] Takeshi Nakanishi and Tsuneya Ando. Optical Response of Finite-Length Carbon Nanotubes. *Journal of the Physical Society of Japan*, 78(11):114708–114708, nov 2009.

[110] M. V. Shuba, A. G. Paddubskaya, A. O. Plyushch, P. P. Kuzhir, G. Ya. Slepyan, S. A. Maksimenko, V. K. Ksenevich, P. Buka, D. Seliuta, I. Kasalynas, J. Macutkevic, G. Valusis, C. Thomsen, and A. Lakhtakia. Experimental evidence of localized plasmon resonance in composite materials containing single-wall carbon nanotubes. *Physical Review B*, 85(16):165435, apr 2012.

[111] Sergei M. Bachilo, Michael S. Strano, Carter Kittrell, Robert H. Hauge, Richard E. Smalley, and R. Bruce Weisman. Structure-assigned optical spectra of single-walled carbon nanotubes. *Science*, 298:2361–2366, 12 2002.

[112] Flávio Plentz, Henrique B. Ribeiro, Ado Jorio, Michael S. Strano, and Marcos A. Pimenta. Direct experimental evidence of exciton-phonon bound states in carbon nanotubes. *Physical Review Letters*, 95:247401, 12 2005.

[113] Fabien Vialla, Ermin Malic, Benjamin Langlois, Yannick Chassagneux, Carole Diederichs, Emmanuelle Deleporte, Philippe Roussignol, Jean Sébastien Lauret, and Christophe Voisin. Universal nonresonant absorption in carbon nanotubes. *Physical Review B - Condensed Matter and Materials Physics*, 90:155401, 10 2014.

[114] G. Ya Slepyan, M. V. Shuba, S. A. Maksimenko, C. Thomsen, and A. Lakhtakia. Terahertz conductivity peak in composite materials containing carbon nanotubes: Theory and interpretation of experiment. *Physical Review B - Condensed Matter and Materials Physics*, 81:205423, 5 2010.

[115] Qi Zhang, Erik H. Hároz, Zehua Jin, Lei Ren, Xuan Wang, Rolf S. Arvidson, Andreas Lüttge, and Junichiro Kono. Plasmonic nature of the terahertz conductivity peak in single-wall carbon nanotubes. *Nano Letters*, 13:5991–5996, 12 2013.

[116] Maria G. Burdanova, Alexey P. Tsapenko, Daria A. Satco, Reza Kashtiban, Connor D.W. Mosley, Maurizio Monti, Michael Staniforth, Jeremy Sloan, Yuriy G. Gladush, Albert G. Nasibulin, and James Lloyd-Hughes. Giant Negative Terahertz Photoconductivity in Controllably Doped Carbon Nanotube Networks. *ACS Photonics*, 6(4):1058–1066, apr 2019.

[117] Maria G. Burdanova, Alexey P. Tsapenko, Marianna V. Kharlamova, Esko I. Kauppinen, Boris P. Gorshunov, Junichiro Kono, and James Lloyd-Hughes. A Review of the Terahertz Conductivity and Photoconductivity of Carbon Nanotubes and Heteronanotubes. *Advanced Optical Materials*, 9(24):2101042, dec 2021.

[118] Maria G. Burdanova, Alexey P. Tsapenko, Marianna V. Kharlamova, Esko I. Kauppinen, Boris P. Gorshunov, Junichiro Kono, and James Lloyd-Hughes. A Review of the Terahertz Conductivity and Photoconductivity of Carbon Nanotubes and Heteronanotubes. *Advanced Optical Materials*, 9(24):2101042, dec 2021.

[119] T. Seifert, S. Jaiswal, U. Martens, J. Hannegan, L. Braun, P. Maldonado, F. Freimuth, A. Kronenberg, J. Henrizi, I. Radu, E. Beaurepaire, Y. Mokrousov, P. M. Oppeneer, M. Jourdan, G. Jakob, D. Turchinovich, L. M. Hayden, M. Wolf, M. Münzenberg, M. Kläui, and T. Kampfrath. Efficient metallic spintronic emitters of ultrabroadband terahertz radiation. *Nature Photonics 2016 10:7*, 10:483–488, 5 2016.

[120] Millie S. Dresselhaus, G. Dresselhaus, R. Saito, and A. Jorio. Raman spectroscopy of carbon nanotubes. *Physics Reports*, 409(2):47–99, mar 2005.

[121] A. Jorio, M. A. Pimenta, A. G. Souza Filho, Ge G. Samsonidze, A. K. Swan, M. S. Ünlü, B. B. Goldberg, R. Saito, G. Dresselhaus, and M. S. Dressel-

haus. Resonance raman spectra of carbon nanotubes by cross-polarized light. *Physical Review Letters*, 90:4, 3 2003.

[122] Alexander A Green, Matthew C Duch, and Mark C Hersam. Isolation of single-walled carbon nanotube enantiomers by density differentiation. *Nano Res*, 2:69–77, 2009.

[123] Mark C. Hersam. Progress towards monodisperse single-walled carbon nanotubes. *Nature Nanotechnology 2008 3:7*, 3:387–394, 5 2008.

[124] G. Brown, S. R. Bailey, M. Novotny, R. Carter, E. Flahaut, K. S. Coleman, J. L. Hutchison, M. L.H. Green, and J. Sloan. High yield incorporation and washing properties of halides incorporated into single walled carbon nanotubes. *Applied Physics A: Materials Science and Processing*, 76:457–462, 3 2003.

[125] F. Tuinstra and J. L. Koenig. Raman Spectrum of Graphite. *The Journal of Chemical Physics*, 53(3):1126, sep 2003.

[126] A. Hangleiter and R. Häcker. Enhancement of band-to-band auger recombination by electron-hole correlations. *Physical Review Letters*, 65:215, 7 1990.

[127] Peter T. (Peter Theodore) Landsberg. *Recombination in semiconductors*. Cambridge University Press, 1991.

[128] Mark J. Kerr and Andres Cuevas. General parameterization of auger recombination in crystalline silicon. *Journal of Applied Physics*, 91:2473–2480, 2 2002.

[129] M. S. Tyagi and R. Van Overstraeten. Minority carrier recombination in heavily-doped silicon. *Solid-State Electronics*, 26:577–597, 6 1983.

[130] Feng Wang, Yang Wu, Mark S. Hybertsen, and Tony F. Heinz. Auger recombination of excitons in one-dimensional systems. *Physical Review B*, 73(24):245424, jun 2006.

[131] Yoshihiko Kanemitsu. Multiple exciton generation and recombination in carbon nanotubes and nanocrystals. *Accounts of Chemical Research*, 46(6):1358–1366, jun 2013.

[132] Sougata Pal, David Casanova, and Oleg V. Prezhdo. Effect of Aspect Ratio on Multiparticle Auger Recombination in Single-Walled Carbon Nanotubes: Time Domain Atomistic Simulation. *Nano Letters*, 18(1):58–63, jan 2018.

[133] Yuhei Miyauchi. Photoluminescence studies on exciton photophysics in carbon nanotubes. *Journal of Materials Chemistry C*, 1:6499, 9 2013.

[134] Amanda R. Amori, Zhentao Hou, and Todd D. Krauss. Excitons in single-walled carbon nanotubes and their dynamics. *Annual Review of Physical Chemistry*, 69:81–99, 4 2018.

[135] Libai Huang and Todd D. Krauss. Quantized bimolecular auger recombination of excitons in single-walled carbon nanotubes. *Physical Review Letters*, 96(5):057407, feb 2006.

[136] Feng Wang, Gordana Dukovic, Ernst Knoesel, Louis E. Brus, and Tony F. Heinz. Observation of rapid auger recombination in optically excited semi-conducting carbon nanotubes. *Physical Review B - Condensed Matter and Materials Physics*, 70:1–4, 12 2004.

[137] Ying Zhong Ma, Leonas Valkunas, Susan L. Dexheimer, Sergei M. Bachilo, and Graham R. Fleming. Femtosecond spectroscopy of optical excitations in single-walled carbon nanotubes: Evidence for exciton-exciton annihilation. *Physical Review Letters*, 94:157402, 4 2005.

[138] Leonas Valkunas, Ying Zhong Ma, and Graham R. Fleming. Exciton-exciton annihilation in single-walled carbon nanotubes. *Physical Review B - Condensed Matter and Materials Physics*, 73:115432, 3 2006.

[139] Seok Ho Jeong, Ki Kang Kim, Seok Jin Jeong, Kay Hyeok An, Seung Hee Lee, and Young Hee Lee. Optical absorption spectroscopy for determining carbon nanotube concentration in solution. *Synthetic Metals*, 157(13-15):570–574, jul 2007.

[140] Xianjie Liu, Hans Kuzmany, Paola Ayala, Matteo Calvaresi, Francesco Zerbetto, and Thomas Pichler. Selective enhancement of photoluminescence in filled single-walled carbon nanotubes. *Advanced Functional Materials*, 22:3202–3208, 8 2012.

[141] H. Kuzmany, W. Plank, M. Hulman, Ch Kramberger, A. Grüneis, Th Pichler, H. Peterlik, H. Kataura, and Y. Achiba. Determination of SWCNT diameters from the Raman response of the radial breathing mode. *European Physical Journal B*, 22(3):307–320, aug 2001.

[142] M. J. Longhurst and N. Quirke. The environmental effect on the radial breathing mode of carbon nanotubes. II. Shell model approximation for internally

and externally adsorbed fluids. *Journal of Chemical Physics*, 125(18):184705, nov 2006.

[143] A. Jorio, G. Dresselhaus, M. S. Dresselhaus, M. Souza, M. S.S. Dantas, M. A. Pimenta, A. M. Rao, R. Saito, C. Liu, and H. M. Cheng. Polarized raman study of single-wall semiconducting carbon nanotubes. *Physical Review Letters*, 85(12):2617–2620, sep 2000.

[144] A. Jorio and R. Saito. Raman spectroscopy for carbon nanotube applications. *Journal of Applied Physics*, 129(2):21102, jan 2021.

[145] Erik H. Hároz, Juan G. Duque, Eduardo B. Barros, Hagen Telg, Jeffrey R. Simpson, Angela R. Hight Walker, Constantine Y. Khripin, Jeffrey A. Fagan, Xiaomin Tu, Ming Zheng, Junichiro Kono, and Stephen K. Doorn. Asymmetric excitation profiles in the resonance Raman response of armchair carbon nanotubes. *Physical Review B - Condensed Matter and Materials Physics*, 91(20):205446, may 2015.

[146] Erik H. Hároz, Juan G. Duque, Xiaomin Tu, Ming Zheng, Angela R. Hight Walker, Robert H. Hauge, Stephen K. Doorn, and Junichiro Kono. Fundamental optical processes in armchair carbon nanotubes. *Nanoscale*, 5(4):1411–1439, feb 2013.

[147] Martin Fouquet, Hagen Telg, Janina Maultzsch, Yang Wu, Bhupesh Chandra, J. Hone, Tony F. Heinz, and C. Thomsen. Longitudinal optical phonons in metallic and semiconducting carbon nanotubes. *Physical Review Letters*, 102(7):075501, feb 2009.

[148] A. M. Rao, P. C. Eklund, Shunji Bandow, A. Thess, and R. E. Smalley. Evidence for charge transfer in doped carbon nanotube bundles from raman scattering. *Nature*, 388(6639):257–259, 1997.

[149] O. Dubay, G. Kresse, and H. Kuzmany. Phonon softening in metallic nanotubes by a peierls-like mechanism. *Physical Review Letters*, 88:235506, 5 2002.

[150] Valentin N. Popov and Philippe Lambin. Radius and chirality dependence of the radial breathing mode and the g -band phonon modes of single-walled carbon nanotubes. *Physical Review B - Condensed Matter and Materials Physics*, 73:085407, 2 2006.

[151] Michele Lazzeri, S. Piscanec, Francesco Mauri, A. C. Ferrari, and J. Robertson. Phonon linewidths and electron-phonon coupling in graphite and nanotubes. *Physical Review B - Condensed Matter and Materials Physics*, 73:155426, 4 2006.

[152] Nicolas Caudal, A. Marco Saitta, Michele Lazzeri, and Francesco Mauri. Kohn anomalies and nonadiabaticity in doped carbon nanotubes. *Physical Review B - Condensed Matter and Materials Physics*, 75:115423, 3 2007.

[153] Moonsub Shim, Anshu Gaur, Khoi T. Nguyen, Daner Abdula, and Tanzer Ozel. Spectral diversity in raman g-band modes of metallic carbon nanotubes within a single chirality. *Journal of Physical Chemistry C*, 112:13017–13023, 8 2008.

[154] Daohua Song, Feng Wang, Gordana Dukovic, M. Zheng, E. D. Semke, Louis E. Brus, and Tony F. Heinz. Direct Measurement of the Lifetime of Optical Phonons in Single-Walled Carbon Nanotubes. *Physical Review Letters*, 100(22):225503, jun 2008.

[155] Sougata Pal, David Casanova, and Oleg V. Prezhdo. Effect of Aspect Ratio on Multiparticle Auger Recombination in Single-Walled Carbon Nanotubes: Time Domain Atomistic Simulation. *Nano Letters*, 18(1):58–63, jan 2017.

[156] Andrij Vasylenko, Jamie Wynn, Paulo V.C. Medeiros, Andrew J. Morris, Jeremy Sloan, and David Quigley. Encapsulated nanowires: Boosting electronic transport in carbon nanotubes. *Physical Review B*, 95(12):121408, mar 2017.

[157] D. Shao, P. Yotprayoonsak, V. Saunajoki, M. Ahlskog, J. Virtanen, V. Kangas, A. Volodin, C.V. Haesendonck, M. Burdanova, C.D.W. Mosley, and J. Lloyd-Hughes. Conduction properties of thin films from a water soluble carbon nanotube/hemicellulose complex. *Nanotechnology*, 29(14), 2018.

[158] Paul Delaney, Hyoung Joon Choi, Jisoon Ihm, Steven G. Louie, and Marvin L. Cohen. Broken symmetry and pseudogaps in ropes of carbon nanotubes. *Nature*, 391(6666):466–468, jan 1998.

[159] Charlotte A. Slade, Ana M. Sanchez, and Jeremy Sloan. Unprecedented New Crystalline Forms of SnSe in Narrow to Medium Diameter Carbon Nanotubes. *Nano Letters*, 19(5):2979–2984, may 2019.

[160] Tonya K. Leeuw, Dmitri A. Tsyboulski, Pavel N. Nikolaev, Sergei M. Bachilo, Sivaram Arepalli, and R. Bruce Weisman. Strain Measurements on Individual Single-Walled Carbon Nanotubes in a Polymer Host: Structure-Dependent Spectral Shifts and Load Transfer. *Nano Letters*, 8(3):826–831, mar 2008.

[161] Mingyuan Huang, Yang Wu, Bhupesh Chandra, Hugen Yan, Yuyao Shan, Tony F Heinz, and James Hone. Direct Measurement of Strain-Induced Changes in the Band Structure of Carbon Nanotubes. 2008.

[162] Pavan K. Valavala, Douglas Banyai, Max Seel, and Ranjit Pati. Self-consistent calculations of strain-induced band gap changes in semiconducting (n,0) carbon nanotubes. *Physical Review B - Condensed Matter and Materials Physics*, 78(23):235430, dec 2008.

[163] Jason Streit, Chad R. Snyder, Jochen Campo, Ming Zheng, Jeffrey R. Simpson, Angela R. Hight Walker, and Jeffrey A. Fagan. Alkane Encapsulation Induces Strain in Small-Diameter Single-Wall Carbon Nanotubes. *Journal of Physical Chemistry C*, 122(21):11577–11585, may 2018.

[164] A. I. Chernov, P. V. Fedotov, H. E. Lim, Y. Miyata, Z. Liu, K. Sato, K. Suenaga, H. Shinohara, and E. D. Obraztsova. Band gap modification and photoluminescence enhancement of graphene nanoribbon filled single-walled carbon nanotubes. *Nanoscale*, 10:2936–2943, 2018.

[165] Mehmet Orhan, Alper Kinaci, and Tahir Cagin. Dielectric properties of acetonitrile confined in carbon nanotubes. *Chemical Physics*, 530:110598, 2 2020.

[166] Jochen Campo, Sofie Cambré, Bea Botka, Jan Obrzut, Wim Wenseleers, and Jeffrey A. Fagan. Optical property tuning of single-wall carbon nanotubes by endohedral encapsulation of a wide variety of dielectric molecules. *ACS Nano*, 15:2301–2317, 2 2021.

[167] M. P. Anantram, Jie Han, and J. P. Lu. Band-gap change of carbon nanotubes: Effect of small uniaxial and torsional strain. *Physical Review B*, 60(19):13874, nov 1999.

[168] Gang Wu, Jian Zhou, and Jinming Dong. Raman modes of the deformed single-wall carbon nanotubes. *Physical Review B - Condensed Matter and Materials Physics*, 72(11):115411, sep 2005.

[169] Ki Kang Kim, Jin Sung Park, Sung Jin Kim, Hong Zhang Geng, Kay Hyeok An, Cheol Min Yang, Kentaro Sato, Riichiro Saito, and Young Hee Lee. Dependence of Raman spectra G band intensity on metallicity of single-wall carbon nanotubes. *Physical Review B - Condensed Matter and Materials Physics*, 76(20):205426, nov 2007.

[170] Christian Ehli, Christian Oelsner, Dirk M. Guldi, Aurelio Mateo-Alonso, Maurizio Prato, Cordula Schmidt, Claudia Backes, Frank Hauke, and Andreas Hirsch. Manipulating single-wall carbon nanotubes by chemical doping and charge transfer with perylene dyes. *Nature Chemistry 2009 1:3*, 1:243–249, 5 2009.

[171] Phaedon Avouris, Marcus Freitag, and Vasili Perebeinos. Carbon-nanotube photonics and optoelectronics. *Nature Photonics 2008 2:6*, 2(6):341–350, jun 2008.

[172] Hannah J. Joyce, Jessica L. Boland, Christopher L. Davies, Sarwat A. Baig, and Michael B. Johnston. A review of the electrical properties of semiconductor nanowires: insights gained from terahertz conductivity spectroscopy. *Semiconductor Science and Technology*, 31(10):103003, sep 2016.

[173] Peter Karlsen, Mikhail V. Shuba, Polina P. Kuzhir, Albert G. Nasibulin, Patrizia Lamberti, and Euan Hendry. Sign inversion in the terahertz photoconductivity of single-walled carbon nanotube films. *Physical Review B*, 98(24):241404, dec 2018.

[174] Stephen K. Doorn, Michael S. Strano, Michael J. O'Connell, Erik H. Haroz, Kristy L. Rialon, Robert H. Hauge, and Richard E. Smalley. Capillary electrophoresis separations of bundled and individual carbon nanotubes. *Journal of Physical Chemistry B*, 107(25):6063–6069, jul 2003.

[175] Tao Liu, Zhiwei Xiao, and Ben Wang. The exfoliation of SWCNT bundles examined by simultaneous Raman scattering and photoluminescence spectroscopy. *Carbon*, 47(15):3529–3537, dec 2009.

[176] Jeffrey R. Simpson, Oleksiy Roslyak, Juan G. Duque, Erik H. Hároz, Jared J. Crochet, Hagen Telg, Andrei Piryatinski, Angela R.Hight Walker, and Stephen K. Doorn. Resonance Raman signature of intertube excitons in compositionally-defined carbon nanotube bundles. *Nature Communications 2018 9:1*, 9(1):1–7, feb 2018.

142

[177] Katharina Arnold, Sergei Lebedkin, Oliver Kiowski, Frank Hennrich, and Manfred M. Kappes. Matrix-imposed stress-induced shifts in the photoluminescence of single-walled carbon nanotubes at low temperatures. *Nano Letters*, 4(12):2349–2354, dec 2004.

[178] S. Berger, C. Voisin, G. Cassabois, C. Delalande, P. Roussignol, and X. Marie. Temperature dependence of exciton recombination in semiconducting single-wall carbon nanotubes. *Nano Letters*, 7(2):398–402, 2007.

[179] L Yang and J Han. Electronic structure of deformed carbon nanotubes. *Phys. Rev. Lett.*, 85:154–157, 2000.

[180] Michael J. O'Connell, Saujan Sivaram, and Stephen K. Doorn. Near-infrared resonance raman excitation profile studies of single-walled carbon nanotube intertube interactions: A direct comparison of bundled and individually dispersed hipco nanotubes. *Physical Review B - Condensed Matter and Materials Physics*, 69:235415, 6 2004.

[181] Randy K. Wang, Wei Chiang Chen, Daisy K. Campos, and Kirk J. Ziegler. Swelling the micelle core surrounding single-walled carbon nanotubes with water-immiscible organic solvents. *Journal of the American Chemical Society*, 130:16330–16337, 12 2008.

[182] James Lloyd-Hughes and Tae-In Jeon. A Review of the Terahertz Conductivity of Bulk and Nano-Materials. *Journal of Infrared Millimeter and Terahertz Waves*, 33(9):871, 2012.

[183] A. B. Christie, I. Sutherland, and J. M. Walls. Studies of the composition, ion-induced reduction and preferential sputtering of anodic oxide films on Hg0.8Cd0.2Te by XPS. *Surface Science*, 135(1-3):225–242, dec 1983.

[184] P. W. Leech, P. J. Gwynn, and M. H. Kibel. A selective etchant for $Hg_{1-x}Cd_xTe$, CdTe and HgTe on GaAs. *Applied Surface Science*, 37(3):291–298, jul 1989.

[185] Zhenyu Zhang, Bo Wang, Ping Zhou, Dongming Guo, Renke Kang, and Bi Zhang. A novel approach of chemical mechanical polishing using environment-friendly slurry for mercury cadmium telluride semiconductors. *Scientific Reports*, 6(1):22466, mar 2016.

[186] Nick D. Hutson, Brian C. Attwood, and Kirk G. Scheckel. XAS and XPS Characterization of Mercury Binding on Brominated Activated Carbon. *Environmental Science and Technology*, 41(5):1747–1752, mar 2007.

[187] Shaohua Qiao, Jie Chen, Jianfeng Li, Zan Qu, Ping Liu, Naiqiang Yan, and Jinping Jia. Adsorption and Catalytic Oxidation of Gaseous Elemental Mercury in Flue Gas over MnOx/Alumina. *Industrial and Engineering Chemistry Research*, 48(7):3317–3322, apr 2009.

[188] Marianna V. Kharlamova, Markus Sauer, Takeshi Saito, Yuta Sato, Kazu Suenaga, Thomas Pichler, and Hidetsugu Shiozawa. Doping of single-walled carbon nanotubes controlled via chemical transformation of encapsulated nickelocene. *Nanoscale*, 7(4):1383–1391, jan 2015.

[189] Paulo T. Araujo, Stephen K. Doorn, Svetlana Kilina, Sergei Tretiak, Erik Einarsson, Shigeo Maruyama, Helio Chacham, Marcos A. Pimenta, and Ado Jorio. Third and Fourth Optical Transitions in Semiconducting Carbon Nanotubes. *Physical Review Letters*, 98(6):067401, feb 2007.

[190] Atsushi Hirano, Takeshi Tanaka, Yasuko Urabe, and Hiromichi Kataura. PH- and solute-dependent adsorption of single-wall carbon nanotubes onto hydrogels: Mechanistic insights into the metal/semiconductor separation. *ACS Nano*, 7(11):10285–10295, nov 2013.

[191] Patrick May, Hagen Telg, Guofang Zhong, John Robertson, Christian Thomsen, and Janina Maultzsch. Observation of excitonic effects in metallic single-walled carbon nanotubes. *Physical Review B*, 82(195412), 2010.

[192] Nachiket R. Raravikar, Pawel Keblinski, Apparao M. Rao, Mildred S. Dresselhaus, Linda S. Schadler, and Pulickel M. Ajayan. Temperature dependence of radial breathing mode Raman frequency of single-walled carbon nanotubes. *Physical Review B*, 66(23):235424, dec 2002.

[193] Nicolas Goubet, Amardeep Jagtap, Clément Livache, Bertille Martinez, Hervé Portalès, Xiang Zhen Xu, Ricardo P.S.M. Lobo, Benoit Dubertret, and Emmanuel Lhuillier. Terahertz hgte nanocrystals: Beyond confinement. *Journal of the American Chemical Society*, 140:5033–5036, 4 2018.

[194] J. Maultzsch, H. Telg, S. Reich, and C. Thomsen. Radial breathing mode of single-walled carbon nanotubes: Optical transition energies and chiral-index assignment. *Physical Review B - Condensed Matter and Materials Physics*, 72:205438, 11 2005.

[195] Seiji Uryu and Tsuneya Ando. Excitons in metallic carbon nanotubes with aharonov-bohm flux. *Physical Review B - Condensed Matter and Materials Physics*, 77:205407, 5 2008.

[196] Chris J. Pickard and R. J. Needs. High-pressure phases of silane. *Physical Review Letters*, 97:045504, July 2006.

[197] Andrew J. Morris, C. P. Grey, R. J. Needs, and Chris J. Pickard. Energetics of hydrogen/lithium complexes in silicon analyzed using the maxwell construction. *Physical Review B - Condensed Matter and Materials Physics*, 84:224106, Oct 2011.